Analysis of Strain in the Human Left Ventricle Using Real-Time 3D Echocardiography and Optical Flow

Viktor Gamarnik

Submitted in partial fulfillment of the
requirements for the degree of
Doctor of Philosophy
in the Graduate School of Arts and Sciences

COLUMBIA UNIVERSITY
2016

ABSTRACT

Analysis of Strain in the Human Left Ventricle Using Real-Time 3D

Echocardiography and Optical Flow

Viktor Gamarnik

Cardiovascular disease (CVD) consistently ranks among the leading causes of death in the United States. The most common subtype of CVD, ischemic heart disease, is a frequent precursor of myocardial infarction and heart failure, most commonly affecting the left ventricle (LV). Today, echocardiography is regarded as the gold standard in screening, diagnosis, and monitoring of LV dysfunction. But while global assessment of LV function tends to be quantitative, cardiologists with specific expertise still perform many regional evaluations subjectively. However, a more objective and quantitative measure of regional function – myocardial strain – has been developed and widely studied using 2D echocardiography.

With recent developments in real-time 3D echocardiography (RT3DE), it has become possible to measure strain in its native 3D orientation as well. Our laboratory's earlier work introduced the Optical Flow (OF) method of strain analysis, which was validated on simulated echocardiograms as well as through animal studies. The principal goal of this thesis is to translate this OF-based method of strain estimation from the research setting to the patient's bedside.

We have performed a series of studies to evaluate the feasibility, accuracy, and reproducibility of OF-based myocardial strain estimation in a routine clinical setting. The first investigation focused on the optimization of RT3DE acquisition and the OF processing pipeline

for use in human subjects. Subsequently, we evaluated the capacity of this technique to distinguish abnormal strain patterns in patients with CVD and varying degrees of LV dysfunction. Our analysis revealed that segmental strain measures obtained by OF may have better sensitivity and specificity than the more commonly used global LV strains. Our third validation study examined the reproducibility of these strain measures in both healthy and diseased populations. We established that OF-based strain measures demonstrate repeatability comparable to that achieved by the latest commercial software commonly used in clinical research to estimate 2D or 3D strain.

These studies were driven in large part by the absence of a ground truth or accepted gold standard of 3D strain measurements in the human LV. However, cardiac magnetic resonance imaging has had considerable success in measuring some forms of strain in the human LV. We therefore began to develop an image-processing pipeline to derive strain estimates from a new pulse sequence called 3D-DENSE. We further sought to improve the OF pipeline by automating the process of tracking the LV border. To this end, we developed a level-set based technique which tracks the LV endocardium. Our evaluation of its performance on RT3DE data confirmed that this method performs within the limits of inter-observer variability.

Overall, our pilot studies of OF-based strain estimation demonstrate that the technique possesses several promising features for improving cardiologists' ability to quantify and interpret the complex three-dimensional deformations of the human LV.

Table of Contents

List of Tables

List of Figures

List of Abbreviations

AHA   American Heart Association

AR   Aortic Regurgitation

AS   Aortic Stenosis

AUC   Area Under Curve

AV   Aortic Valve

CAD   Coronary Artery Disease

CI   Confidence Interval

CMR   Cardiac Magnetic Resonance Imaging

CO   Cardiac Output

CRT   Cardiac Resynchronization Therapy

CSPAMM   Complementary Spatial Modulation of Magnetization

CV   Coefficient of Variation/ across-subject variability

CVD   Cardiovascular disease

DBP   Diastolic Blood Pressure

DCM   Dilated Cardiomyopathy

DENSE   Displacement Encoding with Stimulated Echoes

DM2   Diabetes Mellitus Type 2

DRLSE	Distance Regularized Level Set Evolution
ECG	Electrocardiogram
ED	End-Diastole
EF	Ejection Fraction
ES	Effect Size
FOV	Field-Of-View
HCM	Hypertrophic Cardiomyopathy
HF	Heart Failure
HLD	Hyperlipidemia
HTN	Hypertension
ICC	Intraclass Correlation Coefficient
IHD	Ischemic Heart Disease
IRB	Institutional Review Board
LA	Left Atrium
LAD	Left Anterior Descending artery
LCA	Left Coronary Artery
LCx	Left Circumflex artery
LV	Left Ventricle/Left Ventricular
LVEF	Left Ventricle ejection fraction

MI	Myocardial Infarction
MR	Mitral Regurgitation
MRI	Magnetic Resonance Imaging
MS	Mitral Stenosis
MV	Mitral Valve
OF	Optical Flow
RA	Right Atrium
RCA	Right Coronary Artery
ROC	Receiver-Operating Characteristic
RT3DE	Real-Time 3D Echocardiography
RV	Right Ventricle
RWMA	Regional Wall Motion Analysis
RWMSI	Regional Wall Motion Score Index
SBP	Systolic Blood Pressure
SD	Standard Deviation
SPAMM	Spatial Modulation of Magnetization
STE	Speckle-Tracking Echocardiography
TDI	Tissue Doppler Imaging
TTE	Transthoracic Echo

TTPS	Time to Peak Strain
TV	Tricuspid Valve
VAR	Test-retest (Within-subject) Variability

Chapter 1. Introduction

1.1 Motivation

Cardiovascular disease (CVD) consistently ranks among the leading causes of death in the United States (Figure 1-1)[1]. Although CVD encompasses a broad range of heterogeneous conditions, ischemic heart disease (IHD) is by far the most common [2]. IHD is primarily caused by coronary atherosclerosis, or the buildup of plaques in the arterial endothelium [3], which results in hypoxia of the underlying heart tissue secondary to the reduced blood flow. Severe hypoxia in the myocardium ultimately leads to injury and tissue death – a condition commonly known as myocardial infarction (MI), which is a major cause of heart failure (HF) [4].
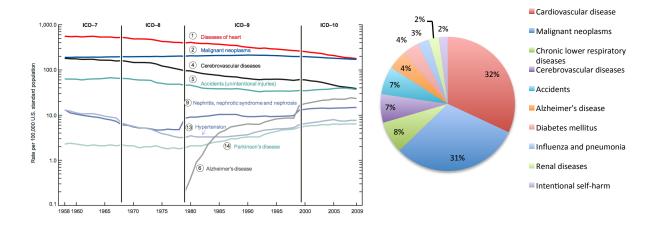
Figure 1-1. (Left) Incidence of the most common diseases in the US over time, expressed as rate per 100,000 individuals. (Right) The ten most common causes of death in the US. Note that in both graphs, diseases of the heart lead data from the latest National Vital Statistics Reports [1], [5].

Today, echocardiography is regarded as the gold standard in screening, diagnosis, and monitoring of left ventricular (LV) dysfunction. Even with the increased use of CT, MRI and nuclear imaging methods, the flexibility afforded by the variety of imaging modes in ultrasound, in addition to its low-cost and non-ionizing nature, has put this technology at the forefront of

clinical evaluation. Global assessments such as ejection fraction (EF) and stroke volume or cardiac output are routinely performed from echo images, and are well-established predictors of clinical outcomes in HF [6]-[8]. Evaluation of cardiac geometry (e.g. wall thickness, chamber dimensions) and tissue mass are also possible in both two- and three-dimensional images, and such evaluation is routine when screening for LV hypertrophy [9] and dilated cardiomyopathy, for example. The presence and severity of valvular disease is also regularly assessed using Doppler ultrasound [7].

Beyond these global indices of function, the temporal and spatial resolution possible in ultrasound make it uniquely qualified for detailed regional evaluation of function. For example, hypokinetic or dyskinetic regions, which can be identified on echo cine-loops, have been correlated with perfusion defects in coronary artery disease (CAD) [10]. However, this type of regional analysis is subjective, as it is performed visually and thus depends on the training and experience of the interpreter. A more objective measure is myocardial strain.

Strain (ε) is defined as the change in length (L) of tissue relative to its baseline state (L_0), i.e. $\varepsilon = (L-L_0)/L_0$ [11]. With respect to the heart, strain quantifies the magnitude of regional deformation of the myocardium throughout the cardiac cycle. Strain measurements have several critical advantages over pure motion measurements. Most significantly, strain measurements, both in subjects with preserved ejection fraction (EF) and in those with overt CVD, are prognostically relevant, being associated with future cardiovascular events [12]-[14]. Over the past 15 years, the research community has developed a substantial collection of evidence describing the prognostic and diagnostic value of strain measurements from 2D

echocardiograms. More recently, focus has also turned to strain estimates derived from real-time 3D (also called 4D) echocardiograms (RT3DE).

While RT3DE is capable of providing much more information than its 2D counterpart, adoption of this method in the clinic has been limited, in large part due to the lack of quantitative and efficient analytical tools. Previous work at the Heffner Biomedical Imaging Laboratory included developing several tools for quantitative, semi-automatic analysis of 4D echocardiograms [15], [16]. In particular, the Optical-Flow (OF) method of strain analysis introduced by Duan et al. [17] was tested on simulated echocardiographic data [18] and in animal studies (open-chest canines) [19]. In these settings, the OF technique proved to be an efficient and accurate approach to estimating myocardial strain and detecting abnormalities (e.g. from experimentally induced ischemia and infarction).

Given the potential of RT3DE and OF-based strain to significantly impact the process of echocardiographic screening and diagnosis, the overarching goal of the work presented in this thesis is to expand these achievements by translating these tools from the research setting to the bedside.

1.2 Overview and Contributions of the Thesis

1.2.1   Overview and Specific Aims

We identified three primary and two secondary areas of focus as critical steps in evolving the OF myocardial strain estimation approach for routine use in clinical settings. Following a brief overview of cardiac anatomy, echocardiographic imaging and strain measurement in

Chapter 2, Chapters 3-7 explore our specific aims:

1. **Adapting and evaluating the feasibility of OF-based strain measurements in humans:**
   Noninvasive imaging with RT3DE presents a number of substantial challenges compared
   to simulated data and invasive animal studies. The most salient of these are (1) lower
   image quality due to intervening tissues and reduced imaging windows; (2) lower frame
   rates secondary to the requirement of a wider and deeper field of view; and (3) lack of
   "ground truth" data. In Chapter 3, we describe the optimization of the RT3DE
   acquisition and the OF processing pipeline for use in humans. Using data acquired from
   healthy volunteers, we evaluate the strengths and weaknesses of this approach, based
   on the multiscale spatiotemporal framework described at the end of Chapter 2.

2. **Determining the capacity of OF-based strain measurements to distinguish abnormal
   patterns in patients with CVD**: We sought to test the hypothesis that the OF technique
   has sufficient sensitivity to distinguish healthy and diseased hearts and localize
   dysfunction. We recruited patients with an established history of CVD, from whom we
   acquired images in order to evaluate our ability to separate them from the healthy
   control population using global and segmental strain estimates. To mitigate the lack of
   ground truth strain data, we further correlated OF strain estimates with each patient's
   medical history based on previous laboratory and imaging data. These experiments are
   described in Chapter 4.

3. **Establishing the reproducibility of OF-based strain measures in healthy and diseased
   populations:** Owing to the potential difficulties in validating RT3DE measures with other
   imaging modalities (see below), we chose instead to establish the method's

reproducibility in healthy and diseased populations. In Chapter 5, we describe the methods and results of the reproducibility investigation, and compare our results to a well-established commercial software package used in clinical research studies to estimate 2D and 3D LV strain.

4. **Exploring additional validation approaches, via comparison with MRI:** Although ground-truth measurement of LV strain in humans is not currently possible, cardiac magnetic resonance imaging (CMR) has had considerable success in deriving strain estimates using a variety of pulse sequences. In Chapter 6, we explore the potential utility of a recently developed CMR method to generate dense strain maps in the human LV. In particular, we describe the implementation of an image-processing pipeline for derivation of strain measurements from 3D DENSE data, and address the required next steps to use such information for validation of RT3DE-based strain estimates.

5. **Automating myocardial border tracing with level sets**: As detailed in Chapter 3, the only manual steps in the RT3DE OF-based strain measurement pipeline are LV landmark selection and delineation of the epi- and endocardial borders. Although OF initialization requires only a single frame to be traced, access to the myocardial borders throughout the cardiac cycle can be advantageous. In Chapter 7, we explore the possibility of using a level-set method to automatically track the endocardial border, using data from earlier canine experiments.

Chapter 8 summarizes our findings along the various paths we investigated towards adapting and validating the RT3DE OF method in humans and generating the first evidence of its utility in a clinical setting. We also propose several compelling directions for future work,

including refinements to the OF pipeline to augment its robustness on clinical images, additional exploration of the data we have acquired, and options for validation using other modalities.

1.2.2 Contributions

In the course of completing this dissertation, we made several important contributions to the interpretation of myocardial strain from RT3DE imaging. As described in Chapter 2, we have proposed and implemented a multiscale spatiotemporal framework for examining 3D strain data. This work was the first to propose a formal method of interpreting 3D strain in the context of validation and verification experiments, while maintaining strong connections to accepted clinical standards. In subsequent experiments, we utilized this system to guide our validation studies using ultrasound as the primary modality. Notably, this framework is equally well suited for multi-modality validation experiments (for example, RT3DE vs. MRI), and for building data visualization approaches.

The work described in Chapter 3 constitutes the first characterization of strain variability in humans as measured by the RT3DE OF method. To reach this point, we first had to quantitatively verify that the pipeline performance would be robust in the context of the limited data quality afforded by noninvasive transthoracic echocardiography. Drawing upon theoretical and empirical evidence, we optimized the pipeline for consistent acquisition and LV strain estimation in human subjects. Furthermore, we introduced some optimizations to decrease the overall processing time and improve accuracy.

In Chapter 4, we present the first results of full 3D strain evaluation in patients with a wide spectrum of CVD. Whereas prior studies in animals suggested that OF-based strain estimates are sensitive to ischemic and infarcted conditions, our data suggest that certain components of 3D strain have sufficient sensitivity and specificity to distinguish patients with clinical risk factors for LV dysfunction (for example, hypertension and diabetes). In a further departure from most literature on this subject, we demonstrate that a composite strain measure has very high sensitivity and specificity compared to any one strain component considered individually.

In Chapter 5, we demonstrate the reproducibility of the RT3DE OF method in a population of healthy and diseased individuals. While previous work on this method has demonstrated success in simulated data and selected animal studies, this is the first experiment to statistically quantify the degree to which our estimates are consistent on clinical data, in a test-retest scenario. Our analysis revealed that while peak strain values may not have sufficient reliability, the reproducibility of average global strain profiles is consistent with previously reported techniques. Furthermore, we succeeded in validating the reliability of the composite strain measure first introduced in Chapter 4.

The analysis pipeline for 3D DENSE MR image data, presented in Chapter 6, has been fully developed in our laboratory, and uses a combination of existing tools adapted to our specific goals, as well as several new methodologies including phase-unwrapping and semi-automated segmentation and tracking of the LV borders. To date, we are aware of only one publication demonstrating the feasibility of LV strain computation from 3D DENSE images in humans. While this technique continues to be refined and will ultimately require its own validation protocol,

we have demonstrated that several key aspects of the image acquisition and analysis pipeline are feasible, in both healthy individuals and in patients with CVD.

Lastly, the endocardial border-tracking algorithm described in Chapter 7 constitutes an original formulation of the level set-based segmentation framework, exploiting image features specifically designed for echocardiography.

Chapter 2.   Background

2.1 Introduction

This chapter provides a highly abbreviated overview of the key areas that must be understood to fully grasp the technical and biological context of the techniques and results described in the remainder of the thesis. We will review basic cardiac anatomy, the pathophysiology of cardiovascular disease as it relates to the heart, and the fundamental principles of echocardiographic imaging and strain estimation. With these principles in mind, the chapter concludes with a presentation of a multi-resolution framework as an indispensable tool for fusing these concepts when interpreting left-ventricular strain measurements.

2.2 Heart Anatomy

2.2.1 Gross Anatomy and Circulatory Pathway

The human heart (Figure 2-1) is an electromechanical pump, comprising three structural systems: a connective tissue "skeleton" which provides overall structure and anchors the valves; an electrical signaling and conduction system which controls the precise timing of the pumping activity; and the muscular tissues (myocardium), whose contraction imparts force to the blood, propelling it throughout the body. The organ is subdivided into four chambers – the left and right atria (LA and RA), and the left and right ventricles (LV and RV) – and blood flow direction is controlled by unidirectional valves.

Oxygen-depleted blood enters the right atrium via the superior and inferior venae cavae. In diastole, while the myocardium undergoes relaxation, the tricuspid valve (TV) opens, permitting

blood to flow from the RA into the RV. When systolic contraction is triggered by depolarization of the sinoatrial node, the RV begins to contract. The resulting increase in pressure causes the TV to close, and blood is ejected from the RV into the pulmonary artery, through the open pulmonary valve.
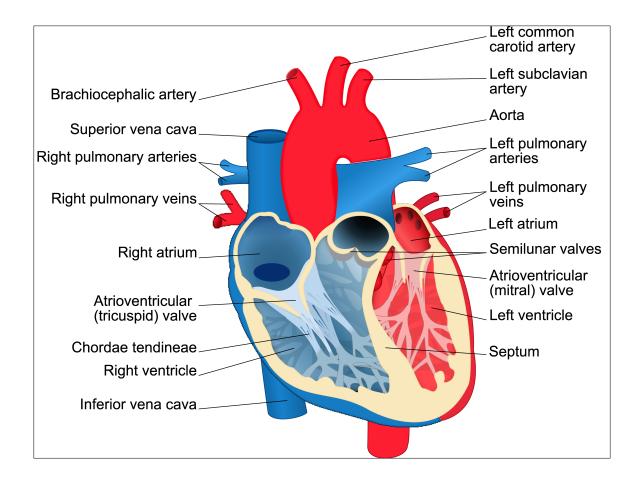
Figure 2-1. The human heart. Image source: wikimedia.org

Blood travels to the lungs, whose vast capillary bed facilitates the rapid and efficient exchange of carbon dioxide for oxygen via diffusive processes. Freshly oxygenated blood re-converges in the pulmonary veins, which deliver it to the LA. Blood then crosses the mitral valve

(MV) and enters the LV. Once again, systolic contraction triggers closing of the MV, and ejection of blood into the aorta across the aortic valve (AV). By this mechanism, oxygen is delivered to the rest of the body, and metabolic waste products such as CO_2 are collected for removal. Of the four chambers, the LV has the thickest myocardial wall, owing to its role in supplying blood to the entire body, which offers greater resistance.

Particularly pertinent to our subject is the heart's intricate vascular network, known as the coronary arteries and veins. Because the heart is constantly active, the coronary circulation is absolutely paramount to its function. Decreased flow through these vessels leads to an immediate decrease in the amount of oxygen and other nutrients available to the underlying myocardium – a condition known as ischemia. Cessation of flow in a coronary artery rapidly leads to death of the underlying tissue, i.e. a myocardial infarct or a "heart attack." As shown in Figure **2-2**, the coronary circulation originates near the aortic root, with the right and left coronary arteries (RCA and LCA, respectively).
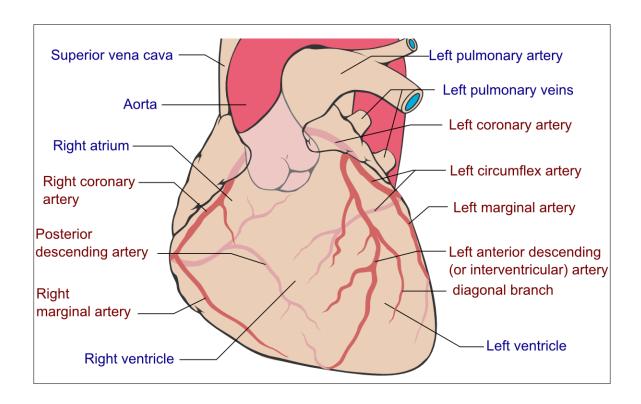
Figure 2-2. Coronary circulation. Image source: wikimedia.org

Although we will omit a full discussion of coronary circulation for the sake of brevity, we will note two vessels: the left anterior descending (LAD) and the left circumflex (LCx) arteries, both of which originate from the LCA. The LAD supplies blood to 45-55% of the LV, including the interventricular septum, the anterolateral wall, and the apex. The LCx may supply between 15-25% or up to 50% of the LV, depending on whether its distribution is right-dominant or left-dominant, respectively. Due to their primary role in sustaining the LV myocardium, these two vessels are frequent targets of experimental interventions, for example when the investigation targets induction of ischemia or infarction in the LV.

2.2.2   Left Ventricle Anatomy and Coordinate System

As the primary focus of this thesis is to examine LV function, we next present the conventions which will be used in the following chapters when discussing LV anatomy. From a classical anatomical perspective, the four walls of the LV are:

- The inferior wall, which rests upon the diagram (referred to in some literature as posterior wall);

- The anterior wall, which lies opposite the inferior;

- The septum, which separates the LV from the RV;

- The lateral wall, which lies opposite the septum (referred to in some literature as the free wall).

The variability in nomenclature arises in large part from the heart's asymmetrical shape and oblique position in the thorax [20]. For its part, the LV shape is roughly conical. This shape gives rise to the "natural coordinate system" of the LV, as follows:

- The *long axis (z)* is defined by a line extending between the apex and the center of the mitral valve;

- The *short axis (r, θ)* is defined as the plane orthogonal to any point along the long axis, with *r* denoting the radial distance from *z,* and θ denoting the circumferential angle from a radial direction of reference;

- The *origin* is then defined as the point where a short axis plane cutting through the *mid-septum* intersects the *z* axis.
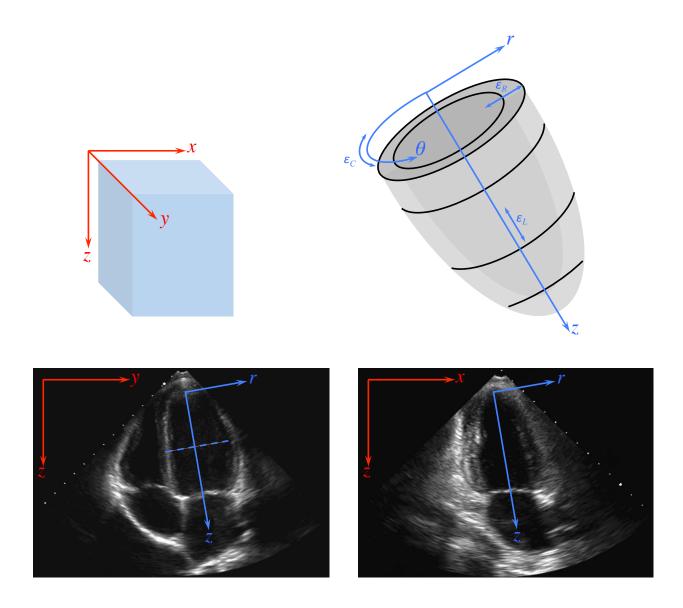
Figure 2-3. (Top Row) Illustration of the relationship between the Cartesian coordinate system *(x, y, z)* and the natural coordinate system of the LV *(r, θ, z)*, whose shape resembles an ellipsoid. (Bottom Row) The relationship between the coordinate systems is illustrated on 4-chamber and 2-chamber views of the heart, respectively. The dotted blue line, which defines a short-axis view through the mid-septum intersects the z-axis at the origin of the LV coordinate system, with θ *= 0* at the mid-septum.

Figure 2-3 provides a visual demonstration of this coordinate system, and how it relates to

the classical Cartesian *(x, y, z)* system, and to the standard views in echocardiography. As

discussed in section 2.5.1, this coordinate system is particularly useful when discussing the

principal directions of motion and deformation of the LV. As we will see in subsequent chapters, conversion between this 3D coordinate system and the Cartesian one is trivial – and by extension, so are mappings and projections onto other 2D and 3D conventions. For a thorough discussion of LV nomenclature, anatomy and their relationships to imaging, the reader is referred to [20], [21].

2.2.3   The 17-Segment AHA Model

In clinical cardiology, and particularly in the context of cardiac imaging, another system is frequently used to subdivide the LV. This is known as the standard 17-segment model, proposed by the American Heart Association (AHA) [22]. Whereas the LV coordinate system may be regarded as continuous, the AHA model suggests a discrete segmentation of the myocardium, along with a consistent nomenclature based on the gross anatomy. As shown in Figure 2-4, this model first splits the LV into three "levels" along the z-axis (the base, mid, and apical levels). The base and mid levels are then subdivided into six segments, while the apical level is composed of four segments corresponding to each wall of the LV, plus the apex itself. This segmentation has several critical advantages.

First, its combination of anatomical landmarks with simple geometry forms a strong bridge between the complicated true anatomy of the LV and the mathematically efficient *(r, θ, z)* coordinate system. Second, it can be broadly applied to multiple imaging modalities, facilitating direct comparisons of estimated values without sophisticated registration techniques (at least at the segment level). Third, it enjoys broad acceptance in the clinical community, meaning that
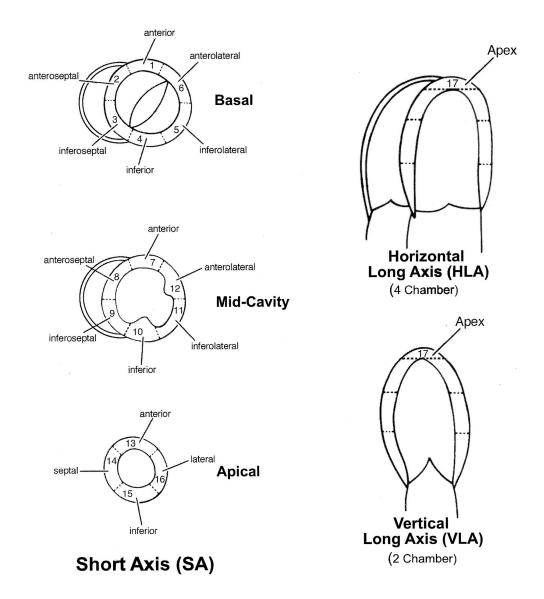
Figure 2-4. The AHA 17-segment model showing the segment names at the basal, mid, and apical levels, and the associated anatomical landmarks. Compare the HLA and VLA diagrams to the images in Figure 2-3. *Copied from* **[22]***, with permission. (License Number: 3704871283080)*

it is possible to correlate a physician's findings with novel data while employing identical nomenclature. Lastly, the geometry lends itself to straightforward extension to higher-resolution analysis (see Section 2.6).

2.3 Cardiovascular Disease

As mentioned in the introduction, CVD is a primary driving force of morbidity and mortality not only in the United States [1], but also worldwide, with 17.5 million deaths attributed to CVD in 2012, 7.4 million of which are specifically attributed to coronary heart disease [23]. While a full discussion of CVD and its many manifestations is beyond the scope of this work, we will describe several pathologies specifically in the context of their effects on the LV.

2.3.1 Ischemic Heart Disease

Fundamentally, IHD is a mismatch between the myocardium's demand for oxygen and the available supply [24]. It is most commonly caused by atherosclerosis, an inflammatory process of plaque formation in the arteries, ultimately leading to obstruction of blood flow and hence reduced oxygen supply to the underlying tissue, referred to as hypoxia. Reduced blood flow and hypoxia together lead to a rapid accumulation of metabolic products, whose effect upon the cardiac myocytes varies with the severity and duration of ischemia. Brief or mild ischemia may lead to reversible tissue injury, while cases of prolonged hypoxia or complete cessation of flow due to obstruction result in irreversible injury and necrosis.

The effect of regional ischemia upon LV function was quantitatively described by Little and O'Rourke in 1985 [25], who performed coronary occlusion experiments in canine models. Their investigation revealed that ischemia produces a rightward shift in the LV's end-systolic pressure-volume relationship, resulting in decreased stroke volume and consequently reduced LV ejection fraction (LVEF). This finding supported the theory that changes in contractility

caused by global ischemia alter the end-systolic elastance of the LV. Naturally, the magnitude of this effect is proportional to the extent of hypoperfusion: occlusion of the proximal LCx leads to greater and more global reductions in LVEF; by contrast, occlusion of the distal LAD creates a smaller area of hypoperfused LV myocardium, and consequently the LVEF impairment is less severe. In terms of identifiable motion defects, ischemia may produce a decline in the normal motion and deformation patterns of the affected region.

A myocardial infarct (MI) can be thought of as the extreme conclusion of ischemia: it results from complete coronary occlusion, leading to intense hypoxia, rapid build-up of metabolites, and eventually myocyte death, or necrosis. As in ischemia, the location, size, and severity of the infarcted region depend on which coronary vessel is occluded. Critically, whereas ischemia may produce reversible injury, infarction leads to *irreversible* tissue damage, and eventual scar formation and total loss of function in the affected region. In the case of sufficiently large infarcts, a decline in global LV function is seen in the form of impaired LVEF. The impact upon tissue motion and deformation is also more severe, manifesting as complete loss of function, and in some cases paradoxical behavior (e.g., while normal myocardium actively thickens during systolic contraction, infarcts are known to undergo passive thinning during this process).

2.3.2   *Cardiomyopathies*

Cardiomyopathies are a class of cardiac disease which manifest primarily as structural abnormalities of the myocardium. They are generally classified into three distinct types: dilated (DCM), hypertrophic (HCM), and restrictive. Of these, restrictive cardiomyopathy is the least common; the reader is referred to [24] for a detailed discussion.

In the context of LV dysfunction, the main feature of DCM is enlargement of the ventricular chamber without significant hypertrophy of the myocardium, and impaired *systolic* function. As in the case of ischemia, impaired contractility leads to reduced LVEF and decreased motion/ deformation. The key distinction, however, is that DCM affects the entire LV – there is no regional heterogeneity.

HCM, on the other hand, is characterized by abnormal thickening (i.e. hypertrophy) of the LV walls and consequent *diastolic* dysfunction. This pathology also typically affects the LV in a global manner, though the pattern is asymmetrical with the septum typically exhibiting the greatest hypertrophy. Notably, when hypertension is the primary etiology, the pattern tends to be symmetrical. The effect on LVEF is less specific in HCM since systolic function is unaffected, but the stiffer myocardium does increase diastolic pressures.

2.3.3   Valvular Heart Disease

Since the main function of cardiac valves is to ensure unidirectional flow between the chambers and outlets of the heart, they have two modes of failure. Regurgitation is the failure of the valve to prevent blood flow in the opposite direction to the normal circulatory pathway. Stenosis is the failure of the valve to permit adequate flow in the normal direction. Although the effects of a single valve's failure may propagate throughout the entire heart, we will address only the two valves which control LV inflow and outflow.

Mitral stenosis (MS) occurs when the mitral valve fails to fully open, preventing the free flow of blood from the LA to the LV in diastole. As a result, the normally miniscule pressure

gradient between the two chambers rises, and causes gradual enlargement of the LA. The impaired diastolic filling leads to decreased stroke volume and cardiac output, but since LV contractility is unaffected, LVEF may not be affected.

Mitral regurgitation (MR) is a failure of the valve apparatus to prevent retrograde flow from the LV to the LA during systolic contraction. In acute MR, there is insufficient time for physiologic adaptations; the retrograde flow therefore causes higher pressure and volume in the LA, a reduced forward CO, and diastolic stress on the LV owing to additional inflow from the LA from the previous contraction. The additional diastolic stretching actually causes an increase in LV stroke volume via the Frank-Starling mechanism [26]. If the MR develops more slowly, there is ample time for compensatory mechanisms to come into play, and the result is *chronic* MR. In particular, the normally stiff LA undergoes dilation to accommodate the increased blood volume. As the retrograde flow pathway becomes less and less resistant, the LV is affected in two ways: (1) the forward CO drops, since more and more of the stroke volume enters the LA rather than the aorta, and (2) the LV dilates, since the dilated LA is able to contain more blood, which drains into the LV in diastole and stretches it. Although in the early stages of chronic MR forward CO is relatively preserved, over time the chronic volume overload exerts its effect and leads to globally depressed LV function.

Aortic stenosis (AS), which frequently occurs in the elderly, is the failure of the aortic valve to permit forward flow out of the LV in systole. The reduced radius of the outflow orifice means that the LV must exert additional pressure to maintain adequate CO; in chronic AS, the LV compensates for this via hypertrophy. The gradual thickening and stiffening of the LV may also

lead to a form of ischemia, due to greater oxygen demand and reduced diastolic perfusion of the myocardium.

Aortic regurgitation (AR), like MR, is distinguished by retrograde flow of blood from the aorta into the LV during diastole. The condition is analogous to MR both in terms of the dysfunction and the compensatory mechanisms. In acute AR, the primary change in LV function is increased diastolic pressure due to additional blood volume, and, via the Frank-Starling mechanism, increased SV. In chronic AR, the persistently augmented blood volume in diastole causes global dilation and hypertrophy of the LV. Over time, this remodeling cascade can also produce systolic dysfunction.

In sum, failure of the valve apparatus can produce a variety of effects on the LV myocardium. The nature and severity of the resulting changes depends not only on the severity of the valve defect, but also on whether it is acute or chronic. In most situations, the LV remodeling is global, and the compensatory mechanisms eventually lead to diastolic and systolic dysfunction.

2.3.4   Arrhythmias

Arrhythmias and conduction abnormalities constitute a separate but related class of CVD. The underlying causes and clinical manifestations of these conditions are quite diverse, and while the incidence is lower than IHD [27], the associated morbidity is no less striking: electrical dysfunctions frequently lead to stroke [28], heart failure [29], and sudden cardiac death [30]. The specific type of electrical malfunction leads to characteristic changes both in the

electrocardiogram (ECG) and the motion of the heart. For example, atrioventricular block is a delay or interruption in the transmission of an impulse from the atria to the ventricles [31], causing dissociation between atrial and ventricular contraction. In this case, the atria and ventricles may both contract normally, but the contraction is asynchronous. By contrast, a condition like bundle branch block may generate not only asynchronous contraction between the ventricles, but regional wall motion abnormalities as well [32]. Objective measurement of dyssynchrony and treatments such as cardiac resynchronization therapy (CRT) are an active field of research and development.

Due to the diversity of abnormal cardiac rhythms and their complex nature, we cannot make significant generalizations about their effects on LV function. In subsequent chapters, we will provide specific details as needed. One point, however, is worth making at this time: many advanced imaging techniques rely on *ECG gating* and/or averaging of data over several heartbeats. An irregular heart rate frequently nullifies some of the key assumptions involved in gating and averaging (e.g. equal time intervals between successive beats), introducing artifacts into the images, or making acquisition altogether impossible. For this reason, despite the high prevalence of arrhythmias, patients with such conditions are frequently excluded from the study population.

2.3.5   Hypertension

High blood pressure, or hypertension, is a problem of enormous biological, medical, and social complexity. While the numerical definition is clear (diastolic blood pressure chronically ≥ 90 mmHg and/or systolic blood pressure chronically ≥ 140 mmHg), the etiology of the disease is

unknown in over 90% of patients. A full third of all US adults over 20 years of age are estimated to have hypertension; by 60, one half of all adults are affected [33]. While there is a tremendous body of literature describing the possible causes, mechanisms and treatments of hypertension, we wish here to outline only a few points. First, high blood pressure is a "silent" disease – if the disease is not detected by routine screening, patients are frequently asymptomatic until the blood pressure is exceedingly high, or begins causing other organ damage. Second, the effects are not confined to the cardiovascular system: hypertension is a known risk factor for renal disease, stroke, and retinopathy, as well as heart disease. With respect to end-organ damage in the heart, hypertension is known to accelerate atherosclerosis (leading to myocardial ischemia and infarction); it also increases the afterload seen by the LV, leading first to systolic dysfunction, then compensatory hypertrophy, and eventually systolic dysfunction and HF. Thus, the range of effects seen in the LV ranges from small, localized ischemia/infarcts to more global reductions in function as a consequence of LVH and ischemia.

2.4 Role of Echocardiography

Beyond the routine clinical assessment, which includes a detailed patient history and a comprehensive physical exam, patients with CVD and particularly those suspected of having LV dysfunction undergo a variety of tests. Initial examination typically includes an ECG, a chest X-ray, and blood tests.

Echocardiography is regarded as the gold standard in screening, diagnosis and monitoring of LV dysfunction. It is also the preferred diagnostic modality because it affords high frame rates, high clinical availability, no ionizing radiation, virtually no exclusion criteria, and much lower

cost when compared to CT, MRI and SPECT. Despite these advantages and frequent use in the clinical setting, the sensitivity and accuracy of this modality still depend on the skill of the human interpreting the acquired images. The amount of time necessary for a good "echo reading" is burdensome for the individual cardiologist, and naturally introduces a degree of subjectivity into the procedure.

2.4.1   2D Echocardiography

During a standard clinical echocardiographic examination, a trained registered sonographer acquires a set of still images and cine-loops, from which all measurements of heart structure and function are performed by a cardiologist with specific expertise. Acquisitions are performed from parasternal, apical, and subcostal acoustic windows, these being where ultrasound is best transmitted through soft tissues to the heart. From cine-loops of the moving heart, data about chamber dimensions, volumes, and wall thickness are measured. Spectral Doppler is used to quantify blood flow velocity through cardiac valves, and to detect abnormalities in such flows from valve insufficiency or stenosis [8]. The assessment of LV systolic function (the ejection phase of the cardiac cycle) is most frequently performed by measuring ejection fraction, which is calculated as

$$LVEF = \frac{end\ diastolic\ volume - end\ systolic\ volume}{end\ diastolic\ volume}$$

(2.1)

and expressed as a percentage. The two volumes in the formula are calculated either in 2D or in 3D, using the biplane modified Simpson's method, from two orthogonal apical views (4-chamber, 2-chamber view). EF values above 55% are considered normal, whereas EF below 55%

represents some degree of LV dysfunction [34]. Global assessments such as ejection fraction (EF) and stroke volume or cardiac output are routinely performed from echo images, and are well-established predictors of clinical outcomes [6], [8], [35].

LV wall motion analysis is performed by visual assessment of the magnitude of thickening during systole of each LV segment. The motions of all ventricular segments are assessed by integrating visual information from short- and long-axis views, and a global wall motion score is calculated by summing the individual scores of each segment. Regional evaluation of function is performed in a similar manner by individually examining the scores of each segment; for example, hypokinetic and dyskinetic regions have been correlated with perfusion defects in coronary artery disease (CAD). LV diastolic function (the filling phase of the cardiac cycle) is also assessed from trans-mitral Doppler flow, mitral valve velocity by tissue Doppler, pulmonary veins flow, and by measuring left atrial dimensions. The interpretation of the clinical echocardiographic exam, even if limited to the most clinically used parameters, is labor-intensive, time-consuming, as well as being subject to inter-observer variability.

2.4.2 3D Echocardiography

Real-time 3D (RT3D) echocardiography has been available for over a decade, but its clinical acceptance has been limited due to insufficient image quality and low temporal resolution compared to 2D imaging. Over time, RT3D echocardiography has become an important aid for the structural evaluation of cardiac valves, and it is gaining popularity in the functional assessment of the left and right ventricles and of the left atrial structure and function. 3D imaging of the heart confers several critical benefits over 2D. First, no geometric assumptions

are required because the entire heart chamber is imaged, so that its true orientation and dimensions are available. Second, analysis can be more comprehensive than with 2D, because every region of the myocardium can be examined, rather than just particular slices. In the context of LV imaging specifically, acquisition of the 3D image volume from an apical approach is also more efficient than 2D, which requires multiple acquisitions from different locations to sample every region. Lastly, when we consider motion and deformation analysis, RT3D imaging is not subject to out-of-plane motion problems, which are pervasive in 2D.

In sum, RT3D echocardiography offers the physician a wealth of information that is otherwise difficult or impossible to obtain from 2D imaging. While there is a large variety of software that facilitates quantitative analysis of 2D echocardiograms (e.g., Philips' QLAB[TM], GE's EchoPAC[TM], Toshiba's Artida[TM]), the selection of tools for comprehensive analysis of RT3DE images is much more limited (e.g., TomTec's 4D LV Function[TM]). In the absence of effective analytical tools, all this new information only amplifies the problems highlighted in the previous section: manual analysis of 3D data is even more labor-intensive and time-consuming than in 2D, and creates even more opportunities for inter-observer variability.

2.5 Role of Strain in Functional Assessment

2.5.1 Defining Strain

In layman's terms, "strain" usually refers to "stretching" of a material, and describes the deformation itself rather than the force which causes this deformation (the "stress"). For the purposes of this work, we will utilize the Lagrangian definition of deformation [11], which states

that strain (E) is defined as the change in length (L) of tissue relative to its baseline state (L_0):

$$E = \frac{L - L_0}{L_0}$$

(2.2)

By this definition, strain is a dimensionless ratio, and so it is often expressed directly as a fraction or a percent. While this definition will suffice for now, in Chapter 3, we will introduce another way to calculate strain, by examining the gradient of a displacement field.

With respect to the heart, strain quantifies the magnitude of regional deformation of the myocardium throughout the cardiac cycle. Typically, strains reported in the heart correspond to the three principal directions of myocardial deformation: radial (e.g. the thickening/thinning of the LV wall in systole and diastole, respectively), longitudinal (e.g. the systolic shortening and diastolic expansion of the LV along its long axis), and circumferential (e.g. the torsion of the LV in the short axis) – see Figure 2-3. Strain measurements have several critical advantages over pure motion measurements. Most significantly, strain measurements, both in subjects with preserved EF and in those with overt CVD, are prognostically relevant, being associated with future cardiovascular events [12], [14]. Furthermore, consideration of deformation, rather than motion alone, permits quantification of more complex patterns, such as the inherent twist of the LV, which has been suggested to be a reliable indicator of LV function as well [36].

2.5.2 Strain Estimation in Echocardiography

There are numerous approaches to myocardial strain estimation from echocardiographic data. Broadly, there are three categories, distinguished by the type of data that is acquired and analyzed. Acquisition of radiofrequency data in standard 2D echo views permits strain

quantification through myocardial elastography [37]. This high-resolution method has been used to image a number of interesting cardiac phenomena, including electromechanical wave propagation [38] in 2D.

Doppler-based measures of the myocardial velocity and strain rate are referred to as Tissue Doppler Imaging (TDI). TDI utilizes the Doppler effect with a standard ultrasound probe to measure the velocity of the insonified tissue throughout the cardiac cycle. Most commonly, TDI is performed in 2D B-mode views, and produces an estimate of motion (and, by extension, deformation), along the direction of US beam propagation [39], [40]. By this technique, measurement of each of the three principal strain components is possible, depending on which echocardiographic view is utilized. TDI-based estimates of radial strain dyssynchrony have been shown to be strong predictors of response to cardiac resynchronization therapy [41]. However, a critical limitation of TDI is angle-dependence: much as in the case of flow Doppler, the estimated tissue velocities (and consequently the strains) vary with the angle of incidence between the ultrasound beam and the observed tissue. This introduces a significant amount of variation into the technique, and impedes both the reliability and precision of the method [42].

The third set of methods for motion and strain estimation in ultrasound is commonly classified as speckle-tracking echocardiography (STE). Generally speaking, speckle-tracking methods take advantage of the fact that speckle patterns in tissue remain stable over sufficiently short time intervals. Thus, if the tissue is sampled at an appropriate rate, inter-frame motion may be estimated by measuring the displacement of persistent speckle patterns. Compared to TDI methods, STE can be applied in 3D and has the distinct advantages of angle-

independence [43], high spatial and temporal resolution, and sensitivity to small strains. When frame rates are limited to what is typically available in the clinic (i.e. < 100 Hz), it may be advantageous to apply speckle-tracking methods to B-mode data, as is the case with the optical flow (OF) method previously developed by our group [18], [44]. Another significant advantage of STE is that most clinical ultrasound machines neither store nor easily permit the exportation of RF data; thus, algorithms which use only standard B-mode images are considerably easier to incorporate into existing workflows. Strain estimates from such block-matching approaches are now commonly available on a variety of 2D ultrasound systems, but are still not fully calibrated and validated.

2.5.3 LV Strain in the Clinical Setting

A number of studies have suggested that strain estimates derived using these methods may be valuable predictors of clinically significant outcomes. Suffoletto et al. determined that radial strain, assessed via speckle-tracking echocardiography can quantify dyssynchrony and predict both short- and long-term response to Cardiac Resynchronization Therapy (CRT) [45]. Edvardsen et al. found that TDI-based strain estimates could detect longitudinal dyskinesia of the apical septum during LAD occlusion more reliably than standard echo [46]. In a study of patients with cardiac light-chain amyloidosis, Koyama et al. found that early impairment of systolic function could be detected by TDI-based strain estimates, even if tissue-velocity measures (i.e. pure TDI) did not demonstrate sufficient sensitivity for this task [47]. While these studies demonstrate the immense diagnostic and prognostic potential of myocardial strain estimation, it is important to note their underlying limitations. In general, because the

investigators relied on 2D echocardiography, at minimum two acquisitions would be needed in order to measure all three principal strains in some segments of the LV; for a full-chamber map of the strains, significantly more images would have to be acquired. Furthermore, because such acquisitions are limited to a single slice, there is no ability to compensate for through-plane motion, potentially resulting in underestimation of some types of strain [48]. Such underestimation is especially evident when TDI is used to assess circumferential strain, since the continuously changing direction of the deformation is incompatible with Doppler's angle-dependent nature. In healthy populations, underestimated strains may still generate valuable information, for example about LV synchrony. However, when a patient with heart disease is the subject of analysis, myocardial strain amplitudes are often low to begin with; in this case strain underestimation would lead to erroneous results and potential misdiagnosis.

RT3D echo has the potential to augment the clinical utility of myocardial strain studies via three critical refinements to the established 2D methods. First, 3D echo permits whole-chamber visualization from a single apical view, eliminating the need for acquisition of multiple sonograms. Second, the through-plane motion consideration is obviated, as the entire three-dimensional tissue of interest is observed, as opposed to specific slices. Together, these two improvements serve to augment both the reliability and reproducibility of the technique, while minimizing errors due to geometric assumptions (which are not needed in 3D). Finally, when the 3D data is processed via a speckle-tracking technique and reoriented to heart-centered coordinates, the technique becomes truly angle-independent: all three principal strains (as well as the shear strains) can be robustly quantified in the entire LV from a single echocardiogram.

Although RT3D echocardiography has been available on clinical machines for well over a decade, acceptance by physicians has been limited in large part due to insufficient image quality. Today, clinical RT3D echocardiography is still used primarily for structural (rather than functional) evaluation, i.e. for assessment of congenital heart disease [49] and valve abnormalities [50]. Functional evaluation using RT3DE is performed as well, but limited to global measures such as volume, mass and EF [51]. Some studies of functional regional analysis have also been undertaken, particularly in the context of dyssynchrony estimation in CRT patients [52] – but such applications have not yet gained wide clinical acceptance.

2.6 A Multiscale Framework for Strain Assessment

2.6.1 Challenges and Limits of Strain Measures

The demonstrated potential of strain analysis to detect clinical and even sub-clinical LV dysfunction belies several difficulties in attaining reproducible and reliable strain profiles. One reason for this is the intrinsic heterogeneity of ultrasound as a modality. Because transthoracic echo relies on intercostal and subcostal spaces to view the heart, image quality varies significantly not only between patients, but even within a single image in one patient. Artifacts such as tissue dropout, shadowing and reverberations can introduce significant noise into the image, and thus corrupt strain estimates. As this is an issue of data acquisition, it affects all subsequent post-processing techniques, whether TDI, 2D STE or 3D STE. Thus, in order to achieve more robust strain analysis, most studies have employed a manual step of excluding low-quality segments from analysis [43], [53], [54]. Naturally, the heterogeneity of image quality between patients further amplifies this problem. One study has suggested that this

limitation may preclude the use of STE in general patient populations [54].

Another source of heterogeneity is not intrinsic to ultrasound acquisition, but rather to the domain of post-processing methods. Even if we only consider block-matching STE, there is enormous variability in the specific steps used to calculate regional and global strain values. Factors such as search window size, type of matching metric, and spatial and temporal smoothing all influence the shape and amplitude of the final strain profile. For all these reasons, strain measures today still lack reliability and standard calibration methods.

2.6.2   Clinical Relevance of Strain Measurements

Many studies have demonstrated that the evaluation of LV deformation along different directions can provide important details on the pathophysiology of LV systolic mechanics beyond traditional EF assessment. Even when EF is in the normal range, the distribution and patterns of myocardial strain can be heterogeneous, reflecting a functional remodeling that has been correlated with the presence of cardiovascular risk factors such as hypertension, diabetes, coronary artery disease, and LV hypertrophy [55]-[57]. Recently, the application of deformation imaging to population studies led to the recognition of a significant proportion of LV subclinical dysfunction otherwise unrecognized by traditional assessment. Strain measurements, both in subjects with normal EF and in those with cardiac disease, are prognostically relevant, being associated with future cardiovascular events [12], [58]. Furthermore, a recent study demonstrated that LV dysfunction as measured by global longitudinal strain, even in the context of unaffected LVEF, has a distinct association with subclinical brain infarcts [59].

In patients with overt heart disease, the site of damage in the ventricular wall may differently affect specific components of LV function. In patients with ischemic heart disease, LV longitudinal strain has been shown to be specifically affected by subendocardial infarction, whereas transmural infarction is associated with depressed circumferential strain [14], [60].

Although global strain has been demonstrated to carry significant prognostic value in several clinical conditions and is able to identify degrees of subclinical dysfunction that EF cannot detect, a more regional assessment is needed when, as in ischemic heart disease, the disease process involves LV segments but global function appears unaffected. Longitudinal strain, in particular, is especially sensitive to myocardial ischemia because longitudinally oriented myofibers are predominant in the subendocardium, an area particularly vulnerable to ischemic injury. In fact, LV strain and strain rate have been shown to correlate with the presence of obstructive coronary disease even in normally contracting myocardial segments [61].

Another area of potential utility of tissue velocity and deformation imaging is LV dyssynchrony assessment in patients with heart failure or after myocardial infarction. Time differences in peak velocity or peak strain between opposing wall segments or an excessive peak velocity or strain dispersion, measured as standard deviation of the time to peak strain (TTPS) in myocardial segments, have been shown to correlate with the extent of the myocardial damage, and with the response to cardiac resynchronization therapy (CRT) [62], [63].

2.6.3 A Multiscale Spatiotemporal Framework

Despite the published validation studies, the latest expert consensus on 3D STE is that additional rigorous verification and testing are still needed [64]. Furthermore, there is a lack of agreement about specifically which strain derivatives are most useful clinically (i.e. peak radial strain, peak strain rate, dyssynchrony indices, etc.).

The commercial packages frequently used in clinical studies essentially function as black boxes, and the consequent variability in their outputs is well-documented [64]-[67]. As there is no standard calibration for any of these methods, it is difficult to establish specific quantitative criteria even for something as simple as "normal" versus "abnormal," let alone specific disease states.

The lack of consensus regarding standardized interpretation of multidimensional strain data is another immense unresolved challenge. Investigators have performed comparison studies between 2D/3D STE and both 3D MRI [53], [54], [68], [69] and sonomicrometry [43], but such comparisons still do not capture the true motion of the underlying tissue, so disagreement is to be expected. Studies that reported more promising results have only compared averaged or global values, for example taking the mean longitudinal strain across the entire LV as a metric of function. The more fundamental question, however, is which metric ought to be compared, as the LV may be characterized in a number of ways for any chosen component of the complete strain tensor. At the broadest level, on par with EF estimation, is the global average value of the strain, taken over every valid point in the ROI (i.e. after exclusion of low quality regions). More detailed analysis of the temporal progression of strain in each segment may also be

informative: a salient feature of infarcted regions is the demonstration of radial thinning during systole while healthy regions undergo thickening. This paradoxical deformation may not be obvious to an inexperienced observer, but is easily seen by visualizing the strain profiles in multiple segments.

As explained previously, the complete strain tensor exists at every pixel in the image. In segmental analysis, many pixels are averaged to decrease noise and a single value for the entire segment is generated. However, if the underlying data is sufficiently reliable, averaging should be avoided (as it could be detrimental), and a truly full-resolution strain map of the LV should be generated. Such high-resolution maps are considerably more complex, but employ the full extent of the acquired data, permitting delineation of more localized phenomena. In Figure 2-5, we summarize the multiple spatial and temporal scales at which LV function should be analyzed, starting from the coarsest global-level measurements and extending to the voxel scale.

In the chapters that follow, we will demonstrate the effectiveness and convenience of using this framework to explore the strengths and shortcomings of the OF approach to 3D strain estimation in the LV. It will become clear to the reader that this framework bridges the gap between the "bench" and "bedside" ways of thinking about the meaning and significance of LV strain.
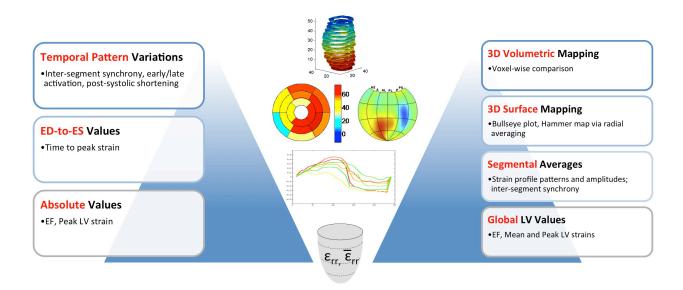
Figure 2-5. A proposed framework for analyzing LV strain from RT3D echocardiograms and comparing against results from other imaging modalities or clinical markers. The temporal scales are shown on the left; the spatial scales are shown on the right.

The issue of validation remains unresolved. As detailed above, numerous studies have attempted to demonstrate the accuracy, reproducibility, and robustness of LV strain measures by various means. Nevertheless, as of today, we are unaware of any published study describing the results of the "ultimate" validation procedure, whereby all 3D strain components measured by STE are compared to a gold standard such 3D tagged MRI on a pixel-by-pixel basis. Such a study, performed on human subjects, would definitively prove the adequacy or inadequacy of the proposed STE technique in estimating true LV strains in humans. Performed exclusively on a large population of healthy subjects, the study would provide a reference or calibration metric for what ought to be considered normal values. By extension, inclusion of specific disease populations (along with properly matched normal controls) would permit us to evaluate whether the method offers any added-value (i.e. greater sensitivity or specificity) over the

38

existing clinical paradigm. The evidence generated by such investigations will form the foundation upon which broader criteria on the interpretation of echocardiography-based strains may be developed. Only once such guidelines are enacted by authoritative organizations will strain measurements begin to gain traction in the cardiology clinic.

Although there are still numerous technical and practical challenges to executing this "ultimate" validation study for the OF strain estimation technique, we have taken several critical steps toward achieving this lofty goal. The details and results of these steps are the focus of the next four chapters.

Chapter 3. Feasibility of Myocardial Strain Assessment in the Human Left Ventricle by

Three-Dimensional Echocardiography Using Optical Flow

3.1 Introduction

As noted in the previous chapters, echocardiography remains the mainstay of clinical diagnosis for a variety of cardiac diseases, including heart failure [70], coronary artery disease (via stress echo) and valvular heart disease (via Doppler [71] and 3D echo [50], [72]). Recently, technological advances and the introduction of new post-processing algorithms applied to cardiac ultrasound imaging have allowed the quantification of regional myocardial deformation, expressed mathematically as strain. 2D myocardial strain measures, derived from tissue Doppler [73] and speckle tracking methods [74] have proven useful in detecting cardiac dysfunction and predicting cardiovascular outcomes in a wide variety of cardiac pathologies [75]. Analysis of cardiac function from 2D images, however, has several limitations: it requires multiple acquisitions over different heartbeats, it samples only the portion of cardiac tissue included in the ultrasound plane, it cannot account for out of plane motion, and the analysis of the large number of 2D images required to cover all myocardial segments can be extremely time-consuming.

Though RT3D echocardiography overcomes most of the disadvantages of 2D echocardiography, its widespread clinical acceptance has been delayed by several factors. These mainly relate to technical limitations of first-generation 3D systems that result in insufficient image quality for clinical purposes and low temporal resolution compared to 2D images. Over time, many of these have been resolved or improved, and today RT3D echocardiography has become an important aid in clinical practice, particularly in the fields of cardiac valve assessment, ventricular functional assessment, and atrial structure and function.

The study of myocardial deformation in 3D has the potential to become a useful tool in cardiology thanks to its advantages over 2D, as detailed above.

Previous studies, including several reports produced by our group, have demonstrated that RT3D echo can characterize myocardial strain in 3D using "speckle tracking" [18], [19], [44], [68], [69], [76], [77]. In our earlier work, we introduce an Optical Flow (OF)-based technique for 3D strain estimation [17], and validated the method on simulated B-mode echocardiograms [18]. Subsequently, we performed a series of animal experiments to demonstrate that strain can be measured accurately *in-vivo* [19], and that such measures can be used to detect ischemic and infarcted tissue [77]. Furthermore, we have described some of the necessary optimizations for our processing pipeline in order to extract such measures from human subjects in a clinical setting [78]. A number of studies in human subjects have demonstrated the utility of 3D strain measurements using commercially available strain analysis software. Although commercial speckle tracking software tools often function as a "black box," – meaning that the exact computational steps leading from input to strain measures are either unknown or unmodifiable by the end user – strain estimates are usually derived from tracking of the LV subendocardial surface (after automatically or manually delineating the endocardial border). However, it is well-known that LV strain exhibits transmural gradients [79], [80]; the ability to quantify such patterns using echocardiography could significantly improve our understanding and diagnosis of ventricular dysfunction.

Our aim in the present work is to evaluate the feasibility of applying our strain estimation pipeline on data from human subjects, acquired in a clinical setting. The technique we describe

is distinct from the aforementioned ones in that it calculates true 3D strains, taking into account the entire myocardium of the LV. In the following sections, we will address the critical considerations in adapting our technique to work with human data; describe the acquisition and post-processing protocols; and assess the feasibility of strain analysis using RT3D and OF in a population of healthy individuals.

3.2 Materials and Methods

3.2.1 Study Population

We prospectively recruited a total of 19 healthy individuals. Subjects were included in the study if they had: (1) no history of cardiac symptoms, hypertension or diabetes, (2) no use of medication with primary cardiovascular effects or known cardiovascular side effects, and (3) normal physical exam findings. We excluded subjects who were below the age of 18 years or who had any history of smoking, ischemic heart disease or non-sinus cardiac rhythm, as well as those who exhibited abnormal findings on 2D echocardiograms during the study. Recruitment of all subjects was performed with the approval of Columbia University's Institutional Review Board (IRB), as were all successive steps in the remainder of the protocol, as detailed below. Written informed consent was obtained from all study participants.

3.2.2 Data Acquisition

All studies were conducted using a Philips iE-33 machine equipped with an X5-1 matrix array probe (Philips Medical Systems, Andover, MA, USA). After 10 minutes resting in the supine position, each participant's heart rate and blood pressure were measured. The

echocardiographic exam was then performed according to the recommendations of the American Society of Echocardiography by a licensed technician with the subjects in the left lateral decubitus position. A series of standard 2D B-mode images were visualized and acquired, then used for visual confirmation of normal LV function in each participant. For 3D assessment, a full volume acquisition of the entire LV in 3D was obtained from an apical approach, optimizing the depth and elevation width of the field-of-view (FOV) to maintain the frame rate ≥30 Hz. Four 3D B-mode volumes were acquired in four consecutive beats, using ECG triggering and real-time stitching to create the full 3D view. To achieve the best possible image quality, all views were acquired under apneic conditions. To minimize inter-observer variability, the same technician performed the scans for each subject.

3.2.3 3D Strain Analysis with Optical Flow

The pipeline for strain estimation from RT3D echocardiograms using our OF technique is shown in Figure 3-1. First described by our group in [44], [77], [78], the pipeline has been adapted from its initial use in open-chest canine experiments to handle the particularities of transthoracic echo (TTE) in humans.
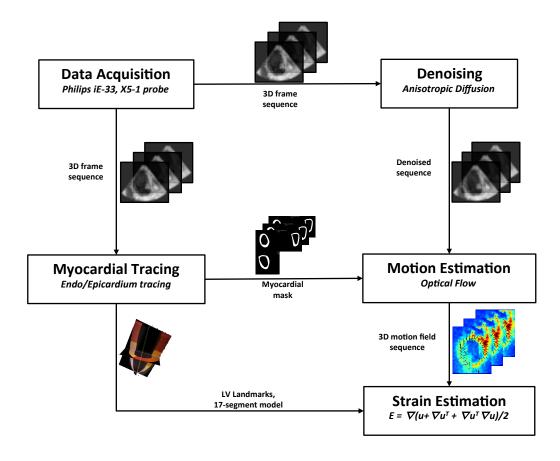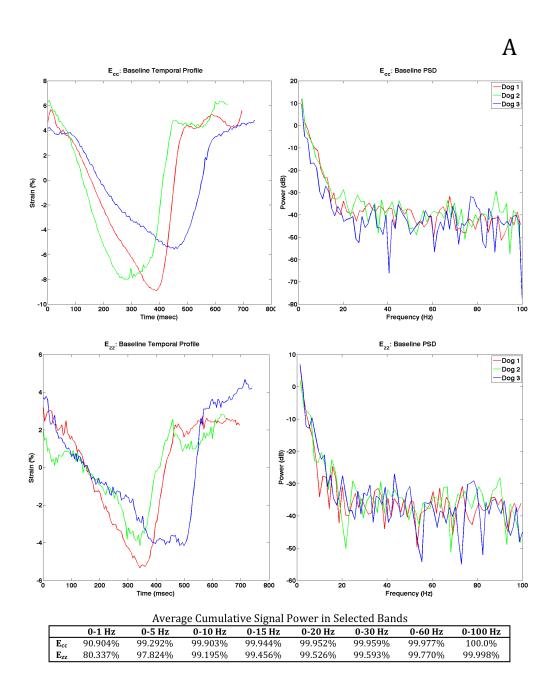
Figure 3-1. Optical Flow pipeline for strain estimation from human 3D B-mode echocardiograms.

Acquisition

In order to ascertain whether our acquisition frame rate would be sufficient to capture the rapid dynamics of LV deformation, we performed a frequency-spectrum analysis of the canine sonomicrometry data acquired in earlier experiments [19]. A summary of the results from three canine experiments is shown in Figure 3-2. The strain curves were derived from sonomicrometry crystal data, which were acquired at f_s = 200 Hz. We analyzed the power spectral density of each signal, calculating the proportion of signal contained within different frequency bands. We additionally tested subsampling of the original data at one-tenth of the

original acquisition rate, and low-pass filtering with a 30Hz cutoff to evaluate the effect of lower

frame rate on visualizing the characteristics of interest of the temporal strain profile (Figure 3-3

and Table 3-1).

E_{cc}: Baseline Temporal Profile

E_{cc}: Baseline PSD

E_{zz}: Baseline Temporal Profile

E_{zz}: Baseline PSD

Average Cumulative Signal Power in Selected Bands

	0-1 Hz	0-5 Hz	0-10 Hz	0-15 Hz	0-20 Hz	0-30 Hz	0-60 Hz	0-100 Hz
E_{cc}	90.904%	99.292%	99.903%	99.944%	99.952%	99.959%	99.977%	100.0%
E_{zz}	80.337%	97.824%	99.195%	99.456%	99.526%	99.593%	99.770%	99.998%

	0-1 Hz	0-5 Hz	0-10 Hz	0-15 Hz	0-20 Hz	0-30 Hz	0-60 Hz	0-100 Hz
E_{cc}	52.804%	95.672%	99.002%	99.411%	99.490%	99.563%	99.711%	99.995%
E_{zz}	90.274%	97.448%	98.839%	99.090%	99.219%	99.341%	99.650%	99.996%

Average Cumulative Signal Power in Selected Bands

Figure 3-2. Spectral analysis of temporal strain profiles from three canine experiments. (A) Left: Circumferential and longitudinal strain curves from three canine experiments, depicting function at baseline (healthy tissue). Right: Power spectral density graphs for each curve. The table exhibits the amount of signal power in selected frequency bands, averaged over the 3 cases. Note that > 99.6% of signal power is concentrated below 30Hz. (B) Left: Circumferential and longitudinal strain curves from three canine experiments, depicting function after pLAD occlusion leading to infarction. Right: Power spectral density graphs for each curve. Note that > 99.3% of signal power is concentrated below 30 Hz.
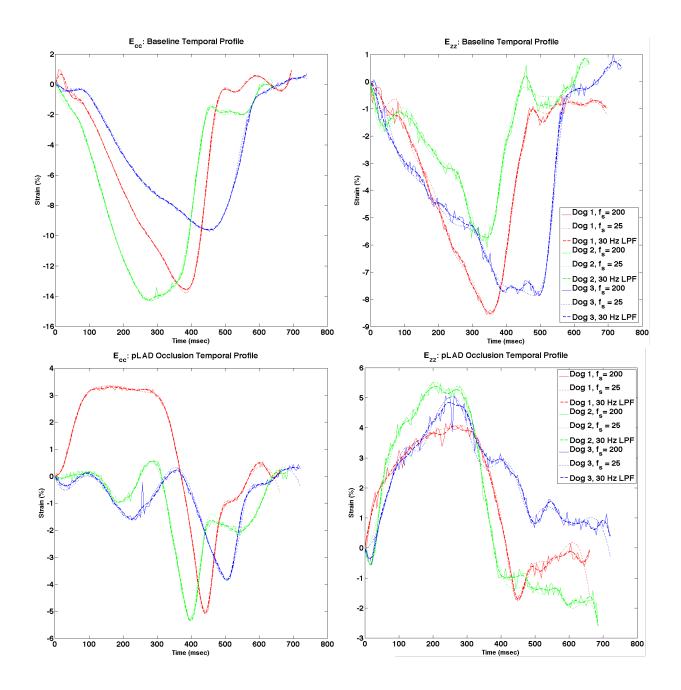
Figure 3-3. Circumferential and longitudinal temporal strain curves in three canine data sets, both shown at the acquisition frequency (200Hz), after 25 Hz subsampling and spline interpolation, and after low-pass filtering with a 30Hz cutoff

In all cases, the subsampled and interpolated curves directly overlay the original data, suggesting that a lower sampling rate may be adequate.

We further validated this hypothesis using RT3D data acquired from 5 healthy volunteers at

four sampling rates, f_s = [15, 25, 30, 35] Hz. The details of this experiment are described in [81].

In sum, we found that measured displacement and strain amplitudes are sensitive to the acquisition frame rate, with significantly higher amplitudes being observed at f_s = 35 Hz versus 15 and 25 Hz. There was, however, no appreciable difference in the strain amplitudes or patterns between f_s = 30 Hz and f_s = 35Hz. Because of the trade-off between FOV and f_s, we maintained a frame rate of ≥ 30 Hz during acquisition.

Table 3-1. Effects of subsampling-and-interpolation, and low-pass filtering (LPF) on canine strain curve characteristics reported as average differences (Δ) of peak values and time to peak strain (TTPS) values.

	Baseline Condition			pLAD Occlusion Condition		
	Mean ± SD	Δ vs. Interpolated	Δ vs. LPF	Mean ± SD	Δ vs. Interpolated	Δ vs. LPF
E_{cc} peak (%)	-7.49 ± 1.73	0.03	-0.06	-4.35 ± 1.45	-0.01	0.02
E_{zz} peak (%)	-4.55 ± 0.67	-0.09	-0.15	3.16 ± 0.87	0.03	0.15
E_{cc} TTPS (msec)	376 ± 84	5	5	445 ± 53	-2	-2
E_{zz} TTPS (msec)	394 ± 90	5	-2	225 ± 20	-22	-13

Denoising

In our framework, anisotropic diffusion [82] is used to improve image quality in the RT3D scans before tracking is attempted. Briefly, when applied to an image, the anisotropic diffusion filter models a heat-diffusion process, effectively "homogenizing" the pixel gray levels in the same way a gas or liquid achieves homogeneity through physical diffusion. In the implementation described by Duan et al., a 3D+time image *I(x, y, z, t)* is filtered using a heat diffusion equation of the form

$$\frac{\partial I}{\partial t} = div(c(x, y, z, t)\nabla I),$$

(3.1)

where $c(x,y,z,t)$ is the diffusion parameter, div is the divergence operator, and ∇I is the gradient of the image intensity. As the diffusion parameter is not constant, this equation represents a nonlinear process. More specifically, the diffusion parameter is set to vary with the gradient of the image data [83]:

$$c(x, y, z, t) = g(|\nabla I(x, y, z, t)|).$$

(3.2)

The function g, controls the diffusion as follows [84]:

$$g(x, \lambda) = \begin{cases} 1 & x \leq 0 \\ 1 - e^{-\frac{3.315}{(x/\lambda)^4}} & x > 0 \end{cases}.$$

(3.3)

The only parameter of this function, λ, is essentially a gradient threshold for edges. Following the work of Montagnat et al. [85], Duan proposed that this gradient threshold ought to evolve linearly in time, in order to avoid reductions in the magnitude of strong edges in the image as homogeneous regions undergo filtering. Thus, the final component of the model is:

$$\lambda(t) = \lambda_0 + at,$$

(3.4)

where λ_0 is an initial gradient value, a is a slope parameter, and t is the time index. In sum, the behavior of the anisotropic diffusion model is based on these last two parameters, whose values must be adjusted based on the image quality (e.g. amount of noise in the data).

Optimization of this filter for transthoracic imaging was described in [86]. In that report, denoising parameters were studied using human data (N = 10) acquired on a Siemens ACUSON

51

SC2000™ with a matrix phase-array 4Z1c transducer. It was determined that the optimal initial gradient value λ_0 was in the range of *6 to 10*. Note that the slope parameter is empirically set to *-1* while the time interval is *0.05* for *4* iterations.
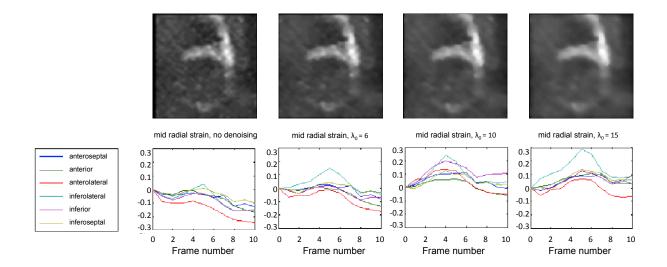
Figure 3-4. Demonstration of the effect of anisotropic diffusion upon RT3D TTE B-mode data and upon the resulting radial strains computed in the mid LV segments in the systolic phase, without denoising and with the initial threshold $\lambda_0 = 6, 10, 15$.

Due to our use of a different machine and probe, we repeated the study to find the optimal parameters for data from the Philips iE-33 machine. Consistent with our previous findings, we observed that the better image quality on the Philips machine required less denoising (e.g. a lower initial threshold $\lambda_0 = 4$). Consequently, we applied a low level of denoising across all cases in this study.

Myocardial Tracing and Landmark Selection

The OF speckle tracking algorithm relies on an initial set of known tissue points in the FOV. These points are selected by manual delineation of the endo- and epicardial borders at end-

52

diastole (ED) by an expert trained in cardiac TTE interpretation. To transform data from the Cartesian (*x, y, z*) system to the natural coordinate system of the LV (*r, ϑ, z*), we manually identify the apex, the center of the mitral valve, and the mid-septum. The principal LV *z*-axis is then defined as the apical-mitral line, whose position is assumed to be stable throughout the cardiac cycle [87]. The coordinate transform from pixel coordinates (*i, j, k*) to anatomical coordinates (*x, y, z*) is performed as follows:

$$
\begin{bmatrix} x \\ y \\ z \end{bmatrix} = R \begin{bmatrix} i \\ j \\ k \end{bmatrix} + T = \begin{bmatrix} r_{11} & r_{12} & r_{13} \\ r_{21} & r_{22} & r_{23} \\ r_{31} & r_{32} & r_{33} \end{bmatrix} \begin{bmatrix} i \\ j \\ k \end{bmatrix} + \begin{bmatrix} O_i \\ O_j \\ O_k \end{bmatrix}
\tag{3.5}
$$

where *R* is the rotation matrix aligning the *z*-axis with the long-axis, and *T* is the translation vector defined to position the center of the anatomical coordinates at the center of the mitral valve. Myocardial tracing and landmark identification are the only two manual and patient-specific steps in the pipeline.

Motion Estimation with Optical Flow

The method of tissue tracking with OF using a cross-correlation metric has been extensively described [88], [89]. Our implementation uses spatial cross-correlation across consecutive volumes to estimate motion. The normalized cross-correlation coefficient to be maximized is defined as:

$$CC = \frac{\sum_{x \in \Omega} \left(I(\boldsymbol{x},t) \cdot I(\boldsymbol{x} + \Delta \boldsymbol{x}, t + \Delta t) \right)}{\sqrt{\sum_{x \in \Omega} I^2(\boldsymbol{x},t) \sum_{x \in \Omega} I^2(\boldsymbol{x} + \Delta \boldsymbol{x}, t + \Delta t)}}$$

$$(3.6)$$

where *I* represents the volumetric image at consecutive times *t* and *t+Δt*, *Δx* represents the displacement of a pixel *x*, and *Ω* is a small neighborhood around the pixel *x*. A graphical explanation of this block-matching technique is shown below, for both 2D and 3D cases.
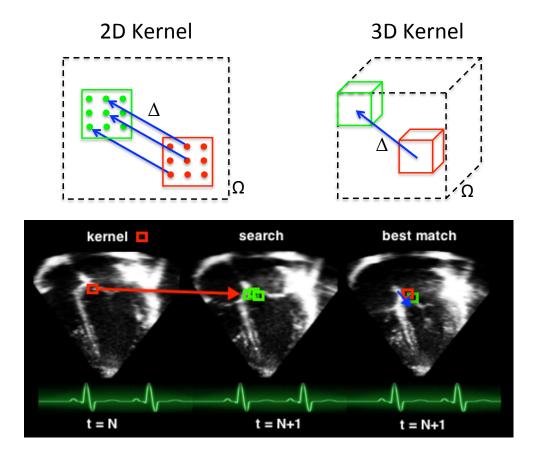
Figure 3-5. Tissue tracking with Optical Flow in 2D and 3D. A kernel or template region (red) is selected around a particular tissue point at time N; at time N+1, the tissue point has moved, so a search is conducted in the neighborhood Ω (black dotted region); the best match at N+1 is taken to be the location within Ω with the highest cross correlation (green). The displacement Δ can then be calculated by simple subtraction of the tissue point coordinates at time N and time N+1.

As the reader can appreciate from the equation and diagram, the OF method must be provided with two critical parameters: the size of the template (kernel) and the size of the

54

search region. The choice of kernel size depends in part on the amounts of speckle and noise present in the image. In addition, the kernel size determines the resolution of the resulting displacement map. Meanwhile, the size of the search region depends on how far the tissue is expected to move between frames. A tradeoff with accuracy and computational speed must be made: choosing a very small search region is computationally efficient, but increases the risk that the tissue point will move outside this area, making it impossible to obtain an accurate result. Alternatively, one may choose a very large search region, ensuring that the tissue point cannot move beyond its bounds. However, this carries two disadvantages of its own: first, the computational cost increases exponentially with the size of the search region, and second, the abundance of potentially good matches in a large search area increases the likelihood of choosing an erroneous point. Thus, for a given range of image quality and expected physical motion, there exists an optimal set of parameters to maximize the accuracy of tracking while reducing computational costs.

In [86], we examined the effects of template region and search window dimensions on motion and strain estimates from human data. The findings are summarized in Figure 3-6. We determined that for LV motion tracking, the optimal values are 7×7×7 voxels (4.8 mm^3) for the template size around a pixel and 9×9×9 voxels (6.1 mm^3) for the search region Ω.
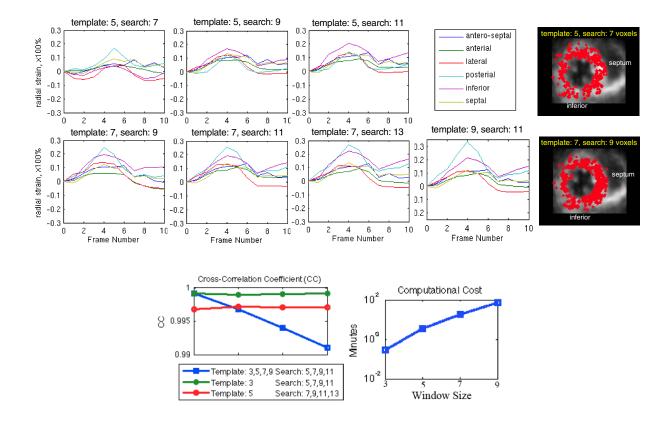
Figure 3-6. (Top) Examples of temporal radial strain profiles estimated at the mid level of the LV using various kernel and search region sizes during OF tracking. (Bottom) Effects of variable kernel and search region sizes on the cross correlation coefficient and computational cost of OF tracking.

Since OF tracking relies on the accuracy of the previous frame, errors tend to accumulate over the course of time. Thus, tracking is most accurate at the beginning of the cardiac cycle (the ED phase, in this case). We address this problem by observing that the first and last frames in the cycle are identical, and can therefore be tracked both forward and backward using the same myocardial mask from ED. The forward (*fwd*) and backward (*bwd*) displacement estimates *u* can then be combined as a weighted average:

$$u(t_i) = \frac{(t_{max} - t_i) \cdot u_{fwd} + t_i \cdot u_{bwd}}{t_{max}}$$

(3.7)

so that the relative weight of each displacement estimate is inversely proportional to its temporal distance from the initial and final ED frames. Lastly, the displacement field is spatially regularized using 3D cubic splines polynomial fitting, which enhances the spatial coherence of the estimated displacements [81].

Strain Estimation

We calculate strain as the spatial gradient of the displacement. The strain tensor is calculated as

$$E = \frac{1}{2}\left(\nabla u + \nabla u^T + \nabla u^T \nabla u\right)$$

(3.8)

where *u* represents 3D displacements, and the diagonal values of E contain the radial (E_{rr}), circumferential (E_{cc}), and longitudinal strain (E_{zz}) components [90].

We chose to examine strain estimates at the global and segmental levels (using the 17 segment AHA model of the LV [22]), which have been shown to have important clinical correlates [13], [91], and correspond well to established 2D TTE analysis. We therefore calculated the peak E_{rr}, peak E_{zz} and peak E_{cc}, and the corresponding time-to-peak strain (TTPS) for each subject. As noted previously, transthoracic RT3D image quality is highly heterogeneous not only across individuals but even within a single subject. For example, in many subjects, the anterior wall of the LV is either poorly visualized or completely absent from the image (Figure

3-7). Thus, we asked an expert to grade the visual quality of each LV segment, based on whether the segment could be interpreted in a standard TTE reading. Since segments with poor quality cannot be reliably tracked, they were removed from individual analysis. When considering values across subjects, we also excluded segments which were of poor quality in ≥ 80% of cases.
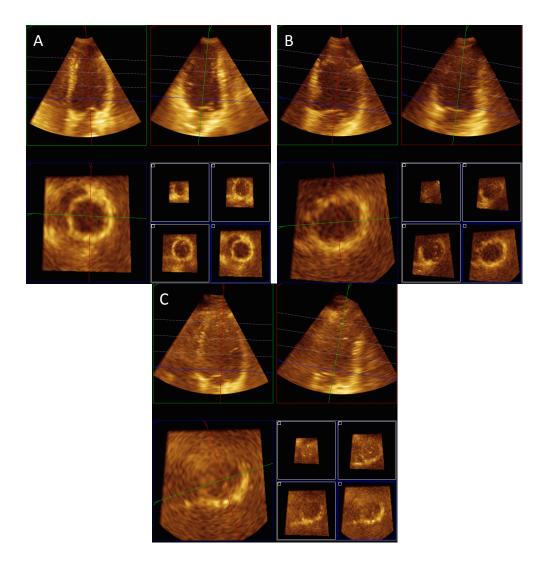
Figure 3-7. Image quality on RT3D scans in three subjects: (A) example of a study with adequate quality for OF-based tracking and diagnostic assessment in most segments except the apical anterior wall; (B) example of a study with regional inhomogeneity in quality – all six basal segments are considered adequate, while the mid-anterior and mid-inferolateral segments are poorly seen; (C) example of a study with poor quality throughout the LV; only the inferior wall and basal/mid lateral wall are well seen.

3.2.4 Statistical Analysis

Measures are expressed as mean ± standard deviation (SD). For all statistical analyses, a two-tailed $p < 0.05$ was considered significant. To account for variable heart cycle lengths among subjects, we applied temporal normalization, using the effect size (ES) frame as a reference to align curves along the time axis.

In the first stage, we sought to establish the range and variability of strain as measured by RT3D and OF in healthy subjects. In accordance with the framework we proposed in [92], we first examined the distribution of peak global strains and the TTPS at a global level (whole LV) and then at individual segment levels, computing average temporal profiles for each segment, based on the estimated strains.

3.3 Results

With respect to the canine study, Figure 3-2 shows the baseline and infarcted strain curves from canine data, and their respective power spectra. The PSD plots verify that most signal power lies in the low-frequency bands. Table 3-1 and Figure 3-3 summarize the results of the sampling frequency validation study using canine strain data. These data illustrate that important parameters such as peak strain and TTPS were largely unaffected by subsampling and low-pass filtering of the data.

With respect to the human study, the demographics of the study sample are shown in Table 3-2 On average, each subject had 12.0±2.9 LV segments with adequate quality in RT3D studies.

The segments with the lowest quality were: apical anterior, apex, apical lateral, mid anterior and basal anterior. After exclusion of segments that were inadequate in ≥ 80% of the study sample, subjects had on average 8.25±0.95 analyzable segments (maximum per subject = 9, minimum per subject = 8, total segments = 256). The average frame rate was 32.7 ± 1.1 Hz (one study at 28 Hz).

Table 3-2. Demographics and clinical data of the subjects included in the human study sample.

N	19
Age (years)	28.6 ± 5.0
Gender (M/F)	10/9
BMI (kg/cm^2)	23.1 ± 4.5
Systolic BP (mmHg)	123.4 ± 12.5
Diastolic BP (mmHg)	76.6 ± 9.6
Heart Rate	71 ± 10
3D EF (%)	60.9 ± 4.8

In Table 3-3, we summarize the global LV strain parameters measured in the healthy population. We verified that the values were normally distributed within the population. The coefficients of variation for all the six studied strain variables are quite high, between 25% and 51%.

Table 3-3. Global peak strain estimates by OF in the study sample.

Variable	Mean ± SD	CV
E_{cc} (%)	-19.4 ± 6.6	34%
E_{rr} (%)	59.4 ± 23.3	39%
E_{zz} (%)	-19.8 ± 6.6	33%
$TTPS_{cc}$ (msec)	414.7 ± 210.9	51%
$TTPS_{rr}$ (msec)	316.9 ± 80.4	25%
$TTPS_{zz}$ (msec)	387.7 ± 181.2	47%

In Figure 3-8 we demonstrate the averaged principal strain components in each of the LV segments which were of adequate quality across the volunteer population. Variation among subjects is reflected in the error bars: vertical error bars at each time point represent the 95% confidence interval (CI) for strain amplitude while the horizontal error bar represents the 95% CI for the TTPS in that segment. While we observed low strain amplitudes in the circumferential component, the longitudinal and radial deformations showed consistent spatial patterns and variability that was within previously published limits.

Temporal profiles and levels of variability vary greatly between segments. For example the mI segment exhibits very low E_{rr} and E_{zz} values which do not seem to agree with measures from other segments. The TTPS also varies greatly between segments, being more consistent for the E_{zz} component. Distinguishing strain values, we observed that for E_{cc}, values are generally low, and show significant variability (wide CIs). Notably, there are similarities in the temporal progression and amplitude among segments belonging to the same wall of the LV (e.g. *IS and *AS curves). E_{rr} curves demonstrate higher amplitudes across all segments, but there is still considerable regional variation. The situation is similar for E_{zz} curves. Overall, the variability of measures is not uniform across all segments – even after exclusion of regions with poor image quality, the width of the CIs fluctuates considerably among the displayed segments. In Table A-1, we summarize the variation in peak values and TTPS for each of the analyzed segments.
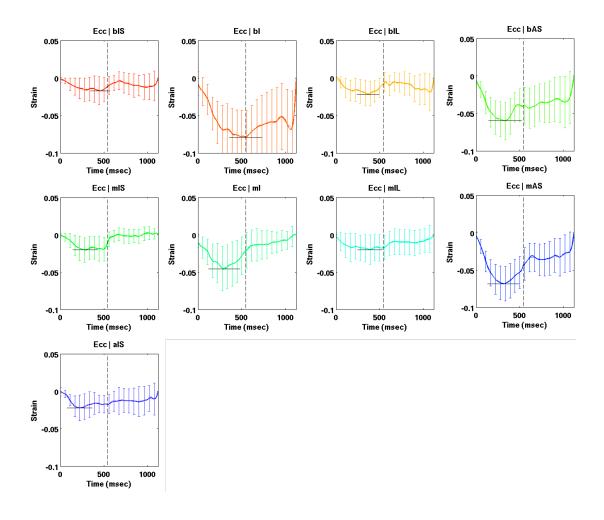
Figure 3-8a. Average temporal curves of circumferential strain for each segment in the study population. Vertical error bars represent the 95% CI for amplitude. The horizontal error bars at the peak of each curve represents the 95% CI for the TTPS. The dotted line denotes ES time, which was used to temporal alignment of subjects.
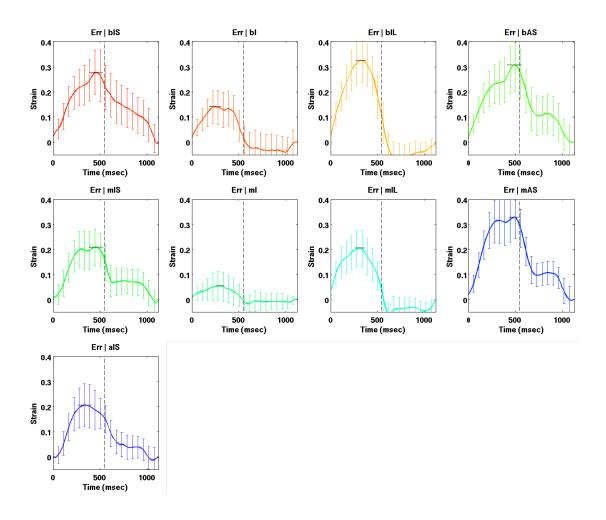
Figure 3-8b. Average temporal curves of radial strain for each segment in the study population. Vertical error bars represent the 95% CI for amplitude. The horizontal error bars at the peak of each curve represents the 95% CI for the TTPS. The dotted line denotes ES time, which was used to temporal alignment of subjects.

63
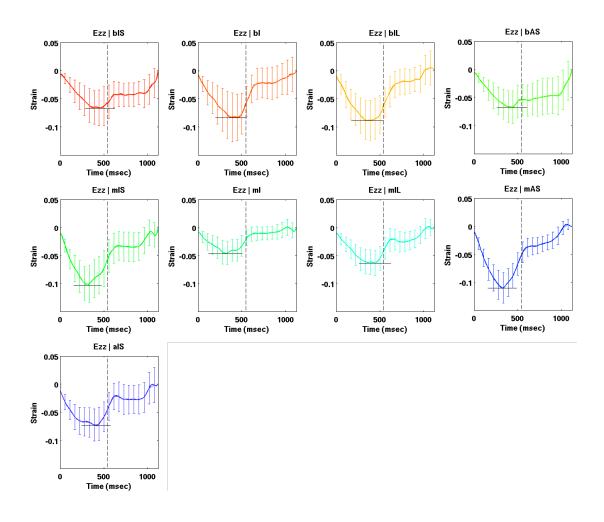
Figure 3-8c. Average temporal curves of longitudinal strain for each segment in the study population. Vertical error bars represent the 95% CI for amplitude. The horizontal error bars at the peak of each curve represents the 95% CI for the TTPS. The dotted line denotes ES time, which was used to temporal alignment of subjects.

We examined scatter plots of the CIs and strain amplitudes and plotted the average width of the CI at each time point, for each of the three strain components (Figure 3-9).
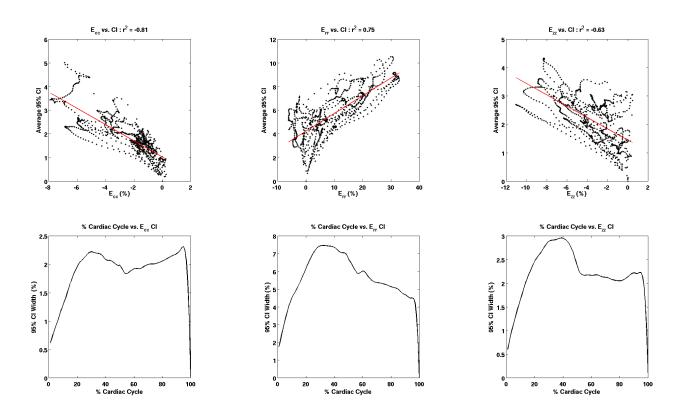
Figure 3-9 (Top row) Strain 95% CI width as a function of strain amplitude. (Bottom row) Strain 95% CI width as a function of time.

The graphs demonstrate that the widest CIs are both strongly dependent upon strain amplitude, and tend to occur in the mid-systolic portion of the heart cycle, when motion and deformation are most rapid.

3.4 Discussion

There is growing evidence describing the utility and advantages of myocardial strain assessment in 3D [93]-[96]. An important characteristic of all the aforementioned studies is that they relied on a 3D strain estimation method that captures only the subendocardial surface. By contrast, a central feature of the method we have described is estimation of strain by

consideration of the entire myocardium. In conjunction with improved image quality, the ability to measure myocardial strains in 3D confers several major advantages over existing 2D methods. Specifically, key limitations such as out-of-plane motion, angle-dependence, and the need for multiple acquisitions are rendered moot by imaging the entire heart chamber in 3D from a single (apical) location. Examination of the entire LV, rather than single slices, permits the visualization and quantification of the inherently complex motion and deformation patterns of the myocardium. Moreover, 3D analysis has the potential to be significantly less time consuming than 2D, as only one dataset needs to be analyzed compared to the several datasets acquired for 2D assessment.

We expect that RT3D will provide all the benefits afforded by 2D myocardial strain estimation, augmented by examination of deformation patterns in their native 3D orientation. The efficiency of RT3D imaging bears additional emphasis. Acquisition of multiple 2D views is 2-3 times longer, and still produces an incomplete portrait of LV function. By contrast, RT3D acquisition can be performed from a single apical location over 4 heartbeats, and captures the entire LV. One drawback of RT3D is the lower frame rate (~30 Hz) compared to 2D echocardiography (typically 60-70 Hz, or higher in a constrained FOV). As faster and more advanced 3D ultrasound probes are developed, this disadvantage is likely to diminish or vanish entirely. The increase in frame rate will in all probability improve the tracking of myocardium, as our previous experiment suggests [81].

3D strain measurements derived from RT3D echo images have shown promise in a variety of clinical diagnostic scenarios. Ozawa et al. demonstrated that 3D global longitudinal strain can

distinguish normal individuals from hypertrophic cardiomyopathy patients [94]. Kaku et al. performed an initial validation of a 3D strain analysis technique in a range of healthy individuals, demonstrating that strain amplitudes and patterns change with age [93]. Meanwhile, a study by Pedrizzetti et al. suggested that principal strain analysis of RT3D echocardiograms is suitably sensitive to the subtle changes in LV deformation resulting from hypertension [95]. We believe that a method capable of analyzing the entirety of the LV myocardium may create a significant advantage by providing data at the voxel level – thereby facilitating measurement of transmural strain patterns.

The current study primarily focused on (1) adapting the method of RT3D strain estimation with OF to data acquired in a typical clinical setting, (2) determining the range of variation in 3D strain estimates among healthy human subjects, and (3) establishing whether the technique may be used at the segmental level to quantify the heterogeneity of strain measures.

Pipeline Optimization

In previous studies, our group described some aspects of the pipeline optimization (selection of parameters for anisotropic diffusion and OF tracking). Here we present analysis of the acquisition parameters, specifically with regard to acceptable frame rates and image quality. In a previous study in open-chest dogs, examination of the frequency spectra of the "ground truth" strain profiles revealed that the majority of signal power is concentrated in the low frequency bands, with ≥ 99.4% of the signal in the 0-30Hz range. As summarized in Figure 3-2, there were no significant differences in the power spectra of baseline (healthy) and experimental (infarcted) canine myocardial regions. Although the dynamics of human

myocardium are not identical to canine tissue, this experiment suggested that acquisition rates of 25-35Hz would be sufficient for capturing the principal characteristics of the temporal strain profiles. We also confirmed that neither subsampling of the original signals at 20 Hz followed by interpolation, nor low-pass filtering of the data with a 30 Hz cut-off, altered their shapes or key characteristics (e.g. peak value and TTPS). Table 3-1 provides a quantitative summary of the results depicted in Figure 3-3: while applying a low-pass filtering produced larger deviations from the original signal, peak amplitude estimates remained within 1-5% of the original; TTPS estimates showed slightly larger differences, which were at most 10% in the case of longitudinal TTPS in infarcted tissue.

We interpret our results on canine data as evidence that, from a theoretical and physiological standpoint, the maximum-achievable frame rate of 30-33 volumes per second ought to be sufficient for capturing the clinically established characteristics of LV strain in humans. Nevertheless, we acknowledge that this analysis does not take into account the differences between human and canine LV function, nor the additional complications arising from TTE imaging – generally lower image quality, a limited field of view, and lower frame rates. We mitigate the former two complications by meticulous positioning of the patient and transducer, acquisition of data under apneic conditions, and a specialized denoising technique.

Evaluation of LV Strain: Global Approach

As recommended in [92], we characterized OF-based LV strain with a multi-scale approach. We first determined the range of variation in strain observed by this method at the global spatial and temporal scales. As seen in Table 3-3, when considering parameters such as global

peak strain and global TTPS, the values measured in healthy volunteers generally agree with previously reported data [93], [97]. Muraru, et al. reported the following reference values (as first and third quartiles), which were based on data acquired with a GE Vivid E9 scanner (GE Vingmed Ultrasound AS, Horten, Norway) and analyzed using the Q-Analysis package (EchoPAC BT12; GE Vingmed Ultrasound AS): -17% to -21% for E_{zz}, -17% to -20% for E_{cc}, and 47% to 59% for E_{rr} [97]. Kaku, et al. used a Sonos 7500 or iE33 scanner with an X5-1, X4, or X3-1 transducer (Philips Medical Systems, Andover, MA), and estimated strains using 4D LV analysis software from TomTec Imaging Systems. They reported the following 3D strain values from a healthy cohort: -20 ± 3.2% for E_{zz}, -28.9 ± 4.6% for E_{cc}, and -37.6 ± 4.8% for E_{rr}. We note that these values are quite close to the range we have observed, though our data may exhibit more variability, because the method of strain estimation is considerably different. While we verified that the values were normally distributed within the population, the standard deviations of the peak strains, representing 34-39% of the mean, suggest that a "normal" range of values might not be identifiable for the clinical task of distinguishing abnormal subjects and quantifying subtle changes in LV function. Non-focal pathologies such as LV hypertrophy are known to hamper global strain components [98], [99]; however, detection of regional abnormalities in LV function — which we believe to be an important application of our method — may not always be detected by global indices, since a localized reduction in function may not push the patient's global value outside the normal range. This idea forms the rationale for the segmental approach described below. The great variability between segments suggests that normal ranges of values and analysis of strain profiles need to be performed at the segmental level, and not globally.

Evaluation of LV Strain: Segmental Approach

While one contributor to the observed differences between segmental results is the natural variation in function among individuals, image quality may be a factor as well. The binary classification we utilized to distinguish "adequate" and "inadequate" segments does not account for the wide range of visual quality seen among patients. Because the technique evaluates strain across the entire thickness of the myocardium, transmural gradients may contribute to the heterogeneity of the measures. Nevertheless, when considered in the context of previously reported 3D strain in healthy volunteers, the variability of our measures is within range of what is considered acceptable.

Since the metrics in which we are most interested tend to occur near the end-systolic phase, error accumulation from ED may play a non-trivial role in peak strain calculation. Although the forward-and-backward tracking approach described above serves to mitigate error accumulation throughout the cardiac cycle, the peak strains occur in the middle frames, which are naturally the most error-prone since they are farthest from the initialization frame.

With respect to measurement of TTPS at the segmental level, we observe that the 95% CIs for each segment mirrored the pattern at the global scale – that is, the intervals were widest for the longitudinal and circumferential deformations, and relatively narrow for the radial component. The absence of spatial patterns akin to what was observed for strain amplitudes suggests that the calculations were affected by something other than regional image quality. We conjecture that, contrary to the results of the canine data experiments, the frame rate we used may be insufficient to reliably characterize the most rapid deformation phenomena,

70

leading to the wide standard deviations and CIs observed in the population. In this context, it is important to note that although TTPS values have been documented [100], the clinical significance of TTPS is not well established; the primary focus is typically on synchrony measures derived from TTPS, particularly in patients undergoing CRT [41]. Moreover, TTPS measures derived from our canine data, which were acquired under "ideal" conditions, also showed significant variation even in healthy myocardial tissue.
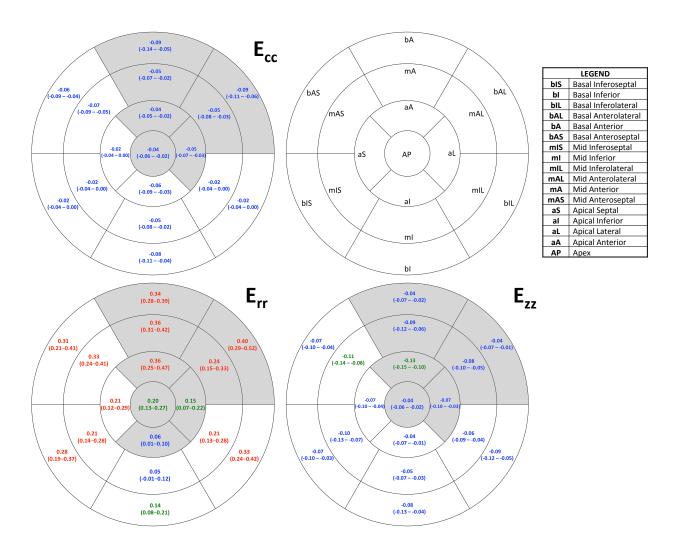
Figure 3-10. Peak strain amplitudes with 95% CI at the segment level. Segments with generally adequate image quality are shown in white; segments with lower image quality are shown in gray. Red denotes absolute mean strain amplitude > 0.20; Green, > 0.10, and Blue ≤ 0.10

3.5 Future extensions of the study

We chose to focus on the feasibility of the technique and establishment of normal value ranges, rather than on measurement of absolute error values, due to the lack of ground truth data for the human LV. While sonomicrometry is an accepted surrogate for ground truth in animal studies, such a technique is not viable in humans. Other 2D and 3D ultrasound-based methods of strain estimation have been extensively described [101]-[104], and there are several recent reports of typical values in healthy individuals [95], [97], [105]. Although the variability among different ultrasound systems is well-documented [106], the OF-based global peak strains reported in Table 3-3 closely match the values found in the aforementioned studies. Specifically, our estimates fall well within the range of variation measured by GE (Horten, Norway) and TomTec software (TomTec Imaging Systems GMbH Unterschlessheim, Germany), whereas values reported by Toshiba (Tokyo, Japan) software appear to consistently show greater circumferential and reduced radial peak strain when compared to GE, TomTec and our method. (Yuda et al. reported the following 3D strain values using an Artida scanner with a PST-25SBT probe (Toshiba Medical Systems): -17.0 ± 1.7% for E_{zz}, -39.5 ± 3.8% for E_{cc}, and 39.6 ± 12.7% for E_{rr} [105].) Only one study reported comprehensive results at the segment level [104]; however, because a Toshiba machine was used, their reported values do not appear to correlate well with the temporal curves we reported in Figure 3-8 (notably, the range of values they report does closely match the aforementioned study by Yuda et al.). A substantial advantage of the OF method described herein is that, unlike commercial software, the image processing pipeline does not function as a "black box." Each step of the analysis has been meticulously documented and its strengths, limitations, and the meaning of the output data are

known to the end-user. Additionally, in future studies we will evaluate the feasibility of measuring transmural strain gradients – a calculation that is currently not possible with methods that consider only the endocardial surface.

Although age and sex are known to influence LV strain values [93], the small sample size in this study did not permit controlling for these variables. Thus, the results of this study should be considered as preliminary, and subject to verification in larger cohorts.

We also considered the possibility of using MRI-based strain measures as a gold standard. While 2D MRI strain measures such as CSPAMM [107], [108] are well-validated and accepted in clinical settings, comparison between 2D and 3D strain measures from different modalities is fraught with complications that can easily invalidate the result (e.g. registration of a 2D MRI slice to a 3D ultrasound volume, interpolation between differing spatial and temporal resolutions, uncertain relationship between 2D and 3D strain from different modalities). 3D cardiac strain from MRI is possible using the DENSE technique [109]. However, 3D DENSE has to date seen limited use in human studies, and cannot be considered a "gold standard" until additional evidence emerges.

3.6 Conclusions

In this study, we have demonstrated the feasibility of Optical-Flow based myocardial strain measures from RT3D ultrasound data in human subjects. We have described some optimization required to adapt the image acquisition and processing pipelines to human TTE data, and documented the range of normal values as measured by this method, at global and segmental

levels. A critical advantage of this technique over many existing approaches is the ability to estimate strain at the voxel level, thereby enabling assessment and localization of function in sub-segment regions. Our consideration of the entire LV myocardium when calculating 3D strain is a significant departure from most studies in human subjects, which examine only the subendocardial surface. Recognizing some limitations in our preliminary study and results, our ongoing work is focused on validation of these findings in a broader normal population and in disease-specific patient groups. In addition, we plan to extend the multiscale analysis to higher spatial resolutions, in order to determine whether myocardial function can be reliably quantified both at the sub-segment level, and transmurally. In the absence of "ground truth" data in the human LV, we are also evaluating the reproducibility of the method as a measure of reliability, and examining how the measures compare to existing software tools.

Chapter 4. Echocardiographic Three-Dimensional Myocardial Strain by Optical Flow: Clinical Validation in Subjects With and Without Cardiovascular Disease

4.1 Introduction

Although echocardiography is considered the first-line imaging modality in diagnostic cardiology, it has several considerable limitations, especially when the focus is on LV function. First, in most clinical scenarios, LV function is primarily assessed by visual estimation of the ejection fraction (EF), and by visual analysis of regional wall motion (RWMA). In addition to relying upon the availability of a highly-trained physician, this approach is both subjective and time-consuming. Furthermore, because the human eye cannot adequately resolve relative motion within the myocardium, EF and RWMA scoring emphasizes endocardial function, since this blood/tissue border is most clearly appreciated. Recognition of these limitations has in recent years led the research community to focus more intensely on objective and quantitative measures of LV function, such as myocardial strain. 2D strain measures, derived from tissue Doppler [73] and speckle tracking methods [74], have proven useful in detecting cardiac dysfunction and predicting cardiovascular outcomes in a wide variety of cardiac pathologies [110].

As seen in the previous chapters, with constant improvements in spatial and temporal resolution, real-time 3D (RT3D) echocardiography is also gaining popularity in the clinical setting. In the last few years, RT3D echo has become an important aid for the structural evaluation of cardiac valves, and it is gaining popularity in the functional assessment of the left and right ventricles, and of the left atrial structure and function.

In clinical practice, left ventricular (LV) systolic function is commonly assessed by echocardiographically determined ejection fraction (LVEF). The analysis of LVEF is based on

end-systolic and end-diastolic endocardial border tracings to determine the maximum relative change in LV volume during a cardiac cycle. LV wall motion analysis, which is often performed by visual estimation of the myocardial wall thickening during systole, is also a widely used method for assessing LV systolic function [111]. Recent advancements in ultrasound analysis algorithms, such as speckle-tracking echocardiography, have made possible the non-invasive assessment of myocardial deformation (strain) over different spatial axes [112]-[114]. Previous studies showed that, even in the presence of a normal LVEF, LV strain may be selectively affected in the longitudinal or circumferential direction depending on the pathophysiology and the extension of the damage to the myocardial wall [55]. Furthermore, the analysis of LV myocardial strain appears to carry prognostic value that is greater than, and additional to, the traditional LV systolic function evaluation by LVEF and wall motion analysis [55].

Even more recently, the development of real-time 3D (RT3D) echocardiography, and its diffusion beyond niche cardiac ultrasound research centers, has opened new and potentially clinically relevant applications of cardiac structure and function assessment. RT3D echo has become an important aid for the structural evaluation of cardiac valves, and it is gaining popularity in the functional assessment of the left and right ventricles, and of the left atrial structure and function. Previous studies, including several reports from our research group, have demonstrated that RT3D echo can characterize myocardial strain in 3D [18], [19], [44], [68], [69], [76], [77]. In our previous work, we described the Optical Flow (OF)-based technique for 3D strain estimation [17], and validated the method on simulated B-mode echocardiograms [18].

There is a growing collection of literature suggesting that 3D strain measures in the LV correlate with a variety of clinical and even sub-clinical disease, including hypertrophic cardiomyopathy [94], hypertension [95], and diabetes [115]. In general, such investigations are based on global strain analysis, which reduces ventricular function to a single value. Besides the study described by [103], there are few studies using non-black-box methodologies to examine regional strain patterns in the LV. In addition, most reported values arise from methodologies which track only the endocardial border, disregarding the rest of the LV myocardium. Our aims in Chapter 4, therefore, are: 1) to assess the feasibility of measuring myocardial strain using our OF pipeline in normal individuals and in patients with cardiovascular disease, and 2) to assess differences in global and segmental myocardial strain between normal subjects and patients with cardiac disease as a clinical validation of our OF algorithm. In the following sections, we describe the study population, acquisition of data in a clinical setting, and evaluation of the 3D strain measures at global and segmental levels. Lastly, we examine the feasibility of deriving 3D strain cutoff values to differentiate known risk factors for LV dysfunction.

4.2 Materials and Methods

4.2.1 Study Population

We prospectively recruited a total of 31 subjects, 19 of whom were healthy with no known history of cardiovascular disease. The inclusion and exclusion criteria for these subjects were provided in Chapter 3.

Patients were recruited from Columbia University Presbyterian Hospital's Cardiology

outpatient unit. The inclusion criteria for patients were as follows: (1) age ≥ 18 years, (2) documented history of cardiovascular disease (coronary artery disease, myocardial infarction, congestive heart failure, reduced LVEF, hypertension), and (3) previous TTE with adequate image quality. In addition, the following exclusion criteria were utilized: (1) arrhythmia causing irregular rhythm (e.g. frequent premature ventricular contractions), (2) presence of co-morbidities significantly affecting echocardiographic image quality (history of chronic obstructive pulmonary disease, asthma, or severe obstructive sleep apnea, (3) lack of previous TTE studies or documented poor image quality. The study protocol was approved by the Columbia University's Institutional Review Board (IRB). Written informed consent was obtained from all study participants.

4.2.2 Data Acquisition

All studies were conducted using a Philips iE-33 machine equipped with an X5-1 matrix array probe (Philips Medical Systems, Andover, MA, USA), and the acquisition protocol was identical to the one described in Section 3.2.2.

4.2.3 3D Strain Analysis with Optical Flow

The pipeline for strain estimation from RT3D echocardiograms was described in Chapter 3. We utilized this approach, with the same parameters (≥ 30Hz acquisition volume rate, low denoising thresholds, 7×7×7 voxel template and 9×9×9 voxel search region) to derive strain measures for all subjects in this cohort. As before, we derived pixel-wise estimates of the radial (E_{rr}), circumferential (E_{cc}), and longitudinal (E_{zz}) strain components, and calculated the peak and

TTPS values for each subject, at the global and segmental levels.

To facilitate further analysis, a physician with specific expertise in cardiac ultrasound graded every segment in the dataset with respect to visual image quality and regional wall motion. Binary visual quality scores were assigned subjectively, based on whether the segment could be interpreted in a standard TTE reading throughout the cardiac cycle. Segments that did not meet this criterion were excluded from further consideration. To grade wall motion, we used the regional wall motion score index (RWMSI) described by Duncan, et al [116]: a score of *3* corresponds to hyperkinesis, *2* to normal regional contraction, *1.25* to mild hypokinesis, *0.75* to severe hypokinesis, *0* to akinesis, and *-1* to dyskinesis. Scores were determined by reading each patient's TTE studies both from the present experiment and from previous clinical evaluations.

4.2.4   Statistical Analysis

Data are expressed as mean ± standard deviation (SD). For all statistical analyses, a two-tailed *p < 0.05* was considered significant. The Student's t-test was used to compare demographic and global echocardiographic variables. To account for variable heart cycle lengths among subjects, we applied temporal normalization, using the ES frame as a reference to align curves along the time axis.

The broad aim of this investigation was to assess the reliability of the OF technique in distinguishing normal individuals from those with a history of cardiovascular disease, and to evaluate the efficacy of analysis at the segmental level. We first evaluated whether differences in global function were significant between the two groups. Recognizing that LV dysfunction

frequently manifests in regional (as opposed to global) defects, we ascertained whether segmental peak and TTPS values were statistically different between classes of segments determined to be normal or abnormal. The Wilcoxon rank sum test (Mann-Whitney U-test) was used to compare segmental strain profiles.

We performed receiver-operating characteristic (ROC) curve analysis for each strain component to investigate the sensitivity and specificity of 3D LV strain measures in distinguishing healthy individuals from those with any history of CVD. We then performed ROC analysis with respect to several specific clinical factors known to affect LV function. The area under curve (AUC, with 95% CI), sensitivity, specificity and optimal cutoff values were calculated in each case.

4.3 Results

4.3.1 Population Demographics

The demographics of the study sample are shown in Table 4-1. Compared to the control group, the patient population was older (p <0.001), with higher BMIs (p = 0.0014) and reduced LVEF (p = 0.002). Notably, despite the prevalence of hypertension (75%) among the patient population, we did not observe differences from the control group in SBP (p = 0.36) or DBP (p = 0.96). No significant differences in heart rate were observed (p = 0.49).

Table 4-1. Demographic data of the subjects included in the study sample. *P values < 0.05 are considered statistically significant.

	All Subjects	Healthy Volunteers	Cardiac Disease Patients
N	31	19	12
Age (years)	40.1 ± 15.9	28.6 ± 5.0	58.4 ± 7.5 *
Gender (M/F)	17/14	10/9	7/5
BMI (kg/cm^2)	25.1 ± 4.8	23.1 ± 4.5	28.4 ± 3.2 *
Systolic BP (mmHg)	125.4 ± 13.7	123.4 ± 12.5	128.3 ± 15.3
Diastolic BP (mmHg)	76.5 ± 9.4	76.6 ± 9.6	76.4 ± 9.5
Heart Rate (bpm)	72 ± 10	71 ± 10	73 ± 9
Hypertension	-	-	9
Diabetes	-	-	5
Hypercholesterolemia	-	-	6
Coronary Artery Disease	-	-	6
History of Myocardial Infarct	-	-	3
History of Heart Failure	-	-	3
Atrial Fibrillation	-	-	3
Mechanical valve replacement (Aortic/ Mitral)	-	-	1/2
ICD or Pacemaker implant	-	-	3

One subject from the patient subgroup was excluded from further analysis due to very poor 2D and 3D image quality. On average, each subject had 12.1±2.8 LV segments with adequate quality in RT3D studies. The segments which most frequently exhibited suboptimal quality were: apical anterior, apex, apical lateral, mid anterior and basal anterior. After exclusion of segments that were inadequate in ≥ 80% of the study sample, subjects had 8.5±0.8 analyzable segments (161 in healthy volunteers and 95 in patients). A significant number of segments were excluded from this analysis primarily because they exhibited tissue drop-out at some point during the cardiac cycle, which could adversely affect the accuracy of OF tracking. The 80% exclusion criterion was applied due to the small sample size in this study: when examining average trends across multiple subjects, we chose to exclude segments whose average value would be based on 2-3 subjects (in contrast to generally reliable regions, whose average values

would arise from more than 10 measurements). The average frame rate was 32.7±1.1 Hz (one study at 28 Hz). It is worth noting that the overall image quality statistics in the patient cohort were almost identical to those in only the healthy cohort (Chapter 3). This suggests that the TTE screening did not produce a bias toward optimal image quality in the patient cohort.

4.3.2 Global and Segmental Strain Profiles

For global strain estimates, all adequate-quality segments in each subject were included in the calculation for each subject. Comparisons at the global level between the healthy and disease populations are presented in Table 4-2. Global longitudinal and circumferential peak strains were found to differ significantly between the two groups (E_{zz}: p = 0.026; E_{cc}: p = 0.0014; E_{rr}: p = 0.56).

Table 4-2. LV structure and function in healthy volunteers and patients, and global strain estimates by OF.

	Healthy Volunteers	Cardiac Disease Patients
3D LVEF (%)	60.9 ± 4.8	47.6 ± 12.6 *
End Diastolic Volume (ml)	107.0 ± 18.4	115.9 ±35.6
End Systolic Volume (ml)	42.2 ±10.0	64.3 ± 6 *
Number cases with EF < 50%	-	5
Number cases with EF < 35%	-	1
E_{cc} (%)	-19.4 ± 6.6	-11.8 ± 3.1 *
E_{rr} (%)	59.4 ± 23.3	54.9 ± 13.2
E_{zz} (%)	-19.8 ± 6.6	-14.9 ± 2.5 *
TTPS$_{cc}$ (msec)	414.7 ± 210.9	353.4 ± 79.6
TTPS$_{rr}$ (msec)	316.9 ± 80.4	297.4 ± 82.0
TTPS$_{zz}$ (msec)	387.7 ± 181.2	366.2 ± 77.5

The results of analysis at the segment level are shown in Figure 4-1 and Figure 4-2, as temporal strain profiles averaged across multiple subjects, with error bars representing the 95% confidence interval (CI). To avoid repetition, we refer the reader to Figure 3-8 for segment-level plots of the average strain profiles in the healthy cohort.

In Figure 4-1 we show segmental myocardial strain in the patient group. Compared to the healthy subgroup, the E_{rr} profiles of the disease subgroup tended to have decreased amplitudes, and wider CIs. In terms of peak strain timing, the TTPS in patients tended to occur later in the cardiac cycle, and was more variable across subjects (as reflected in the wider temporal CIs). The E_{zz} behaved similarly in terms of strain amplitude; notably, the basal inferoseptal and mid inferolateral segments were most affected, with values hovering near zero throughout the cardiac cycle. In general, the E_{cc} profiles in patients showed very large variability across subjects compared to E_{rr}/E_{zz} in patients, and as compared to the healthy subgroup. Notably, several segments (e.g. basal inferior, mid inferior) showed a sustained reversal in strain sign, suggestive of circumferential lengthening. For additional emphasis of the differences between the control and healthy populations, we present the three strains in all adequate segments components side-by-side in Figure 4-2. The relative coherence and greater amplitudes observed in the control population relative to individuals with CVD are quite apparent.
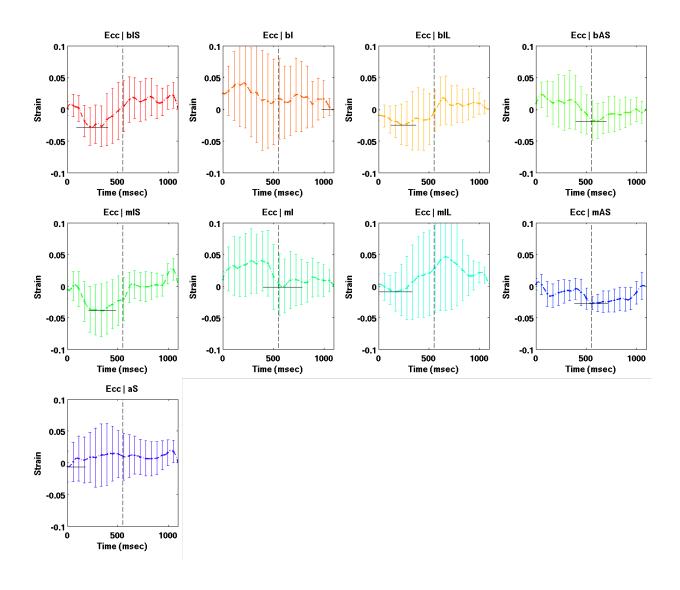
Figure 4-1a. Average circumferential strain curves for each segment in the *patient* study sample. Error bars represent the 95% CI.
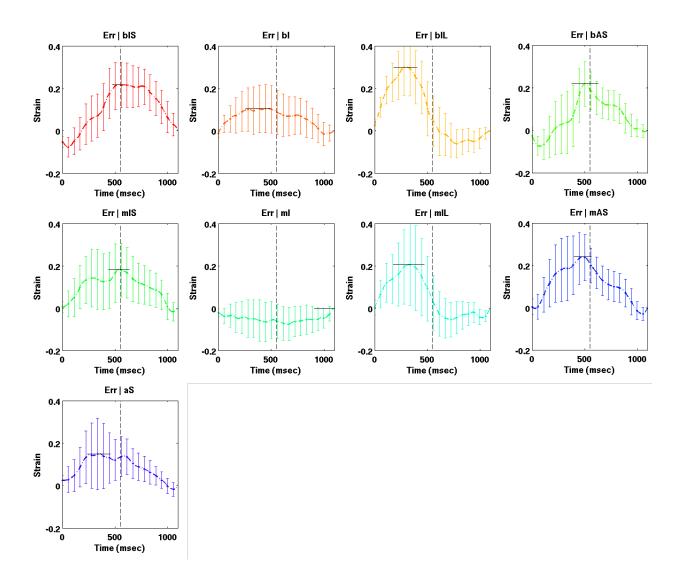
Figure 4-1b. Average radial strain curves for each segment in the *patient* study sample. Error bars represent the 95% CI.
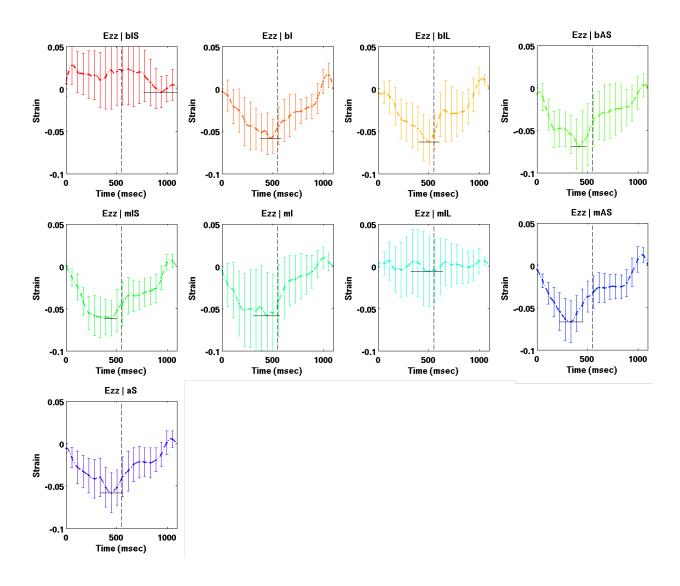
Figure 4-1c. Average longitudinal strain curves for each segment in the *patient* study sample. Error bars represent the 95% CI.
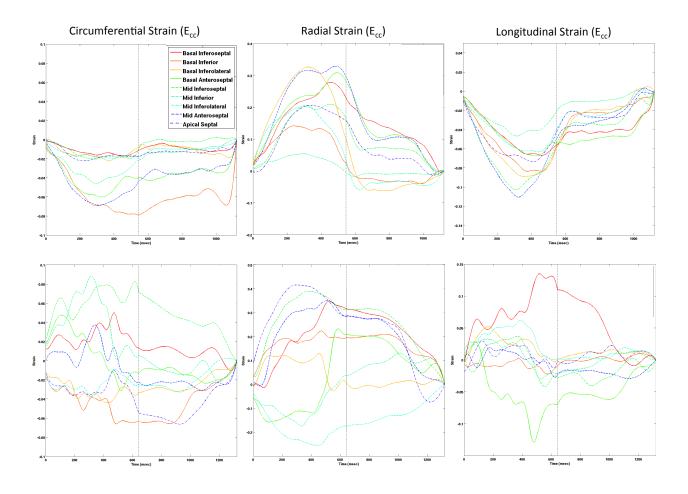
Figure 4-2. Top row: average segmental strain profiles across the control population. Bottom row: average segmental strain profiles across the patient population.

4.3.3 Strain Variation with RWMSI

To investigate the effects of increased heterogeneity in the patient population, we also calculated average profiles across all subjects after classifying segments based on function. For readability, these figures are shown in the Appendix. Figure A-1(a-c) shows the average strain profiles of severely dysfunctional segments in the patient subgroup (RWMSI < 1.25) plotted against the healthy subgroup data. For the radial component, we observed that strain

amplitudes were significantly lower (p < 0.001) in all segments except the basal inferior (p = 0.038), basal inferolateral (p = 0.863) and mid-inferolateral (p = 0.821). For longitudinal strains, significantly lower amplitudes (p < 0.001) were noted in all analyzed segments except the mid-inferior (p = 0.104). The circumferential component also demonstrated significantly reduced deformation (p < 0.001) in all segments. Similarly, in A-2(a-c), we plotted only *normal* segments from the patient subgroup (RWMSI = 2) against the corresponding healthy profiles. Although these strain profiles still differed significantly (p <0.001 in all segments, except basal inferior and apical septal for E_{rr}) from range of normal variation, the decrease in function was on average less severe than in the case of severely dysfunctional segments (Table A-2).

Analysis of peak strain distributions among segments as a function of the RWMSI is presented in Figure 4-3. For brevity, we show only the results for peak strain here; box plots for all analyzed variables and exact significance levels are provided in the appendix. Overall, there were 224 segments from the volunteer group (RWMSI = 2); in the patient group, 8 segments had a RWMSI of 0, 36 segments with a RWMSI of 0.75, 29 segments with a RWMSI of 1.25, and 66 segments with a RWMSI of 2 (total of 139 segments).
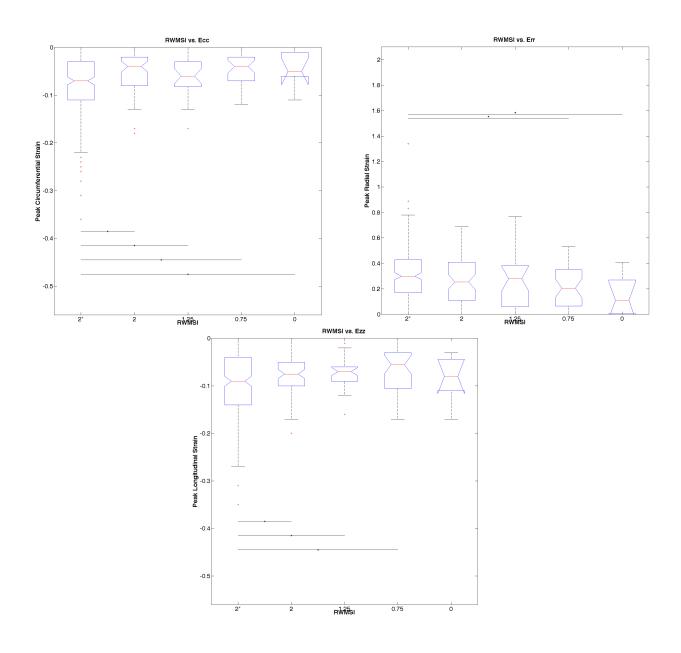
Figure 4-3. Box plot comparison of peak strain values, categorized by RWMSI in patients (0 − 2) and healthy individuals (2*). The red line represents the median value. The blue lines extend to the 25th and 75th percentiles. The dotted lines extend to the farthest samples not considered outliers. Outliers are plotted individually as red asterisks. Horizontal black lines represent significant differences at the *p < 0.05* level. No segments in the study sample demonstrated hyperkinetic (RWMSI = 3) segments.

ROC analysis revealed that global peak E_{cc} [AUC=0.87 (0.73 − 1.00)] and E_{zz} [AUC = 0.78 (0.61 − 0.97)] were best suited for distinguishing healthy individuals from those with any history of CVD. For E_{cc}, the optimal cutoff of -14% resulted in 82% sensitivity and 79% specificity. For E_{zz},

the optimal cutoff of -18% resulted in 91% sensitivity and 68% specificity. Table 4-3 summarizes the results of ROC analysis with respect to the four clinical factors most prevalent in the patient cohort.

Table 4-3. ROC curve analysis of OF-based 3D strain for detection of clinical factors known to affect LF contractility. *poor/failed test means that the AUC was not > 0.50 at the p <0.05 significance level. HTN: hypertension; HLD: hyperlipidemia; DM2: diabetes mellitus type 2; CAD: coronary artery disease.*

		HTN (N = 9)	HLD (N = 6)	DM2 (N =5)	CAD (N =6)
E_{rr}	AUC	0.6	.73 (.48-.98)	.66 (.38-.94)	.45
	OPTIMAL CUTOFF	poor test	0.43	poor test	failed test
	SENSITIVITY		.67		
	SPECIFICITY		.87		
E_{cc}	AUC	0.95 (0.85-1.0)	.91	.91 (0.74 - 1.0)	0.77 (0.53 -1.0)
	OPTIMAL CUTOFF	-14% or -13%	-14 , -13 , -12	-13% or -12%	-18% or -14%
	SENSITIVITY	1.0 or 0.89	1.0 , 83 , .83	1.0 or 0.80	1.0 or 0.83
	SPECIFICITY	0.81 or 0.90	.71 , .80 , .87	0.80 or0 .84	0.60 or 0.70
E_{zz}	AUC	0.79 (.60 - .98)	0.73 (.49 .98)	.81 (.57 - 1.0)	.80 (.57 - 1.0)
	OPTIMAL CUTOFF	-18%	-18 or -17	-15%	-17% or 16%
	SENSITIVITY	1.0	1.0 or .83	0.80	1.0 or 0.67
	SPECIFICITY	0.77	0.58 or 0.63	0.80	0.67 or 0.75

		HTN (N = 9)	HLD (N = 6)	DM2 (N =5)	CAD (N =6)
$0.49E_{cc} + 0.01E_{rr} + 0.50E_{zz}$	AUC	0.99 (0.96-1.0)	0.91 (0.75-1.0)	0.95 (0.82-1.0)	0.87 (0.68 - 1.0)
	OPTIMAL CUTOFF	-14%	-14%	-14% or -13%	-14%
	SENSITIVITY	1.0	1.0	1.0 or 1.0	1.0
	SPECIFICTY	1.0	0.875	0.88 or 0.92	0.79

4.4 Discussion

In this investigation, we evaluated the ability of our previously validated Optical Flow pipeline to measure and distinguish deformation patterns in the LVs of healthy and diseased individuals, on the basis of 3D myocardial strain estimates. In earlier studies, we performed a series of animal experiments to demonstrate that strain can be measured accurately *in-vivo*

[19], and that such measures can be used to detect ischemic and infarcted tissue [77]. Furthermore, we have described the necessary optimizations of our processing pipeline in order to extract such measures from human subjects in a clinical setting [78]. In Chapter 3, we demonstrated that the OF pipeline can be used to measure strain in healthy human subjects, and that the observed range of strain values corresponds to previous literature. The present work is our first effort to evaluate the potential clinical utility of the pipeline in distinguishing abnormal 3D strain patterns in patients with a range of CVD and LV function. To enable a comprehensive analysis of this multidimensional dataset, we applied the multi-resolution spatiotemporal framework [117] in order to examine global and segmental strain magnitudes as well as to characterize the temporal components of the deformation.

Evaluation of LV Strain: Global Approach

At the global level (Table 4-2), we observed significant differences in the peak longitudinal and circumferential strains between healthy and diseased individuals. Notably, despite the generally lower LVEF among the patient population, we did not observe a significant reduction in the global radial peak strain. This lack of differentiation based on the radial strain component may be partially explained by the greater variability in E_{rr} as compared to E_{cc} and E_{zz}. Although the average values and the range of variation we observed among healthy individuals fell within previously reported ranges [93], [97], a recent meta-analysis demonstrated that global E_{rr} measurements exhibit the most significant heterogeneity in healthy individuals [118]. Additionally, the broad inclusion criteria for this study resulted in a fairly heterogeneous patient subgroup, including subjects with hypertension but no frank LV

dysfunction (i.e. normal EF, no wall motion abnormalities). This type of population may bias global measures (especially peak function) toward normal values. Such bias is particularly accentuated if the dysfunction is highly localized in each patient: patients in whom pathology is confined to a small number of segments may exhibit reduced EF, but will not contribute significantly to the lower peak strains, since peak values in normal segments will outweigh depressed peaks in a few abnormal regions. The inherent limitations in distinguishing healthy and diseased individuals on the basis of global measures alone form the rationale for examining the data at higher spatial and temporal resolutions.

Evaluation of LV Strain: Segmental Approach

The range of variability observed in the control population was addressed in Chapter 3. Strain profiles for the patient population were first analyzed as a single group (Figure 4-1). E_{cc} profiles showed two significant deviations from the normal population. First, in 5 segments (bIS, bI, mI, mIL, aS), the average curve was positive (indicating circumferential lengthening) compared to the normal population profiles (negative, circumferential shortening); two other segments (bAS, mAS) exhibited healthy patterns, but with reduced amplitude. Second, the wider CIs in all curves corresponded to the earlier observation regarding the heterogeneity of LV function in the patient subgroup. Examination of the E_{rr} profiles also revealed generally larger CIs (both in terms of amplitude and TTPS), though overall the strain amplitudes in each segment were not significantly reduced relative to normal. An important difference from the healthy population is the lack of inter-segment correlation, for example among regions belonging to the inferoseptal and inferior walls. The longitudinal component, E_{zz}, was also

characterized by increased variability (wider CIs), somewhat decreased amplitudes, and in two segments (bIS, mIL), a reversal of sign suggesting systolic stretching. To elucidate the effect of regional functional heterogeneity in the patient subgroup, we further separated the plots by taking into account the RWMSI for each segment.

In Figure A-1, the dotted line curves represent data compiled over all segments with adequate quality and RWMSIs below 1.25. Compared to healthy distributions, we observe decreased amplitudes in all three components and in almost all segments, correlating to the severe dysfunction known to exist in these regions. With few exceptions, the systolic phase of each curve lies far outside the range of values observed in healthy individuals. By contrast, in Figure A-2 we compare strain profiles from patient segments that were graded as *normal* (RWMSI = 2) against the healthy distribution. While one might expect these segments to behave within the limits of healthy tissue, we actually observed the opposite when evaluating their deformation. Within the patient population, even segments that received normal scores tended to fall outside the normal range, though to a lesser degree than segments with known dysfunction. This suggests that functional indices such as RWMSI may not fully characterize the complex deformation behavior of tissue, since by definition they evaluate *motion* rather then *deformation*, and are based on visual assessment. Another source of error is the fact that the spatial extent of a given segment differs between visual inspection (approximate positioning) and our computer analysis (using geometric landmarks). Investigation of the curves in this regional manner and separation by functional status help to explain the lack of differentiation seen at the global scale. In particular, when the focus is on measures such as global peak strain, individuals with regional dysfunction are "masked" by LV segments with preserved function.

However, when the data are examined at the segment level, discernable changes emerge, even when the total population does not possess uniform disease. An ongoing focus of our work is to perform this type of analysis at sub-segment resolution. Sub-dividing the standard AHA segments into smaller regions leverages the high resolution offered by RT3D ultrasound, and may facilitate more precise evaluation of wall motion defects, beyond what is currently possible in the clinic.

We further illustrate this point in Figure 4-3 and Figure A-3, where we separate peak strain values and the associated TTPS at the segment level, based on RWMSI. In contrast to the global analysis, we note that all 3 strain components show statistically significant differences in peak values between control segments (denoted by 2*) and segments with known dysfunction (1.25 to 0). As in the global case, peak circumferential strain detects differences among all measured RWMSIs, including "normal" segments in patients (denoted by 2). Longitudinal strain shows similar performance. Remarkably, whereas global peak E_{rr} was not sensitive enough to separate normal and abnormal individuals, analysis at the segmental level reveals sufficient sensitivity to distinguish RWMSI of 2* from 0 and 0.75. With respect to TTPS values, we were not able to observe any significant differences among the different classes of segments. We conjecture that, contrary to the results of previous canine experiments (Chapter 3), the acquisition volume rate and image quality we were able to achieve through transthoracic imaging diminished our ability to precisely resolve the timing of the peak strains, leading to the wide standard deviations seen in the both the patient and control populations.

3D LV Strain for Clinical Screening and Diagnosis

Several studies have investigated the utility of LV strain as a diagnostic and screening tool by deriving threshold values from healthy population studies and testing the resulting sensitivity and specificity in a disease population. In 2004, Reisner et al. found that global longitudinal strain (measured in 2D) had a 92% sensitivity and 89% specificity for detection of patients with an acute myocardial infarction versus control patients with normal echocardiographic exams [113]. Becker et al. examined the ability of 2D radial strain to detect reversible myocardial dysfunction; in their study of 53 patients with LV ischemia, an optimal radial strain cutoff produced 70% sensitivity and 85% specificity in distinguishing irreversible damage at the segment level from recovered segments [119]. 2D global longitudinal strain was also examined by Afonso et al. in distinguishing patients with hypertrophic cardiomyopathy from those with other causes of LV hypertrophy [120]. Their study revealed sensitivities and specificities in the same range as the two aforementioned investigations. In the context of such studies, we sought to establish the diagnostic potential of OF-based 3D strain estimation for distinguishing patients from controls as a group, and, moreover, to do so based on clinical factors from their medical history. We chose factors such as hypertension, diabetes, hyperlipidemia and coronary artery disease because these are both highly prevalent in our patient population and known to affect LV function. Although radial strain was a poor predictor of dysfunction in the population we studied, we found that longitudinal and circumferential strains were highly sensitive (and in some cases highly specific) to dysfunction associated with

important cardiovascular risk factors (Table 4-3).

Recognizing that there is physiological interdependence between strain components, we also considered whether a combined strain metric (e.g. a weighted average of the three components) could produce a more reliable test than evaluating the components independently. Indeed, we found that a weighted average which equally emphasizes the circumferential and longitudinal components, while discounting the radial deformation, results in a universal cutoff value of -14%, with combined AUC, sensitivity, and specificity higher than what can be achieved using individual strain components. While these results are based on a small sample, if the high sensitivity in detecting dysfunction associated with the aforementioned conditions is borne out in larger populations, this technique may become a valuable screening tool.

4.5 Limitations

The small sample size and heterogeneity of the diseased subgroup are the most significant limitations in this study. In addition, we did not attempt to match controls and patients based on age, BMI, etc. Notably, despite the prevalence of hypertension among the patient population (75%), we did not observe differences from the control group in terms of SBP or DBP; this is likely due to the fact that all patients were undergoing active medical management. Thus, the results of this pilot study should be considered as preliminary, and subject to verification in larger cohorts. The wide range of pathologies in the patient subgroup does not permit us to draw any conclusions regarding the utility of this technique in the diagnosis of any specific pathology. However, it does demonstrate the method's robust nature.

4.6 Conclusions

In this study, we have demonstrated for the first time the feasibility and clinical utility of Optical Flow-based strain measures from RT3D ultrasound data in a realistic setting. Having documented the range of normal values as measured by this method in earlier work, we quantified its ability to distinguish normal and abnormal function at both global and segmental levels. Recognizing the limitations of this experiment, our ongoing work is focused on validating these findings in a broader normal population and in disease-specific patient groups. In addition, we plan to extend the multiscale analysis to higher spatial resolutions, in order to determine whether function can be reliably quantified at the sub-segment level. In the absence of "ground truth" data in the human LV, we are also evaluating the reproducibility of the method as a measure of reliability, and examining how the measures compare to existing software tools. The concept of intra-subject test-retest reliability is the subject of the following chapter.

Chapter 5. **Reliability of Three-Dimensional Myocardial Strain Measures in the Left Ventricle Using Optical Flow**

5.1 Introduction

In the preceding chapters, we described the first critical steps along the validation pathway for Optical Flow-based measures of strain in the human left ventricle. Chapter 3 presented the series of optimizations that successfully adapted the technique from invasive animal studies to noninvasive transthoracic imaging in humans. The results of the feasibility study demonstrated that three-dimensional measures of strain in the healthy human LV can be achieved, and exhibit a range of variation consistent with previously published studies. Subsequently, in Chapter 4, we addressed the question of whether this technique has sufficient discriminatory power to separate healthy individuals from those with a history of CVD. Our findings suggested that the longitudinal and circumferential components of deformation had significant sensitivity and specificity in distinguishing not only "healthy" and "diseased" states overall, but also specific pathologies that are known risk-factors for LV dysfunction.

While these results are promising, they lack the rigor of experiments in which ground-truth deformation is available. For example, the initial computational studies of OF-based strain measures relied upon models of the LV which had precisely-known motion and deformation values at every pixel [18]; it was therefore possible to quantify the method's success in terms of absolute errors in measurement. In subsequent canine studies, perfect ground-truth data could not be obtained, but a close analogue was provided in the form of sonomicrometry crystals [19]. Sonomicrometry is considered a gold standard reference for measuring regional myocardial deformation [121], [122]. These crystals were embedded directly in the mid-wall of the LV myocardium, and provided highly accurate measures of deformation in the

circumferential-longitudinal plane. Consequently, principal strains computed from sonomicrometry data and from echocardiographic imaging could be compared directly, demonstrating strong correlations and low average errors between the two methods.

In making the transition to clinical imaging in humans, we move still farther away from the possibility of utilizing a ground-truth reference for validation. A variety of ethical and practical considerations prevent the use of invasive measurements such as sonomicrometry when studying human volunteers. To address this challenge, we extensively considered the use of cardiac MRI techniques, including 2D CSPAMM and 3D DENSE (both of which are discussed in Chapter 6). The former method is well-validated, but registration to 3D ultrasound volumes is non-trivial and itself subject to errors; it is also difficult to meaningfully compare 2D deformation from MRI to 3D deformations from echocardiograms. The latter method would seem to surpass both of these limitations, but there is an extremely limited pool of evidence that 3D DENSE produces accurate estimates of myocardial deformation in humans [109]. Thus, it would be inapt to perform validation against a technique which itself has not been fully proven.

With these constraints in mind, we chose to measure the test-retest reproducibility of our technique in a sample of human subjects, comprising both healthy individuals and those with known CVD. While reproducibility does not speak directly to the absolute accuracy of the underlying measurements, it is nevertheless an important validation metric, and has been examined by multiple investigators studying myocardial strain estimation techniques [91], [106], [120], [123]-[126]. To further contextualize our results, we compared the variability of

OF-based strain measures to 2D and 3D strains derived by a well-established commercial software package. This study is the first of its kind to evaluate the reliability of a fully characterized OF-based strain estimation technique on data acquired in a routine clinical setting from prospectively recruited human subjects.

5.2 Materials and Methods

5.2.1 Study Population

For this study, we recruited a total of 22 subjects, 12 of whom were healthy, with no known history of cardiovascular disease, and 10 patients. The inclusion and exclusion criteria for all subjects in this study were identical to those detailed in Chapters 3 and 4 (see 3.2.1 and 4.2.1). Recruitment of all subjects was performed with the approval of Columbia University's Institutional Review Board (IRB), as was the remainder of the protocol as described below. Written informed consent was obtained from all study participants.

5.2.2 Data Acquisition

All studies were conducted using a Philips iE-33 machine equipped with an X5-1 matrix array probe (Philips Medical Systems, Andover, MA, USA). After 10 minutes of resting in the supine position, participants' heart rate and blood pressure were measured. The echocardiographic exam was then performed, by a licensed technician, according to the recommendations of the American Society of Echocardiography, with the subjects in left lateral decubitus position. A series of five standard 2D B-mode images were visualized and acquired: parasternal short axis at the mid-papillary level (SAX), parasternal long axis (LAX); and apical 4-chamber, 3-chamber

and 2-chamber views (A4C, A3C, and A2C respectively). For 3D assessment, a full volume acquisition of the entire LV in 3D was obtained from an apical approach, optimizing the depth and elevation width of the field-of-view (FOV) to maintain the frame rate ≥30 Hz. Four 3D B-mode volumes were acquired in four consecutive beats, using ECG triggering and real-time stitching to create the full 3D view. To achieve the best possible image quality, all views were acquired under apneic conditions. The entire procedure (beginning with blood pressure measurement) was then repeated after a minimum of 30 (and a maximum of 60) minutes had elapsed. During this time, the subjects did not eat or drink, and generally remained at rest, in order to stabilize hemodynamic variables. This time interval was chosen in order to decrease the influence of transient cardiovascular changes which could affect LV function, while still enforcing the independence of the test and re-test scenario. To minimize inter-observer variability, the same technician performed the scans for each subject.

5.2.3   3D Strain Analysis with Optical Flow

The pipeline for strain estimation from 3D echocardiograms was described in Chapters 3 and 4. For this study, all parameters and processing steps were identical to earlier investigations. As before, all datasets were processed by a single observer. The only distinction was that test/retest datasets were analyzed at least 10 days apart, in order to minimize bias. As before, the main parameters we considered were circumferential, radial, and longitudinal peak strains and the corresponding TTPS, at both global and segmental levels.

5.2.4   2D and 3D Strain Analysis with TomTec©

A single observer, who is an expert in echocardiogram interpretation and myocardial strain analysis, analyzed the 2D and 3D datasets using a commercially-available software package for 4D LV analysis (TomTec Imaging Systems, Unterschleissheim, Germany). This software automatically extracted the A4C, A2C and SA views from the RT3D full-volume data. The LV endocardial borders were initialized manually, by selecting the three standard anatomic landmarks. The 3D endocardial surface was then reconstructed automatically, and manual corrections were performed by the observer as necessary. 3D speckle-tracking analysis was then performed for all phases of the cardiac cycle. A critical distinction at this stage is that TomTec tracked *only* the endocardial surface (not the entire myocardium), and consequently provided 3D strains estimated only from the subendocardial region. The software then provided global and segmental circumferential, longitudinal, and radial strains. In addition, the resulting volume curves were used to estimate 3D LVEF. Because the software does not evaluate image quality, it was left up to the observer to judge the quality of the underlying image data and the resulting strain curves. If endocardial wall tracking in a particular segment could not be improved via manual corrections, it was excluded from the analysis.

The 2D data were analyzed with TomTec in a similar fashion, with a combination of semi-automated border delineation and automated speckle-tracking. Note that in 2D images, the entire myocardial wall is segmented (i.e. both endo- and epicardial borders), and consequently all points in the myocardium in that particular slice are considered in the strain calculation. The set of apical LAX images permitted measurement of longitudinal strain in the 17 segments of

the LV. Radial and circumferential strains were measured only at the mid level, from the SAX images.

To minimize intra-observer bias, the "test" and "retest" datasets were analyzed at least 7 days apart, with the observer blinded to the results of the previous reading.

5.2.5   Statistical Analysis

Data were expressed as mean ± standard deviation (SD). For all statistical analyses, a two-tailed t-test was used, and p-values less than 0.05 were considered significant. To account for variable heart-cycle lengths among subjects, we applied temporal normalization, using the ES frame as a reference to align curves along the time axis.

Our approach to the statistical analysis and interpretation of this data consisted of three stages. First, we established the baseline reproducibility of the experimental setup by examining the main physiological variables: HR, DBP, SBP, and LVEF. For each variable, we computed the mean and standard deviation, the test-retest variability (VAR), the between-subject variability (also known as the coefficient of variation (CV)), and the intraclass correlation coefficient (ICC). The test-retest reliability was computed as follows:

$$VAR = \frac{1}{N}\sum_{i=1}^{N}\frac{|test_i - retest_i|}{(test_i + retest_i)/2} \cdot 100\%.$$

(5.1)

In the second stage, the same measures were computed for the strain parameters derived from the Optical Flow pipeline. Lastly, we applied these statistical tests to the strain results generated by the TomTec software, which established a secondary standard of reproducibility,

for comparison with our results. We also utilized Bland-Altman plots to assess whether the level of observed function (e.g. strain amplitude) had any effect on the reproducibility of the results. Analysis was performed using commercially available software (Excel 2011, Microsoft, Redmond, WA, USA; SPSS version 22, SPSS, Inc, Chicago, IL, USA).

5.3 Results

The demographics of the study sample are shown in Table 5-1. We note that the control and CVD subjects differed significantly in terms of age and BMI, but not with respect to HR, SBP or DBP. The mean 3D LVEF in the control population was 60.9 ± 4.8; in the patient population the 3D LVEF was 47.6 ± 12.6 (p <0.05). Among the patient group, the most common pathologies included hypertension, hypercholesterolemia, and coronary artery disease.

Table 5-1. Demographic data of the subjects in the study sample. *P values < 0.05 are considered statistically significant.*

	All Subjects	Healthy Volunteers	Cardiac Disease Patients
N	22	12	10
Age (years)	41.9 ± 17.1	27.9 ± 5.9	58.7 ± 7.9 *
Gender (M/F)	13/9	6/6	7/3
BMI (kg/cm^2)	25.0 ± 5.1	22.4 ± 4.9	28.0 ± 3.5 *
Systolic BP (mmHg)	128.4 ± 14.0	125.5 ± 14.5	131.8 ± 13.3
Diastolic BP (mmHg)	75.5 ± 8.8	73.3 ± 9.3	78.1 ± 7.8
Heart Rate (bpm)	72 ± 11	72 ± 13	72 ± 9
Hypertension	-	-	8
Hypercholesterolemia	-	-	6
Coronary Artery Disease	-	-	6
Diabetes	-	-	5
History of Myocardial Infarct	-	-	3
History of Heart Failure	-	-	2
Atrial Fibrillation	-	-	2
Mechanical valve replacement (Aortic/ Mitral)	-	-	1/1
ICD or Pacemaker implant	-	-	3

In Table 5-2, we summarize the reproducibility of the basic physiological parameters

recorded at the start of each scanning session. We observed that HR and DBP demonstrated high ICCs, though there was considerable within-subject variability in the heart rate. SBP appeared to be less reproducible based on ICC, although the within-subject variability was low. Lastly, we found that 3D LVEF (measured with TomTec) showed high reproducibility.

Table 5-2. Reproducibility of basic physiological parameters in the population.

	HR	SBP	DBP	3D LVEF
$Mean_1 \pm SD_1$	71.7 ± 10.7	128.1 ± 13.3	76.9 ± 8.6	53.5 ± 11.8
$Mean_2 \pm SD_2$	67.5 ± 10.7	123.3 ± 9.3	75.4 ± 7.8	53.0 ± 9.1
Correlation	0.79	0.54	0.87	0.83
ICC (95% CI)	0.79 (0.5–0.91)	0.50 (-0.01–0.81)	0.86 (0.63–0.95)	0.81 (0.56–0.92)
VAR	78.5%	6.5%	4.9%	11.0%
CV	15.4%	9.2%	11.0%	18.8%

In Table 5-3, we measure the reliability of the peak strain calculations for each strain component. The label "Peak of Segments" refers to a peak strain value calculated by finding the maximum positive (E_{rr}) or negative (E_{cc}, E_{zz}) peak among all segments with adequate image quality. "Peak of Global Mean" refers to finding the (positive or negative) peak of the strain curve produced by first averaging the individual strain curves from all adequate segments. In general, we see that peak values exhibit poor test-retest reproducibility. The within-subject variability (VAR) is generally close to, and frequently exceeds, the across-subject variability (CV).

Table 5-3. Comparison of variability in strain measures as a function of how peak value is computed.

	E_{CC}		E_{rr}		E_{zz}	
	Peak of Segs	Peak of Global Mean	Peak of Segs	Peak of Global Mean	Peak of Segs	Peak of Global Mean
Mean$_1$ ± SD$_1$ (%)	-13.1 ± 4.45	-2.8 ± 2.4	49.4 ± 10.1	19.5 ± 9.8	-16.7 ± 4.2	-6.6 ± 2.7
Mean$_2$ ± SD$_2$ (%)	-14.4 ± 4.1	-2.9 ± 2.6	60.3 ± 17.9	21.0 ± 10.7	-16.7 ± 5.4	-5.9 ± 2.3
VAR	23.7%	103.3%	28.0%	45.3%	23.5%	45.7%
CV	31.5%	88.3%	25.1%	50.7%	29.1%	39.8%
CORR	64.1%	56.0%	30.8%	61.4%	46.0%	13.3%
ICC (95% CI)	0.617 (0.274–0.821)	0.540 (0.158–0.777)	0.418 (-0.167–0.611)	0.627 (0.288–0.826)	0.447 (0.041–0.726)	0.132 (-0.298–0.517)

We also performed a more comprehensive investigation of reproducibility at the segmental level. Two illustrative cases of segmental strain curves in the test-retest scenario are shown in Figure 5-1. In the set of circumferential strain curves, we saw that even though most segments (except the basal inferior wall) closely resemble each other in temporal progression and amplitude, there is significant variability in the absolute peak values attained. This was also true of the global average profile, in the bottom right panel. A similar situation occurs in the radial strain profiles from a different subject, though in this case the discrepancies in peak values were more pronounced, especially in the mid-inferior (mI) and apical septal (aS) segments. As a result, regardless of whether the maximum-of-segments or maximum-of-global-average calculation was used, there was a large difference between the first and second test in the peak radial strain values measured for this subject. Nevertheless, in both sets of curves, even by visual inspection, it is clear that the test-retest variability ought to be lower than what is observed when only the peak values are considered.

This insight prompted two additional sets of experiments. First, we examined whether reproducibility of peak values would be affected if it were measured at the segmental level. In

this case, each subject was characterized not by a single peak value per trial, but by a set of peak strains, measured in each segment (on average, 8-10 values per subject). The results of this inquiry are shown in Table 5-4. The even greater variability observed in these data provided further confirmation that assessment of the method's reliability on the basis of peak values alone would not be representative of the true underlying phenomenon.
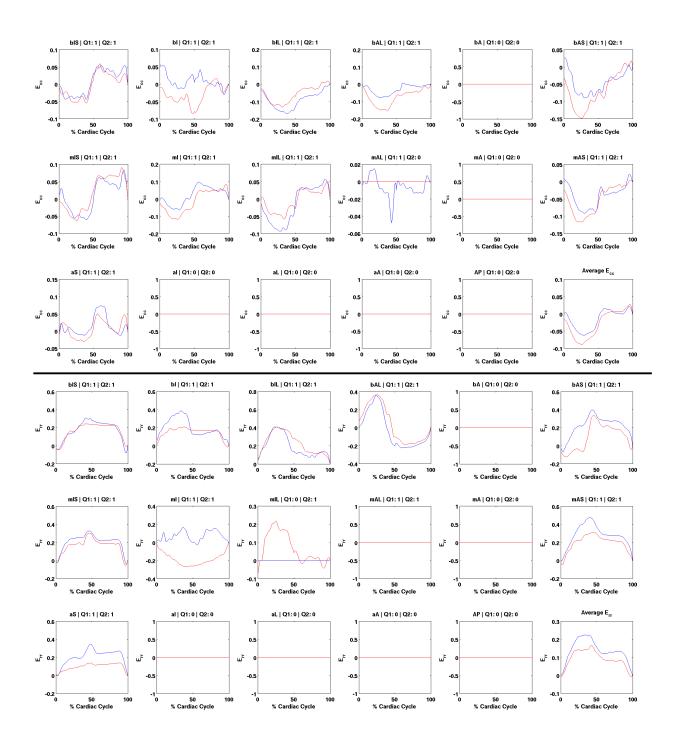
Figure 5-1. [Top] Segmental circumferential strain curves from a single subject in a test-retest (blue, red) scenario. Segments which had inadequate quality are shown as zeros and not considered. The mAL segment was adequate in the first trial but not in the second, hence one curve is constant at zero. The last panel shows the mean "global" profiles, computed by averaging all adequate segments. [Bottom] The same information is shown for radial strain curves, in a different subject. Here, the mIL segment was inadequate during trial 1, but adequate during trial 2.

Table 5-4. Reliability of peak strains measured at the segment level.

	Peak E_{cc}	Peak E_{rr}	Peak E_{zz}
MEAN$_1$ ± SD$_1$ (%)	-5.32 ± 4.79	28.3 ± 16.2	-8.69 ± 5.56
MEAN$_2$ ± SD$_2$ (%)	-6.23 ±4.97	30.0 ± 20.5	-8.53 ± 5.69
VAR	91.6%	64.1%	64.9%
CV	85.0%	62.8%	65.3%
CORRELATION	37.9%	59.6%	41.4%

The next experiment we conducted therefore focused on the complete strain curve, rather than a single characteristic value. In particular, we measured the correlation and ICC of the mean global strain profiles for each strain component in each patient. In this scenario, the output of each trial was the complete strain curve (e.g. 100 points in time), assessed in a pairwise manner across 100 pairs of points per patient. The results of this analysis are presented in Table 5-5. We note that while there are certainly cases of poor performance across all measured parameters, on average the complete strain curve is well reproducible in the radial and longitudinal directions, and adequately reproducible in the circumferential direction. In addition to examining reproducibility at the individual level, we also derived single correlation and ICC values across all subjects, by measuring the correlation and ICC after concatenation of all the average strain profiles. These findings are in the last two rows of Table 5-5. Furthermore, we utilized Bland-Altman plots to examine whether differences in measurement had any dependency upon strain amplitude (Figure 5-2).

Table 5-5. Reproducibility of mean global strain profiles for each subject in the study. ICC values ≥ 0.800 are in green; 0.800 > ICC ≥ 0.600 is orange, and ICC < 0.600 is red.

SUBJECT #	E_{rr} CORR	E_{rr} ICC (95% CI)	E_{cc} CORR	E_{cc} ICC (95% CI)	E_{zz} CORR	E_{zz} ICC (95% CI)
1	0.977	0.917 (0.879 – 0.944)	0.338	0.283 (0.093 – 0.454)	0.922	0.729 (0.622–0.809)
2	0.882	0.873 (0.817 – 0.913)	0.311	0.252 (0.059–0.427)	0.144	0.137 (-0.061–0.323)
3	0.992	0.990 (0.986 – 0.993)	0.919	0.906 (0.863–0.936)	0.976	0.973 (0.960–0.982)
4	0.869	0.834 (0.762 – 0.885)	0.692	0.421 (0.245–0.569)	0.929	0.922 (0.886–0.947)
5	0.992	0.942 (0.916 – 0.961)	0.864	0.589 (0.445–0.704)	0.990	0.989 (0.984–0.993)
6	0.970	0.967 (0.951 – 0.977)	0.962	0.918 (0.880–0.944)	0.986	0.871 (0.814–0.911)
7	0.640	0.424 (0.249 – 0.572)	0.783	0.519 (0.359–0.648)	0.924	0.695 (0.579–0.784)
8	0.978	0.978 (0.967 – 0.985)	0.949	0.926 (0.892–0.950)	0.973	0.958 (0.939–0.972)
9	0.973	0.912 (0.871 – 0.940)	0.772	0.770 (0.676–0.839)	0.886	0.883 (0.831–0.920)
10	0.992	0.935 (0.905 – 0.956)	0.810	0.735 (0.630–0.814)	0.959	0.847 (0.781–0.895)
11	0.976	0.974 (0.961 – 0.982)	0.938	0.932 (0.901–0.954)	0.943	0.904 (0.860–0.934)
12	0.876	0.804 (0.721 – 0.863)	0.888	0.840 (0.771–0.889)	0.867	0.858 (0.796–0.902)
13	0.631	0.371 (0.189 – 0.528)	0.344	0.297 (0.108–0.466)	0.918	0.884 (0.832–0.920)
14	0.076	0.074 (-0.123 – 0.266)	-0.790	-0.781 (-0.847–-0.691)	0.561	0.458 (0.288–0.600)
15	0.788	0.780 (0.690 – 0.846)	0.858	0.856 (0.793–0. 901)	0.861	0.854 (0.791–0.900)
16	0.949	0.901 (0.856 – 0.932)	0.919	0.911 (0.870–0.939)	0.958	0.853 (0.789–0.899)
17	0.965	0.913 (0.873 – 0.940)	0.753	0.753 (0.653–0.827)	0.913	0.905 (0.862–0.935)
18	0.854	0.661 (0.535 – 0.759)	0.664	0.552 (0.399–0.675)	0.736	0.722 (0.613–0.804)
19	0.941	0.836 (0.766 – 0.887)	0.634	0.627 (0.492–0.733)	0.807	0.733 (0.627–0.812)
20	0.948	0.835 (0.764 – 0.886)	0.464	0.259 (0.067–0.432)	0.612	0.582 (0.435–0.698)
21	0.915	0.899 (0.853 – 0.931)	0.581	0.580 (0.434–0.697)	0.916	0.829 (0.756–0.882)
22	0.847	0.779 (0.688 – 0.846)	0.449	0.437 (0.264 – 0.583)	0.055	0.053 (-0.144–0.246)
MEAN	0.865	0.800	0.641	0.572	0.811	0.756
Global CORR	0.759		0.516		0.582	
Global ICC		0.755		0.511		0.578
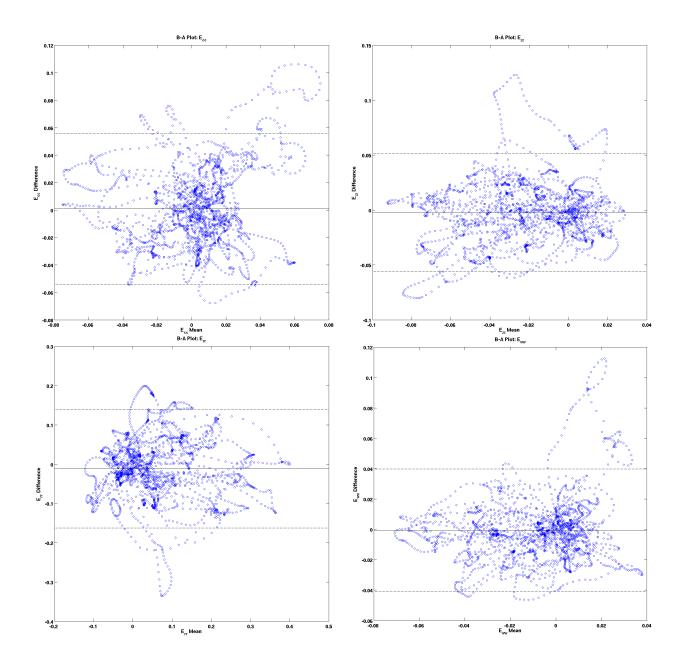
Figure 5-2. Bland-Altman plots for each strain component and for the weighted strain metric (E_{ww}), using every point from average strain curves. The solid line represents the mean difference and the dotted lines are mean ± 1.96SD.

Next, we computed the reproducibility measures of the weighted strain metric (E_{ww}) introduced in Chapter 4. This was of particular interest because although this metric also relied on peak strain values, it had demonstrated high sensitivity and specificity in distinguishing normals and controls. Paralleling the last two rows of Table 5-5, we found a global correlation

of 0.635, and a global ICC of 0.629. This indicated lower reproducibility compared to E_{rr}, but better performance than either E_{cc} or E_{zz} individually. Bland-Altman results are also shown in Figure 5-2.

Finally, we measured the reliability of the commercial TomTec software package, whose output consisted of peak strains measured from both 2D and 3D views. A summary of the findings is presented in Table 5-6. 2D radial and circumferential strains were measured only at the mid-level of the LV, in a SAX view. 2D longitudinal strains were measured in all segments, using A4C, A3C, and A2C LAX views to achieve full coverage. 3D strains results represent peak global values, measured only at the subendocardium (reproducibility analysis of the full strain curves at the segment level was not performed). Note that these results do not include 4 control subjects, whose data has not yet been processed.

Table 5-6. Reproducibility of global 2D and 3D peak strain measurements from the TomTec commercial software package.

	MEAN ± SD1 (%)	MEAN ± SD2 (%)	VAR	CV	CORRELATION	ICC (95% CI)
2D E_{cc}	-20.6 ± 5.9	-21.7 ± 5.6	11.3%	27.4%	86.0%	0.859 (0.663 − 0.945)
2D E_{rr}	36.4 ± 24.8	38.2 ± 20.0	55.1%	60.3%	57.3%	0.560 (0.140 − 0.809)
2D E_{zz}	-16.7 ± 5.1	-18.2 ± 5.9	19.6%	31.5%	81.3%	0.806 (0.553 − 0.923)
2D E_{zz}	-16.2 ± 6.6	-16.8 ± 7.0	21.2%	41.3%	83.3%	0.801 (0.519 − 0.926)
2D E_{zz}	-16.1 ± 6.7	-16.7 ± 6.1	26.6%	38.8%	67.1%	0.631 (0.231 − 0.849)
3D E_{cc}	-25.1 ± 5.6	-27.4 ± 6.7	18.2%	23.4%	61.3%	0.604 (0.204 − 0.831)
3D E_{zz}	-17.1 ± 6.8	-17.8 ± 4.5	23.3%	32.6%	70.4%	0.651 (0.277 − 0.853)
3D E_{rr}	37.14 ± 10.32	35.99 ± 7.18	15.6%	23.9%	71.5%	0.670 (0.309 − 0.862)

5.4 Discussion

Our goal in this study was to validate Optical Flow-based estimates of 3D strain from transthoracic echocardiograms of the left ventricle acquired in a clinical setting. Owing to the lack of ground-truth data, we chose instead to examine the test-retest reproducibility of these measures, both in healthy individuals and in patients with CVD and LV dysfunction. To minimize confounding factors such as inter-observer variability and intra-observer bias, we used single observers during acquisition and analysis, and chose 7-10 day time intervals between analyses of repeated studies. utilized

To establish the baseline reproducibility of the experimental setup, we measured the variability of subjects' heart rate and blood pressure, as well as the 3D LV ejection fraction. We observed that while HR, DBP and LVEF were reproducible (in terms of ICC) between the first and second trials, the reproducibility of SBP was lower than expected. Additionally, there was considerable within-subject heart rate variability, and the difference in HR between trials was statistically significant ($p=0.011$). This may be explained by the fact that although the first trial was conducted after 10 minutes of rest, the second trial was generally preceded by at least 30 minutes of sedentary activity. While subjects were free to move about between acquisitions, many chose to remain sitting or lying down, which would account for the moderate decreases in HR and SBP in particular. The decrease in HR should be considered when measuring strain reproducibility [127]. However, the absence of statistically significant differences in the other physiological parameters suggests that the experimental acquisition setup should not detract significantly from measures of reproducibility.

In extending the validation procedure from Chapters 3 and 4, our first goal was to determine whether the peak strain values obtained in those experiments were reliable, especially given the promising results of the ROC analysis. We observed that while the mean values in both trials were very close, peak values displayed significant within-subject variability, and poor reproducibility as measured by the ICC. This finding was true regardless of the method by which the peak strain was calculated. To be clear, in Chapter 4, the "peak of segments" approach was used. Although our previous results on sensitivity and specificity demonstrated that peak values can have significant discriminatory power, the high levels of within-subject and between-subject variance suggest that such outcomes may be difficult to replicate within the same individual.

The nature of how the peak values were calculated, combined with the guidance of the multiscale spatiotemporal framework, inspired us to examine the variation of peaks at the segmental level. As illustrated in Figure 5-1, a partial answer was revealed in the distribution of strain profiles across LV segments. Among the circumferential strains in this example, it was clear that most curves were highly correlated in time between the test and retest acquisitions; however, this phenomenon was not observed when reliability was judged only by a single value, i.e. using only peak values as opposed to all 100 points along the curve. Among the radial strain curves, the situation is similar, but another phenomenon arises: the mid-inferior wall shows a complete reversal of deformation between the tests, and the apical septal segment shows a significant decrease in amplitude as well. While these changes would not affect the

reproducibility of the "peak of segments" estimate (assuming the values were close to begin with), there is a clear impact on the peak of the global average strain. Again, this is true despite the clear correlation of the curves in most regions of the LV. This also suggests that image heterogeneity may play a role in peak strain calculations: although the mid-inferior segment was graded as "adequate" in both trials, its proximity to at least two other segments which were "inadequate" might have justified its exclusion as well. The influence of potentially inconsistent image quality upon peak values was further confirmed by examination of peak strain reproducibility in individual segments (Table 5-4), which showed particularly poor performance. This provided additional confirmation that at least in the case of 3D strain measures derived from OF, which encompass the entire myocardium, consideration of only peak values may represent an over-compression of the available data, leading to suboptimal reliability. Lastly, we must also consider the finding from an earlier study of the OF pipeline, which demonstrated that strain amplitudes are sensitive to the amount of denoising applied in the pre-processing steps [86]. Our finding of low peak strain reproducibility may then be explained by the combination of variability in image quality of individual segments between acquisitions, and our utilization of a single denoising threshold across all datasets.

Reproducibility of LV Strains Profiles Measured by OF

Evaluation of complete strain profiles considerably expanded the set of paired values across which reproducibility could be assessed. Rather than being characterized by a single value per trial, or by a set of 8-10 peaks from each eligible segment, each subject was represented by 100 samples from the mean global strain curve. As summarized Table 5-5, while several subjects

117

showed particularly poor reproducibility (Subjects 14, 18, and 22), the typical ICC in each patient was significantly higher, particularly in the radial and longitudinal strain components. As a whole, we note that the reproducibility of complete global-average strain curves is superior to only peak values, regardless of how those peaks are derived. Furthermore, when we consider the composite weighted strain metric from Chapter 4, the reproducibility is improved beyond what either circumferential or longitudinal components can achieve individually.

Bland-Altman analysis of the globally averaged strain components also revealed several compelling patterns. For circumferential strains, the majority of outliers coincided with positive mean E_{cc} values. Upon further scrutiny, we determined that those outliers came from a single subject, who exhibited several LV segments with E_{cc} curves that switched sign between the test and retest data. Indeed, similar inspection of the "trace-like" outliers in the other Bland-Altman plots confirmed that these patterns were caused by independent instances of low test-retest reproducibility in an individual, and were not representative of a systematic bias. Thus, while we recognize the meaning and significance of the outlier cases, we believe these graphs do further confirm the overall reliability of global average strain profiles.

Reproducibility of LV Strains by the TomTec Commercial Software

Due to the typical output of most commercial software, and the general focus in existing clinical literature on peak strain amplitudes, we chose to limit reproducibility analysis of these data to only peak values, rather than the complete curves. As summarized Table 5-6, our study indicated that TomTec software produces moderately-to-strongly reproducible results, with the exception of 2D radial strain, which appeared to have very high within-subject and across-

118

subject variability. Although OF-based peak strain reproducibility levels were lower by comparison to those of commercial software (see ICC values in Table 5-3 versus Table 5-6) it must be noted that (1) the OF method of strain estimation may be subject to more heterogeneity, as it considers the entire LV myocardium, and (2) while the criteria by which we included or excluded segments from analysis were known, it is unclear whether the "black-box" TomTec software used similar criteria. As explained previously, the inclusion or exclusion of certain segments could have dramatic effects on peak strain values in particular. It is therefore possible that application of more stringent "quality control" could result in reliability that matches or exceeds this software. Lastly, we must mention that direct comparisons between strain values are not warranted in this study, owing to the vastly different methods by which the values were obtained. In future work, we may examine whether any correlations exist, but care must be taken not to compare amplitudes directly.

5.5 Limitations

The small sample size, and in particular the small proportion of subjects with severely reduced EF, was a significant limitation of this investigation. Consequently, the results presented here cannot be generalized to larger healthy populations, nor to patients with very low EF. The potentially significant variation in heart rate, which was addressed above, may also represent a limitation by its potential effect upon strain reproducibility outside the technique actually being studied. Because we did not measure the variability of the manual steps in the process (e.g. landmark selection and LV border tracing), nor the intra-observer and inter-observer reproducibility, it is possible that (1) some of the observed variability was due to the

operator, and (2) that inter-observer variability could be significant. Thus, we cannot exclude these factors from having contributed to the observed reliability metrics. Our analysis was also limited to strain amplitude, and did not consider whether the timing of deformation (e.g. TTPS) was reproducible as well. Lastly, there are still 4 control subjects who need to be analyzed, and were not included in this dataset.

5.6 Conclusions

We determined that for OF-based estimates of LV function by 3D strain analysis, peak strain values may not be an optimal metric, as they exhibit significant test-retest variability. However, the reproducibility of the average global strain profiles is adequate, and well within the limits of a commercial software package whose reliability is well-established in clinical literature. This study also revealed the potential pitfalls of focusing exclusively on single-value metrics of LV function (i.e. only peak strains), which may initially show promising results but are difficult to reproduce. This chapter represents the first study to evaluate the reproducibility of OF-based strain measures, using data acquired in a routine clinical setting from both healthy individuals and patients with LV dysfunction. The favorable statistical results at this stage warrant further investigation in a larger population of healthy individuals, as well as patients with more homogeneous pathologies. Subsequent experiments will also examine the reproducibility and accuracy of strain findings in a regional manner – for example, whether infarcted and ischemic segments can be reliably identified. In addition, we will attempt to characterize the prognostic value of such data in terms of clinically relevant outcomes.

Chapter 6. **Myocardial Strain Estimation from Three-Dimensional Displacement Encoding With Stimulated Echoes (DENSE) in Human Subjects**

6.1 Introduction

Traditionally, new echocardiographic techniques undergo a series of validation studies beginning with computational simulations and culminating in human patient trials. As we described in Chapter 3, the OF-based speckle tracking method developed in our lab has been previously validated in simulation studies, as well as in open-chest canines. These experiments were important in verifying the accuracy and precision of OF-based strain measures, especially because ground-truth data was available: in [18], the true motion fields were known from the model used to deform the simulated tissue, facilitating direct comparison and error estimation. In the first canine study [17], partial ground-truth measures of deformation were available via implantation of sonomicrometry crystals directly in the tissue being imaged. Finally, in [19], although no "true" deformation data was gathered, strain curve accuracy was evaluated based on known anatomy and the physiological effects of coronary artery occlusion.

Establishing ground-truth data in living human subjects is considerably more challenging. From a purely diagnostic perspective, a patient's known history of disease, as well as results of concomitant pathology studies, may be used to confirm whether a new technique reliably quantifies the location and extent of disease. However, for conclusive quantitative verification of 3D strain measurements, another technique to derive deformation information is necessary. The extremely invasive nature of sonomicrometry prevents its use in human subjects; we therefore explored the potential use of cardiovascular MRI (CMR) as the standard of comparison. In this chapter, we will provide a highly abridged overview of CMR techniques, and describe the development of a new image processing pipeline for a particular pulse sequence

which has shown promise in 3D cardiac strain estimation.

Myocardial Strain Estimation in MRI

CMR provides high quality anatomical imaging of the beating heart, with known spatial registration between image planes. In conventional CMR, the paucity of identifiable landmarks within the heart wall impedes assessment of non-radial components of wall motion and of intramural motion patterns. The addition of magnetization tagging to CMR provides a means of non-invasively "marking" the tissue, which can provide information on point correspondence of locations within the heart wall between different cardiac cycle phases. Tagging can be performed with techniques such as spatial modulation of magnetization (SPAMM), which uses a
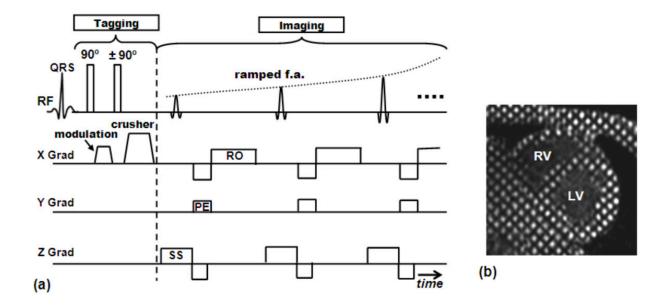
Figure 6-1. (a) The CSPAMM technique, which consists of 2 consecutive SPAMM sequences with a polarity reversal in the second RF tagging pulse. (b) Example of a 2D CSPAMM grid-tagged image. Figure from [128], used with permission. An example of 3D CSPAMM is shown in Figure 6-2.

combination of nonselective RF excitation pulses and magnetization gradients to produce a

123

regular pattern of multiple planes of altered magnetization, oriented perpendicular to the direction of the tagging gradient (Figure 6-1) [129], [130]. This technique, along with the related complementary SPAMM (CSPAMM)[131], has been extensively studied in human subjects, and is capable of reconstructing and analyzing the full 3D motion of the heart wall [132]. However, the processing of the tagged images is quite complex and relies on accurate segmentation of the heart wall. There is a very rich body of literature describing different methods of tagging analysis, ranging from active contours [133]-[135] to optical flow [136] and finite-element modeling approaches [137]. A commonly cited disadvantage among all these methods is the long processing time.

Recently, another CMR technique called displacement-encoded imaging using stimulated echoes (DENSE) has been shown to provide pixel-wise displacement measurements directly from the phase information during the MR acquisition, with relatively simpler post-processing than MR tagging, which usually needs segmentation or model fitting (Figure 6-2). This new method has been validated against MR tagging in displacement measurements and is gradually being used in a growing number of clinical applications. In [138], Ashikaga et al. utilized canine myocardial infarction models to demonstrate strong relationships between DENSE-derived strains and tissue damage as confirmed by an epicardial sock electrode array and delayed enhancement imaging. In [139], Feng et al. demonstrated the accuracy of 2D DENSE using a computational model, finding a high degree of agreement with conventional tagged MRI in both healthy volunteers and patients with a wide variety of CVD. Beyond the scope of purely investigative studies, different CMR techniques are constantly gaining clinical acceptance, with more and more clinical scenarios falling under the scope of "diagnosable by CMR" [140],

[141].These include standard anatomical scans, as well as contrast/delayed enhancement imaging and the tagging methods described above.
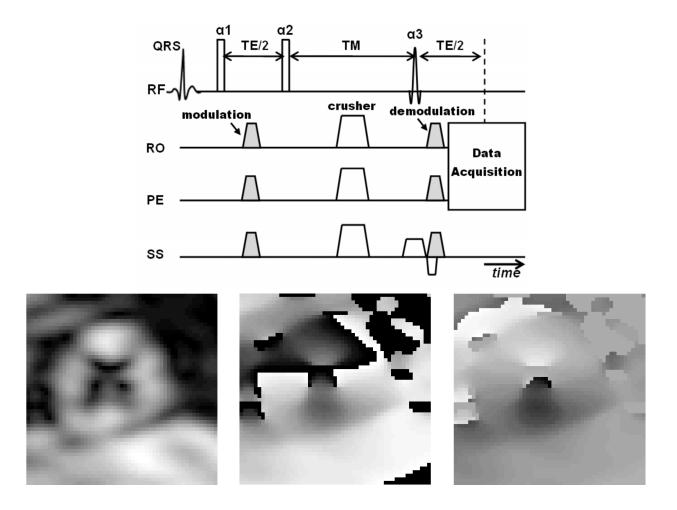
Figure 6-2. The DENSE technique. Top: the DENSE pulse sequence, which differs from CSPAMM by one additional demodulation gradient that eliminates the tag lines (from [128], used with permission. Bottom: the resulting DENSE magnitude (left) and phase (center) images, from a SAX view of the LV. Phase unwrapping produces the phase/displacement map seen in the right image.

CMR is commonly used as a reference method for validation of US techniques in human subjects. Brown et al. employed standard anatomical images obtained via Steady State Free Precession (SSFP) imaging to compare echocardiographic EF and global longitudinal strain measures to MRI-based EF [68]. Hayat et al. compared the results of 2D and 3D speckle tracking to transmural hyperenhancement on gadolinium contrast MRI, finding that globally averaged

longitudinal strain in particular correlated well with LVEF as well as tissue necrosis measured by MRI [69]. Nevertheless, a recent study by Thorstensen et al. found that when compared to late-enhancement MR images of the LV, the added diagnostic value of 3D strain could not be proven due to the limited spatial and temporal resolution of the ultrasound technique being examined [54]. Thus, although the utility and validity of US-based 3D cardiac strain measures remains an open question, in the absence of other gold-standard methods in humans (e.g. sonomicrometry), CMR-derived indices are a well-documented benchmark in the pursuit of an answer.

Building on this foundation of evidence, we sought to develop a customized DENSE acquisition and analysis pipeline to estimate 3D LV displacement (and, eventually, strain) from MRI data. Given the lack of ground-truth data in humans, our intention is to use this information together with a multiscale spatiotemporal framework to compare the results of OF-based strains against an alternative modality.

6.2 Materials and Methods

6.2.1 Data Acquisition

We executed our cardiac MRI protocol on a Philips 1.5T Achieva magnet, acquiring three distinct image series. Following the survey and cardiac localization sequences, we performed two 3D CSPAMM acquisitions. In both cases, we used a narrow FOV (108×108 mm^2) around the LV with an in-plane resolution of 0.96 mm, and a slice thickness of 7.71 mm, with 14 slices covering the entire chamber. The acquisition was performed with 7 mm and 5 mm tag spacing.

Next, we acquired DENSE data using similar parameters; the only notable distinction is a doubling of the FOV to 216×216 mm^2, which decreases the in-plane pixel resolution to 1.92 mm. These parameters correspond closely to those in published studies [142], [143]. The CSPAMM and DENSE pulse sequences are designed by Gyrotools (Gyrotools LLC, Zürich, Switzerland).

SAX view (*'x' motion*) **A4C view (*'z' motion*)** **A2C view (*'y' motion*)** **3D Cartesian orientation**
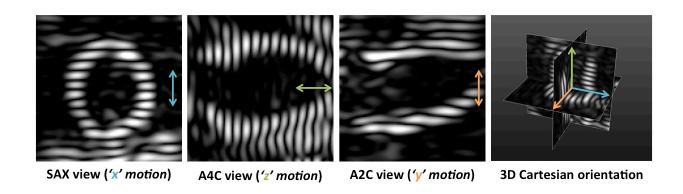
Figure 6-3. CSPAMM encodes 3D motion by acquiring the entire LV in three orthogonal slice orientations, with one motion component per acquisition. Our sequence utilizes one SAX and two LAX views, with motion encoding orthogonal to the tag line orientation. The DENSE acquisition is performed the same way (see Figure 6-2), but a demodulation step before readout eliminates the tag lines, which are illustrative here.

In all cases, we recorded 24 frames per cardiac cycle, thereby achieving a frame rate similar to 3D echocardiography. As a result, the DENSE data consists of 24 volumes of size 112×112×14 pixels. For both CSPAMM and DENSE, motion was encoded along three orthogonal directions independently: the "*x*" component is encoded in a short axis (SAX) view, while the "*y*" and "*z*" components are encoded using 4-chamber (A4C) and 2-chamber (A2C) long axis (LAX) views, respectively. An example of LV imaging using CSPAMM is shown in Figure 6-3. The DENSE pulse sequence is distinguished from CSPAMM by application of one additional gradient, which demodulates the image, effectively removing the "tag lines" seen in CSPAMM while preserving

motion information in the phase component.

Lastly, we acquire a series of short-axis oriented BTFE images using the same FOV as the DENSE data. The BTFE images have an in-plane resolution of 1.22 mm, slice spacing of 5 mm, and are acquired over 25 cardiac phases. While the CSPAMM and DENSE data are functional imaging sequences used to estimate the 3D displacement fields, the BTFE sequence is far better adapted for visualizing anatomy, and is therefore used to segment the myocardial borders.

6.2.2   DENSE Analysis Pipeline

The DENSE analysis pipeline we have developed is shown in Figure 6-4. The first step, segmentation of the LV from the 3D BTFE short-axis image stack, is performed in a semi-automated fashion, with limited user input. The BTFE images first undergo de-noising using anisotropic diffusion with parameters adapted to MRI. The user is then asked to initialize an endocardial contour on a single mid-LV slice. This is limited to a single click-and-drag action, which generates an ellipsoid close to the endocardium. This contour is then used to initialize a level-set method known as Distance Regularized Level Set Evolution (DRLSE), described by Chunming et al. [144]. The DRLSE method is notable for its avoidance of reinitialization (a common technique required for numerical stability but computationally expensive), which permits stable, fast evolution of the level set. This particular formulation uses the edge-based active contour model to evolve the level set function, making it well-suited to segmenting the high contrast region between the blood pool and endocardium.
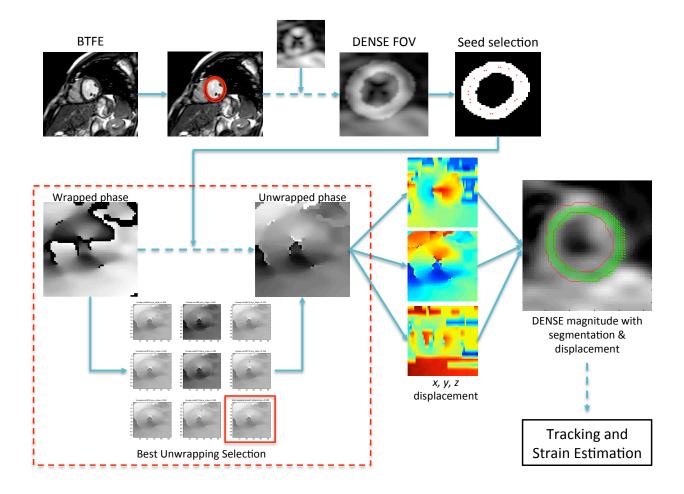
Figure 6-4. The DENSE analysis pipeline. Top row: segmentation of the anatomy from the SAX BTFE image series, registration of the binary mask to the DENSE FOV and seed point selection. Bottom row: selection of best unwrapped phase map, repeated for *x*, *y*, and *z* motion encoding directions, and generation of displacement vectors inside the myocardial contours.

Once the contour has stabilized at the endocardial border, the "final result" for that slice is morphologically eroded, and used to initialize the subsequent slice. This process is repeated for all slices and time-points in the BTFE series. At each step, the user is permitted to correct any inaccuracies in the contour, in order to limit error propagation. Once the endocardial border has been identified, the epicardial border is automatically segmented by proportional dilation of the endocardial mask. The magnitude of the dilation is calculated based on the observation

that the area of the blood pool is closely correlated with the thickness of the myocardium (Figure 6-5). By modeling this correlation as a linear relationship, we are able to accurately segment the epicardial border, without relying on edge-based methods, which tend to fail in areas where tissue contrast is low (e.g., where the epicardium border is adjacent to other organs).

Next, the resulting binary mask is registered and interpolated to match the DENSE image series, using the known orientation and resolution parameters. We perform phase unwrapping utilizing the method described by Cusack and Papadakis [145], extending their original 3D implementation to 4D. The original implementation relies on a seed point with reliable phase, after which unwrapping is first performed on less noisy regions (estimated from the magnitude images), followed by more unreliable regions. At present, we unwrap the entire 4D dataset; however, in future iterations we may constrain this to a narrow ROI around the myocardium, in order to limit error propagation from unreliable regions outside the tissue. Beyond the simple magnitude-based quality mapping in Cusack's implementation, we also examined the value of a more sophisticated quality map estimation based on the method described in [146]. In our case, the seed point candidates are selected directly from the skeletonized binary mask of the myocardium. This generates a large number of unwrapped phase maps. We automatically choose the best candidate based on the number of phase artifacts or discontinuities present in phase-unwrapped data, inside the myocardial mask.
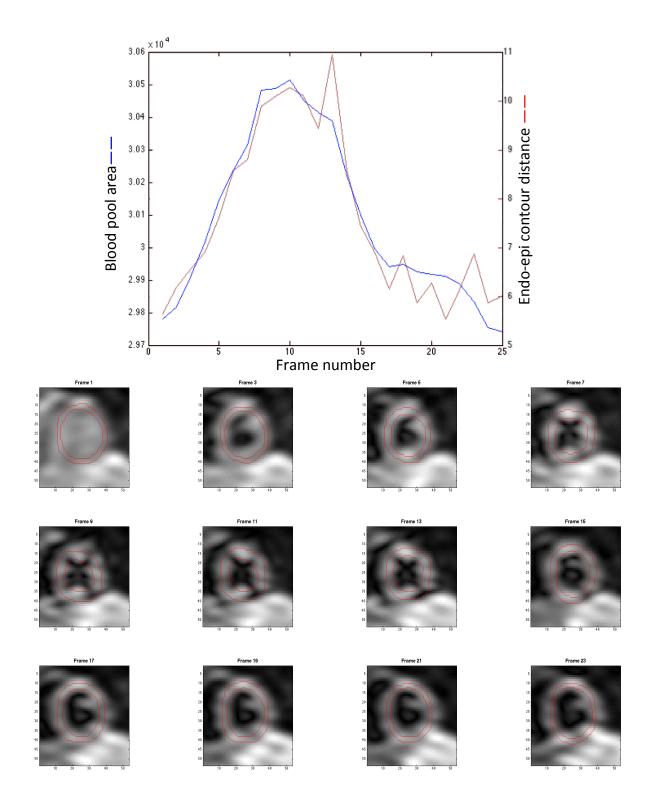
Figure 6-5 [Top] Correlation between the blood pool area (blue), and average distance between manually traced endocardial and epicardial borders (red); all units are in pixels. [Bottom] Sample segmentation result from BTFE images, overlaid on DENSE magnitude images, on 12 frames. Note that the DENSE sequence blurs the anatomy, which is why the myocardium appears to extend beyond the endo/epicardial borders delineated in BTFE images.

We thereby select the unwrapped phase map with the fewest discontinuities in the ROI, even if the background areas suffer significant errors. Lastly, we detect and correct any inter-slice $2N\pi$ discontinuities by a global offset on all phase values.

This process is repeated for each of the three encoding directions. Subsequently, the unwrapped phase values are converted directly to displacement using the relationship

$$\phi = 2\pi G_T \Delta x,$$

(6.1)

where ϕ is the unwrapped phase, γ is the gyromagnetic ratio, G_T is the encoding gradient strength, and Δx is the displacement [147]. Referring back to the DENSE pulse sequence depicted in Figure 6-2, this equation arises from the idea that the phase of a stationary spin is first set by the "modulation" gradient, and after a mixing period (TM) is rewound by the "demodulation" gradient back to zero. However, for non-stationary spins, the rewinding is incomplete, and the amount of phase remaining after demodulation is directly proportional to their displacement during the mixing period. The end result of this process is three 3D displacement maps in time, with each series encoding motion in one of the three Cartesian directions. Combined with the mask of the myocardium, this data is converted to the same format as required by the OF strain pipeline, and subsequently strain calculation is performed.

6.2.3   *Study Population*

In order to perform initial validation of the DENSE method, and to test our ability to acquire RT3D echocardiograms and MRI images with minimal time intervals between scans, we

recruited 8 healthy volunteers and 2 patients with a known history of CVD and regional wall motion abnormalities. All subjects provided written informed consent, in accordance with Columbia University's IRB. For healthy volunteers, the inclusion and exclusion criteria were identical to those cited in previous chapters. For patients, the inclusion and exclusion criteria from the earlier studies were augmented as follows: in order to ensure compatibility with MRI, we excluded all patients with an AICD or pacemaker implant, with drug eluting or bare metal stents, with mechanical valve replacements, and with any other positive MRI exclusion criteria (e.g. ferromagnetic implants, claustrophobia). The demographic data for this study sample are presented in Table 6-1. To give a sense of typical eligibility for MRI among patients with CVD, we screened 222 subjects based on medical history. Of these, 65 patients (29%) were deemed eligible based on clinical factors, and their TTEs were reviewed. 30 (14% overall) were further confirmed eligible following TTE review. The two patients in this investigation were recruited from this pool.

While we were able to obtain complete data sets from all volunteers, neither patient yielded a complete data set for our study. In the first case, the patient completed both parts of the study, but all CMR data suffered significant artifacts due to the presence of an artificial mitral valve and several drug eluting stents (following this study, the study criteria were modified to exclude such cases). In the second case, the patient was unable to undergo the CMR portion of the study due to claustrophobia. Notably, adequate quality RT3D data was successfully acquired in both cases.

Table 6-1. Demographic data of subjects undergoing combined RT3D echocardiography and CMR imaging.

	Healthy Volunteers (N = 8)	CVD Volunteers (N = 2)
Sex (M/F)	5 / 3	0 / 2
Age (yrs)	31± 4	57 ± 7
BMI (kg/m^2)	24.0 ± 3.4	29.9 ± 0.48
HR (bpm)	68 ± 5	80 ± 8
SBP (mmHg)	118.0 ± 1.8	110.5 ± 14.8
DBP (mmHg)	82.8 ± 5.5	68 ± 17.0

6.3 Results

6.3.1 Robust and Reproducible Acquisition Protocol

Figure 6-6 displays representative image data acquired from four human subjects: three volunteers and one patient. These images are indicative of the typical data quality we attain in our study, and attest to the robustness and inter-subject reproducibility at the acquisition phase. One exception is the CMR data for the patient with CVD. The presence of stents and a mechanical mitral valve produced significant artifacts, most prominently in the DENSE images; by contrast, this subject's RT3D data quality is on par with healthy volunteers.

| | V01 | V02 | V03 | P01 |
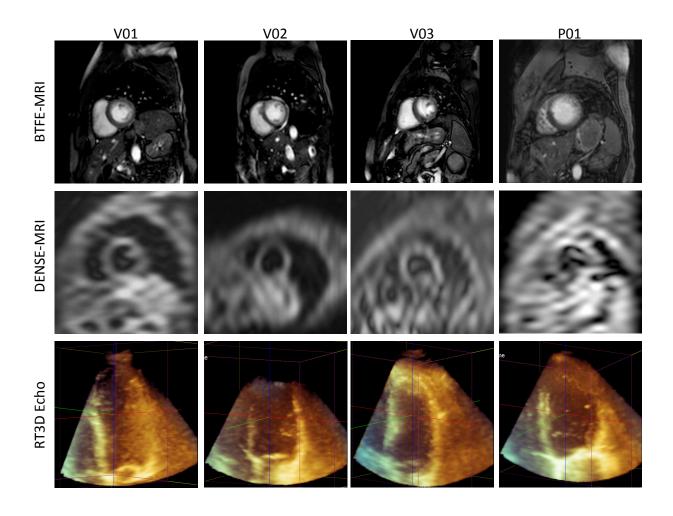
Figure 6-6. CMR and RT3D data acquired from four human subjects. The first three columns are healthy volunteers; the last column is a patient with CVD. The top row shows anatomical data acquired in a short-axis orientation at the mid-LV level. The middle row shows corresponding DENSE magnitude data. The bottom row shows an apical four-chamber view through the RT3D volumes.

6.3.2   Dense Strain Analysis

DENSE images were processed using the pipeline described above. Although segment-level quality control is not necessary to the same extent as in RT3D data, we do note significant spatial variations in quality, resulting from the tagging sequence. In particular, at the phase modulation frequency we use (corresponding to 7mm tag width), when the tag line orientation

is aligned parallel to the myocardial LAX, the tag width is close to the thickness of the underlying tissue. Signal in these regions can therefore be weak and the phase values are subject to additional noise from partial volume effects. As a result, measurements are not reliable in these areas.
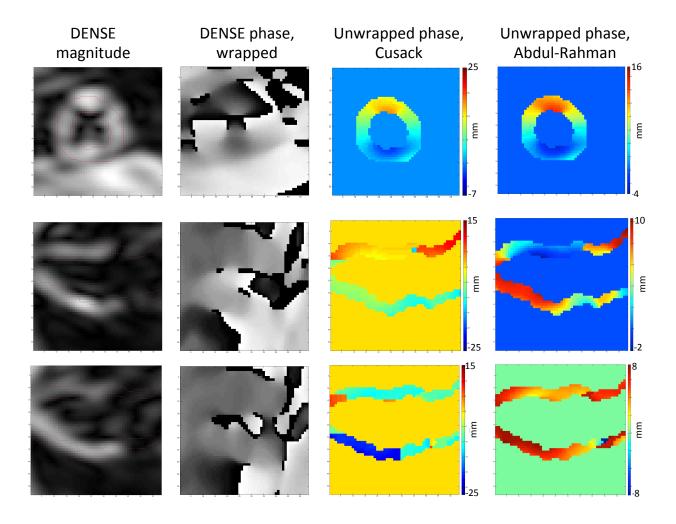
Figure 6-7. DENSE phase unwrapping. The top row shows, in order: (1) a DENSE magnitude short axis slice at end-systole with the ROI contour overlaid in red; (2) the corresponding wrapped phase image; (3) the final result of masking and unwrapping using the 4D Cusack method; (4) the final result of masking and unwrapping using Abdul-Rahman's 3D approach. The middle row shows the same case for a 4-chamber long axis slice where both phase unwrappings are successful. The bottom row shows the same LAX slice at a different time point, where the Cusack method encounters problems leading to discontinuities, while the latter method has better performance.

To mitigate these issues, we investigated several phase unwrapping approaches which have particular advantages and disadvantages. The first method, first described by Cusack [145], has been extended from its original 3D formulation into 4D, and augmented with a quality map as described in [146]. An important advantage of this approach is its reliance on a seed point, which offers the opportunity to identify one or several regions of reliable phase; this is accomplished by selecting points from the myocardial mask. As depicted in Figure 6-7, this approach has mixed results. In the SAX encoding direction, the phase unwrapping is spatiotemporally stable and continuous. However, phases unwrapped in the LAX views are more variable: while some regions are reliable, others show considerable errors (e.g. within-slice artifacts and temporal discontinuities). As we evaluated potential approaches to mitigating these errors, we are also explored alternative phase unwrapping algorithms, such as the 3D best-path avoiding singularity loops (3DBPASL) algorithm developed by Abdul-Rahman et al. [148], which does not require initial seed points for accurate results, but may be more challenging to adapt to 4D data.

Following phase unwrapping and conversion of phase to motion estimations, we perform linear interpolation to obtain isotropic volumes, producing 3D displacement maps as shown in Figure 6-8. In this example, the Cusack phase unwrapping method was used, so the *"x"* displacement maps appear to be cleanest, showing a continuous progression from base to apex, while the other two directions (encoded in 2-chamber and 4-chamber LAX orientations) show varying degrees of artifacts, ranging from within-slice discontinuities to sharp inter-slice and inter-frame (not shown) transitions.
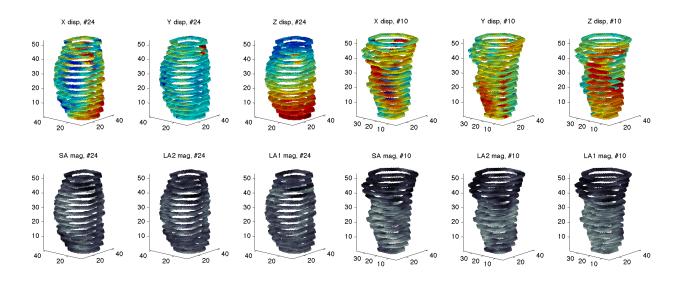
Figure 6-8. Displacement maps of the LV, generated from DENSE phase image data, overlaid onto manual tracings at each slice. End-diastole (Frame #24) is on the left and end-systole (Frame #10) is on the right. The bottom row is the corresponding magnitude image.

6.4 Discussion

The primary goal of this study was to develop an image analysis pipeline to estimate three-dimensional myocardial displacements from MRI data using the DENSE pulse sequence. Secondly, we aimed to validate the hypothesis that MRI-derived data could be acquired contemporaneously with RT3D echocardiograms in both healthy individuals and patients with CVD.

While there is a rich body of literature demonstrating the effectiveness and accuracy of MR imaging methods for cardiovascular applications, most clinically accepted methods are either two-dimensional or achieve 3D volumes by stacking multiple 2D slices. Tagging sequences such as CSPAMM – which have been successfully implemented in 3D – have limited resolution due to the physical limit on tag spacing. Since the primary purpose of this strain measurement approach is to provide a parallel estimate against which OF-based strains might be compared,

2D MRI methods would not be helpful; comparison between 2D and 3D strain measures from different modalities is fraught with complications that can easily invalidate the result (e.g., registration of a 2D MRI slice to a 3D ultrasound volume, interpolation between differing spatial and temporal resolutions, uncertain relationship between 2D and 3D strain from different modalities).

By contrast, the DENSE pulse sequence can provide motion estimates at the pixel level, in true 3D fashion by encoding each Cartesian direction independently. With spatial and temporal resolution similar to echocardiography, DENSE strain estimates can easily be incorporated into the spatiotemporal comparison framework, avoiding the critical complications cited above. A number of studies have demonstrated the successful application of 2D DENSE in both animal models and humans; 3D DENSE-based strain imaging has also been achieved in animal models [149]. To date, however, we are aware of only two publications demonstrating the feasibility of LV strain computation from 3D DENSE images in humans [109], [150]. We therefore sought to develop an in-house pipeline which would be compatible with the specific pulse sequences and MRI machines available at our institution.

With respect to the acquisition, we found that on average, RT3D echocardiograms and CMR imaging can be performed on a single subject within one hour. Although the myocardial tracing algorithm presented here has not been fully validated against expert observer tracings, qualitative analysis has demonstrated that with limited manual intervention, the results are satisfactory. A more rigorous validation routine was not applied at this stage in part because small errors in the BTFE tracing are inconsequential when overlaid onto the DENSE images,

since the latter have much lower resolution (e.g., the red contours in Figure 6-5 always appear well within the blurred myocardium seen on the DENSE magnitude images).

At the tail-end of the pipeline, the tracking and strain estimation block is complete and validated, since it is identical to the methods used in RT3D data and the spatial and temporal resolution of the DENSE displacement maps closely correlate with echocardiograms. The only remaining step where we have encountered significant challenges, therefore, is the phase unwrapping routine. Specifically, we have observed significant artifacts in the LV phase/displacement images when two popular and well-validated phase unwrapping algorithms are used. We investigated several approaches to achieving stable and accurate phase unwrapping in 3D DENSE data. Our first approach is to extend the Cusack and Papadakis method from its original 3D implementation to 4D. This ensures spatiotemporal (as opposed to exclusively spatial or temporal) continuity, while retaining the positive aspects of the technique, namely its speed, automation, and demonstrated *in-vivo* reliability [145]. Additionally, we examined the utility of alternative quality maps which are used to guide the phase unwrapping. For example, we have implemented the pseudocorrelation quality map, which, as described by Abdul-Rahman et al. [146], is one alternative when calibration data is not available. We also examined another potential quality map, calculated using the phase derivative variance [151].

Furthermore, recognizing that this method is able to unwrap 3D and 4D volumes extremely quickly (<1sec per volume), we attempted to exhaustively generate all possible phase maps resulting from seed points which are deemed reliable from the myocardial mask. The "best" result is determined by minimizing the number of artifacts (discontinuities) present in

140

the ROI as well as estimating additional parameters such as SNR and variance.

We are also attempted to utilize the 3DBPASL phase unwrapping algorithm, which has been shown, at least in phantom studies, to outperform older techniques such as Cusack [148]. Based on the results presented in Figure 6-7, we believe this method may be sufficiently robust given our typical data quality. None of these methods succeeded in eliminating all discontinuity artifacts within the myocardium ROI and ensuring perfect spatiotemporal continuity of the phase.

In addition to exploring techniques which directly generate accurate phase values, we could also investigate the option of post-processing unwrapped phase maps to detect and eliminate artifacts. For example, in their original implementation, Cusack and Papadakis described both a morphological operator step (image dilation followed by value adjustment based on masked pixels), and a Gaussian smoothing filter step – both of which were intended to "guard against loss of signal within the [wrapped phase] image" [145]. It should be noted that at no point were the displacement results we present subjected to smoothing or any additional correction. We are therefore confident that combining a more refined phase unwrapping technique with a judicious post-processing step will yield reliable phase (displacement) maps. These maps could then be used to directly track material points for a complete heart cycle, yielding the motion maps necessary for our strain estimation block.

6.5 Limitations

From a practical standpoint, the eligibility of CVD patients for MRI studies is a major hurdle.

The presence of a pacemaker or coronary stent may respectively disqualify a potential subject from MRI, or create strong artifacts in the images. Both of these interventions are very common among the types of patients we wished to examine. The need for ECG-gating and apneic conditions over extended periods are also complicating factors for many patients in advanced stages of CVD. While free-breathing DENSE sequences have been described [150], the pulse sequence we are using does not incorporate dynamic tracking of the diaphragm – a necessary feature for free-breathing scans. Regarding ECG-gating, we have observed that RT3D echocardiography is more tolerant of mild arrhythmias since only 4 consecutive rhythmic beats are required to obtain an image. The DENSE sequence, on the other hand, is much less tolerant of irregular rhythms, requires many more heart cycles for a complete image, and will extend the required apneic period if arrhythmic beats are encountered during acquisition. Typically, a series of three 20-second breath-holds are necessary; however, if the heart rate is irregular, skipped beats can cause extension of the acquisition to 30 seconds or more. Although our healthy subjects have not had problems with these breath-holds, some have expressed discomfort after the study with this aspect of the scan. Thus, we expect that patients exhibiting dyspnea on exertion, orthopnea or pulmonary dysfunction concomitant with their CVD may encounter difficulties with extended breath-holds. Because such symptoms are a common and direct consequence of the cardiovascular dysfunction, it would be impractical to exclude them from the study on this basis, and would further narrow our pool of eligible candidates. This problem can be mitigated during acquisition, however, by reducing the image resolution (i.e. increasing slice thickness), which can reduce the required apneic period by a factor of 2.

Lastly, our experience has shown that even among patients who are eager research

participants, exceedingly few are willing to undergo voluntary MRI exams.

6.6 Conclusions

In this chapter, we have presented the preliminary results of our efforts to obtain high-resolution true-3D strain estimates using CMR imaging, specifically with the DENSE pulse sequence. Although the pipeline is still undergoing development and validation, we have demonstrated that key aspects of the image acquisition and analysis steps are feasible using currently available technology, in both healthy individuals and patients with significant CVD. We also recognize that, even if fully implemented, the DENSE technique would still require extensive validation before it could be used as a "gold-standard" or correlate of "ground-truth." To this end, we could explore alternative avenues of validation, including demonstration of the ranges of normal variability in the DENSE strain estimates; demonstration of correlations between RT3D/ CMR results and known clinical factors; demonstration of agreement between DENSE and other MRI-based strain estimates (e.g. tagged CMR); and collaborations with other institutions who have implemented similar imaging protocols.

Chapter 7.   Level Set-Based Tracking of the Endocardium Without a Shape Prior From 3D

Ultrasound Images

7.1 Introduction

In the description of the RT3D Optical Flow pipeline of Chapter 2, we noted that one of the two non-automated steps involved manual delineation of the LV myocardium. While this task was not conceptually challenging, it was still time-consuming, as it required an operator trained in TTE reading to outline the endocardial and epicardial borders on multiple slices and in multiple views of the 3D volume. In Chapter 5, we similarly noted that even the commercial software package required frequent manual correction of the endocardial border, making the task only semi-automated. Such tasks are representative of a critical reason why 3D echocardiography has not gained traction in routine clinical use, despite its multiple advantages over 2D imaging.

We believe that the limitations in application of RT3D imaging to clinical echocardiography arise from the sparse collection of tools available to clinicians for analyzing the large and complex datasets generated by this powerful technique. Automated tracking of the LV wall is a challenging task due to missing edge information, speckle noise, subject variability and variation in intensity distributions. In previous work, shape priors were effectively used [152], [153]. However, shape priors have two major disadvantages: they require a significant amount of training data and they may not be able to cope well with abnormal cases. Other recent work includes methods based on a Kalman filter [154], optical flow [155], and an approach combining structural and textural information [156]. Methods based on deformable models have previously been used for segmentation of the endocardium [157]. In this study, we developed a level set-based approach to track the endocardial border of the LV. The method does not use a

shape prior model, which removes the requirement of acquiring large sets of training data, and provides substantial adaptability for abnormal cases. The method is evaluated on 10 image sequences comprising both healthy and ischemic conditions.

7.2 Materials and Methods

7.2.1 Data Acquisition

The data used in this analysis was acquired from five open-chest dogs. The research protocol was approved by Columbia University's Institutional Animal Care and Use Committee. Anesthesia was induced with propofol and was maintained using inhaled isoflurane. A lateral thoracotomy was performed and the pericardium was opened and sutured to the chest wall to expose the left ventricle. Sutures were placed around the left anterior descending (LAD) and left circumflex (LCx) coronary arteries or their branches at proximal and distal sites. Each experiment consisted of serially occluding the distal and proximal LAD and LCx branches. More details on the experimental set-up are available in [158].

The apical RT3D echocardiograms were then acquired using a Philips iE33 ultrasound system (Philips Medical Systems, Andover, MA, USA) equipped with an X3-1 probe. A single cardiac cycle consisted of 10- 12 frames. Images were acquired from an apical view, at baseline and 2 minutes after occlusion. To facilitate stable imaging of the region of interest (LV), a silicone gel standoff (Aquaflex, Parker Laboratories, Fairfield, NJ, USA) was placed between the ultrasound probe and the apex of the heart. At the conclusion of the experiment, all dogs were euthanized by injection of pentobarbital sodium and phenytoin.

7.2.2 Tracking Method Overview

The tracking method finds strong edges along the boundary of the previous frame, computes the new deformation at these locations, and then extends the deformation. Each tracking step includes five stages: 1) preprocessing of input image, 2) level set function initialization, 3) edge strength estimation, 4) front propagation, and 5) computation of full deformation. The stages are represented in Figure 7-1. As input, each step i requires the tracking result from the previous step T_{i-1}, the probability volume from previous step P_{i-1}, and the new raw image volume I_i. For the first tracking step, $T_{i-1} = T_0$ is the manual delineation, and P_0 is the preprocessing result (see 7.2.3) for image I_0.
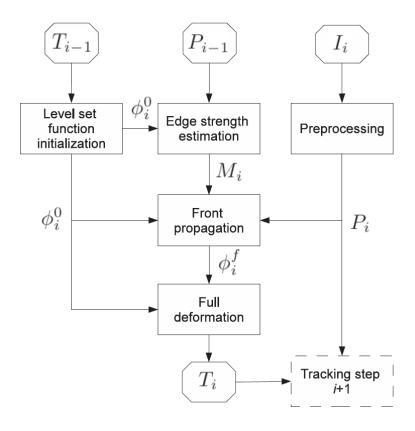
Figure 7-1. Stages of the tracking method for step i.

7.2.3 Preprocessing

In the following, $x \in \Omega$ defines an image point within the image domain . Also, let μ_0 and σ_0^2 represent respective mean intensity and variance of image points inside the initial manually delineated boundary T_0.

At each tracking step i, the new image volume I_i is first filtered $I_i' = G_{\sigma^2}(I_i)$ by a Gaussian kernel G with variance $\sigma^2 = 1.5$ (see Figure **7-2b**). The probability volume P_i is then obtained using the sigmoidal function

$$P_i(x) = \frac{1}{1 + e^{-\alpha(I_i'(x) - \beta)}} \tag{7.1}$$

where $\alpha = \omega_\alpha \sigma_0^2$ and $\beta = \mu_0 + \omega_\beta \sigma_0^2$ with empirically chosen scalar weights $\omega_\alpha = 0.05$ and $\omega_\beta = 0.1$. An example of P_i is shown in Figure 7-2c.
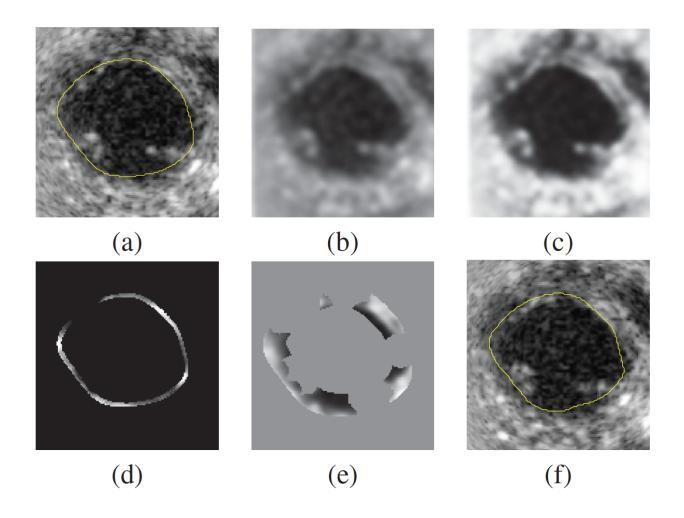
Figure 7-2. Illustration of the main stages of the method in a single tracking step: a) initial boundary T_{i-1} with the corresponding image I_{i-1}, b) filtered image I'_{i-1}, c) probability volume P_{i-1}, d) edge strength estimate E_i, e) P_i at narrow mask M_i, f) tracking result T_i overlaid on I_i.

7.2.4   Level set function initialization and edge strength estimation

The initial level set function $\phi_i^0 = \phi_i(x, t = 0)$ is obtained by computing the signed distance function with the fast marching method [159] to the boundary of T_{i-1}. The edge strength E_i in P_{i-1} is then estimated along the zero level set of ϕ_i^0: $E_i(x) = P_{i-1}\big(x + g(x)\big) - P_{i-1}\big(x - g(x)\big)$ where $g(x) = \nabla\phi_i^0(x)/\lVert\nabla\phi_i^0(x)\rVert$ with ∇ being the gradient operator. An instance of the edge strength estimate is shown in Figure 7-2d.

149

The narrow band mask M_i is the constructed for defining which parts of the image have a strong edge and can be used for propagation:

$$M_i(x) = \begin{cases} 1 & if \ x \in x_E + a\nabla\phi_i^0(x_E)/\|\nabla\phi_i^0(x_E)\| \\ 0 & otherwise \end{cases}$$

(7.2)

where $x_E = \{X|E_i(x) > 0.3\}$ and $-d_{nb} < a < d_{nb}$, d_{nb} being the narrow band width, which has to be sufficiently large to include the cardiac wall deformation in one frame. An example of a mask M_i together with the corresponding values of P_i within M_i are shown in Figure 7-2e.

7.2.1 Robust and Reproducible Acquisition Protocol

The propagation of the front is prescribed by the standard partial differential equation for the level set methods [160]:

$$\phi_t(x,t) = P_i(x)\|\nabla\phi(x,t)\| + \omega_k\kappa(x,t)\|\nabla\phi(x,t)\|$$

(7.3)

where $\kappa(x,t)$ is the mean curvature of the interface [159], and $\omega_k = -0.15$ is a weight for balancing the influence of the curvature term. The front propagation is performed only within the narrow band M_i and the output is denoted as ϕ_i^f.

For the last stage, we define a field $D_i(x_M) = \phi_i^f(x_M) - \phi_i^0(x_M)$ for $x_M = \{x|M_i(x) = 1\}$. Then this deformation is extended for other points x_O

$$D_i^f(x_O) = \mu(D_i[x_M \in N(x_O)]),$$

(7.4)

where μ denotes the mean and $N(x_O)$ defines the neighborhood of x_O as all the points on the axial slices within 1 mm of the axial slice of x_O. The final delineation T_i is given by the zero level

set of $G_{\sigma^2}(\phi_i^0 + D_i^f)$, where $\sigma^2 = 3.5$. For lower quality data, the neighborhood size should be increased to keep the interface moving at possible large gaps in M_i.

7.3 Results

7.3.1   Data and Evaluation Measures

The evaluation data consisted of 5 canine subjects with two sequences each, a baseline sequence and another obtained after ischemia induced via occlusion of the LAD or LCx. For each sequence, manual delineations by two clinicians were available, at the end-diastolic and end-systolic phases.

The tracking method was initialized with one of the manual delineations in the end diastolic phase. Tracking was performed until end systole, with the sequence including 6 or 7 image frames in total, depending on the subject. The tracking result was then evaluated against the corresponding manual delineation of the same observer as the initialization. The delineation by the other observer was used to quantify interobserver variability. The delineations were compared with the following five measures [161]: 1) volumetric overlap error [%] (OE), 2) relative absolute volume difference [%] (VD), 3) average symmetric surface distance [mm] (SD), 4) root mean square (RMS) symmetric surface distance [mm] (RD), and 5) maximum symmetric surface distance [mm] (MD).

7.3.2   Evaluation Results

The results for baseline images and ischemic images are presented Table 7-1 and Table 7-2 respectively. An example of a result is shown in Figure 7-3. The mean overlap error values,

18.23% for baseline images and 22.54% for ischemic images, show that the method achieves high accuracy; the error values of the developed tracking method are consistently smaller than the interobserver variability. For example, the mean overlap error of the method is 8 percentage points smaller for baseline images and almost 6 percentage points smaller for ischemic images than interobserver variability. The robustness of the method is evident from the lack of significant errors in the automatic tracking results, with the worst overlap error being 21.15% for baseline and 28.21% for ischemic, and worst maximum surface distance being 6.31 mm for baseline and 6.41 mm for ischemic cases. It is noted that the two observers disagreed on one delineation in particular, where the volume difference and overlap difference were close to 40%.

The mean symmetric surface distance and maximum distance values (0.98 mm and 4.80 mm for baseline, 1.29 mm and 5.39 mm for ischemic) show that the surface of the tracking result is close to the manually delineated surface. The error values and the interobserver variability are slightly higher for the ischemic images than for the baseline images.

(a)   (b)   (c)
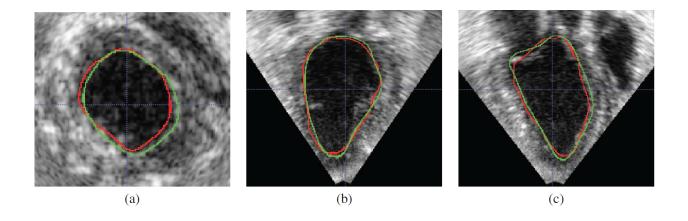
Figure 7-3. Example of baseline image tracking result in the end systolic phase after 7 frames, with automatic tracking result in red and manual reference delineation in green.

Table 7-1. Evaluation results for *baseline* images, for the automatic method compared to the interobserver variability.

		OE (%)	VD (%)	SD (mm)	RD (mm)	MD (mm)
Automatic	Mean	18.23	8.58	0.98	1.30	4.80
	SD	2.12	4.60	0.10	0.15	0.87
	Worst	21.15	16.12	1.14	1.52	6.31
	Best	15.39	4.59	0.86	1.11	4.15
Interobserver variability	Mean	26.27	18.87	1.52	1.88	6.13
	SD	9.26	14.79	0.73	0.78	1.51
	Worst	39.91	39.66	2.60	3.04	8.39
	Best	19.67	6.14	1.02	1.35	5.23

Table 7-2. Evaluation results for *ischemic* images, for the automatic method compared to the interobserver variability.

		OE (%)	VD (%)	SD (mm)	RD (mm)	MD (mm)
Automatic	Mean	22.54	13.68	1.29	1.64	5.39
	SD	4.04	8.50	0.33	0.36	0.84
	Worst	28.21	26.74	1.63	2.00	6.41
	Best	18.10	2.94	0.86	1.14	4.43
Interobserver variability	Mean	28.37	24.98	1.69	2.16	7.71
	SD	7.79	9.87	0.66	0.68	0.99
	Worst	39.97	39.70	2.76	3.27	9.48
	Best	21.13	16.16	1.20	1.56	7.18

7.4 Discussion

The accuracy of the technique was demonstrated to be higher than the range of interobserver variability, while providing a significant advantage in terms of time and objective quantification of data at much higher resolutions than afforded by segmental LV models. The average and maximum surface distance values show that the surface produced by the tracking method can be reliably used for quantification of cardiac wall motion.

153

7.5 Conclusions

In this pilot study, we developed and evaluated a novel technique to track the LV endocardial wall on RT3D ultrasound images. As hypothesized, the lack of a shape prior permitted implementation of the method without training on existing data, and facilitated acceptable performance not only in normal cases, but in ischemic situations as well. While the preliminary results demonstrated here support the notion that such an approach can function well below the interobserver variability threshold, more extensive testing and statistical analysis should be carried out in future experiments before it can be established as a certainty.

Chapter 8.   Summary and Future Work

8.1 Summary

In this dissertation, we described a series of investigations whose collective goal was to extend the Optical Flow method of strain estimation from invasive imaging studies in animals to transthoracic applications in human patients. To accomplish this task, we designed several primary and secondary experiments, whose results would confirm the feasibility, reliability and, most importantly, clinical utility of this technique.

The first study addressed two critical questions: (1) what adaptations must be applied to the OF pipeline in order to enable its use on RT3D echocardiograms acquired from humans, and (2) what is the range of variability in OF-based strain measures among healthy individuals? With respect to the former question, analysis of canine strain data from earlier studies confirmed that the acquisition frame rates afforded by currently available technology were sufficient to capture the principal dynamics of the LV's deformation. We then optimized the denoising and motion tracking blocks of the pipeline to handle transthoracic images, and demonstrated successful acquisition of data in 19 healthy individuals. To address the latter question, we quantified the range of LV strain variability at global and segmental levels. While we found the global strain variation to be quite large with respect to the mean value, analysis at the segmental level confirmed that the range and variability of strain amplitudes estimated by OF was similar to previously reported data from echocardiographic studies.

Our next investigation sought to determine whether this technique had any potential as a screening or diagnostic tool in the clinical setting. In particular, we quantified the differences in LV strain values between a group of healthy individuals and a population of patients with a

spectrum of LV dysfunction. We determined that at the global level, peak circumferential and longitudinal strains were significantly different between the two populations, whereas the radial strain was not. Moreover, analysis at the segmental level revealed that our technique detected significant differences in peak strains not only between *individuals* with and without dysfunction, but between *segments* with different wall motion score indices. ROC curve analysis demonstrated that for circumferential and longitudinal strain components, we could derive cutoff values with good sensitivity and specificity to several known risk factors for LV dysfunction. Lastly, we proposed a novel composite strain index based on a weighted sum of the three principal strains. This new measure of LV function was demonstrated to have considerably greater sensitivity and specificity as compared to any single strain component.

In the absence of ground truth strain data from the human LV, we further established the reliability of the OF technique through a reproducibility experiment. Using test-retest image data acquired from healthy volunteers and patients, we demonstrated that the average global radial strain in particular was highly reproducible, while the radial and circumferential components demonstrated low to moderate reproducibility. The composite strain index exhibited adequate reproducibility as well. Notably, in this study the observed reproducibility of the OF technique was well within the limits of reproducibility achieved by a leading commercial LV strain analysis tool. This investigation was the first to evaluate the reproducibility of an OF-based strain estimation pipeline using data acquired in a routine clinical setting from prospectively recruited human subjects.

In parallel to these three studies, we also initiated the development of another LV strain

157

estimation method, which relied on the DENSE MRI pulse sequence. The DENSE technique offers an alternative method by which 3D strains in the LV can be estimated, and could therefore become a valuable tool in the validation of the OF pipeline. Although the method to leverage 3D DENSE data requires further development and refinement, we have made significant strides in a new area of human cardiac imaging.

8.2 Future Work

As we mentioned in the discussion of each experiment, the results presented here – while promising – are based on a limited set of data. Thus, one critical next step will be to continue recruitment of study subjects for each of the three investigations. Many other compelling areas of future development exist. The following sections describe several of these possible paths, organized according to complexity and from short-term to long-term goals.

8.3 Technical Development

8.3.1   Parallelization of Optical Flow Code

In the current implementation of the OF pipeline, the greatest bottleneck in terms of processing time is the actual optical flow tracking, which requires repeated calculation of the cross-correlation coefficient over hundreds of thousands of points. As a reference, consider that a typical 3D US volume is 176×144×208 voxels; in a typical apical view acquisition, the LV mask at ED constitutes only 3-7% of the total volume, but this computes to 150,000 to 370,000 voxels – all of which must be tracked individually. Although the OF code is written to maximize computational and memory efficiency, the version of the algorithm used in this work is linear:

each voxel is tracked serially. We achieved a two-fold reduction in computation time by parallelizing the forward and backward tracking steps, using the single ED mask. More significant parallelization was not considered a priority, as the new code would require significant re-validation on previous computer simulated and animal study data to ensure consistency. However, implementation of a parallelizable computation scheme would confer significant time savings, and permit more efficient analysis in future studies.

8.3.2   Semi-Automated LV Border Tracking

The manual delineation of the LV's endocardial and epicardial borders is another source of inefficiency and may introduce some subjectivity into the strain calculation. In the current implementation of the pipeline, we used Gimias (CISTIB, University of Sheffield, UK) to create 4-5 manual tracings of the endocardium on multiple SAX views, along with 2-3 tracings in each of the 2-chamber and 4-chamber views. The process was repeated for the epicardium, after which a preliminary mask is automatically corrected with morphological operations. The end result was a single binary mask of the LV at the ED phase.

A fully automated segmentation of the LV myocardium on RT3D images is a challenging task for a number of reasons, especially because of the lack of contrast along the epicardial border. However, even a semi-automated approach which permits corrections by the end user could increase efficiency and objectivity, and enable segmentation throughout the cardiac cycle, rather than only at ED. Based on the positive results in Chapter 7, we suggest that when combined with the epicardial approximation strategy described in Chapter 6, the level set approach could be adapted for semi-automated segmentation of the LV on human TTE data.

Initialization for the LS approach could be provided by the user in a much less precise form than is required for completely manual tracing. Alternatively, McManigle et al. [162] have suggested a simpler approach, which relies on the modified Hough transform to generate a preliminary segmentation of the endo- and epicardial borders on apically acquired LV images. Naturally, the LV segmentation techniques previously developed by our research group – namely active geometric functions [163] and an implicit level set method [157] – also represent compelling alternatives for the semi-automatic segmentation approach, and have the additional benefit of automated initialization with simple geometric shapes.

8.3.3   Augmenting LV Coverage During Acquisition

As described in Chapter 3, the echocardiography protocol we implemented for RT3D images is efficient in that only a single apical acquisition is required. However, we also noted that in all studies, only about half of the 17 LV segments were considered to be of adequate quality for further analysis. Clearly, this inability to estimate strain in a large portion of the LV would not be acceptable in most screening and diagnostic scenarios. We therefore propose to explore the use of a modified image acquisition protocol, which consists of several (2-4) apical scans, each focused on a distinct subset of LV segments. If there is sufficient overlap between adjacent scans, and the subject's heart rate remains regular, a composite full-LV view could be stitched together. Since we use only 4-beat acquisitions, the total scan time would be only marginally extended, but the improvement in the total number of good-quality segments could be significant. An additional "bonus" with such an approach is a moderate increase in volume rate achieved by narrowing the FOV in the azimuth/elevation planes. Techniques for minimizing

geometric distortions (stitching artifacts) in composite 3D echocardiography have been described [164]. This feature would be particularly useful in subjects with narrow intercostal spaces, and in patients with dilated cardiomyopathy, in whom inclusion of the entire LV in a single FOV is frequently difficult, if not impossible.

8.3.4   *Improving Accuracy and Stability of Strain Estimates*

Implementation of a more efficient OF tracking algorithm, along with full-cardiac-cycle myocardium segmentation, could enable at least two refinements to the motion tracking block. First, a multiscale coarse-to-fine motion estimation scheme, similar to the one described by Mukherjee et al. [165], could be applied to improve the accuracy and efficiency of displacement estimation. The general principle behind such methods is to first estimate motion at coarse scales, then use these estimates at increasingly finer scales to guide and limit the size of the template and search windows. As explained in Chapter 3, the ability to accurately limit the dimensions of the search region carries the dual benefit of improving computational efficiency (since fewer points must be checked for potential matches to the template), and reducing random match errors (since distant candidates are not considered). Second, information regarding the position of the myocardial wall borders (obtained from the semi-automated tracking) can be combined with transmural motion estimates from OF to achieve greater accuracy, as suggested by Compas et al. [102].

We have also considered the addition of a momentum constraint to the OF search algorithm. In its current form, the OF tracking algorithm considers each 3D frame independently of the previous and subsequent frames. Thus, from the algorithm's perspective,

sudden changes in the direction and magnitude of motion between subsequent frames are perfectly acceptable, and do indeed occur in tissue regions with poor image quality (SNR). We know, however, that such fluctuations are not physiological: there is an inertial component to the moving tissue, which changes the likelihood of future motion vectors. It is therefore likely that the addition of a temporal continuity/momentum constraint to the OF tracking method would improve tracking estimates by favoring physiologically realistic displacements. This could be accomplished, for example, by applying a likelihood map to cross-correlation coefficients in a given search region, based on motion estimates from previous frames.

8.4 Clinical Development

8.4.1 Value of 3D Strain in Screening and Diagnosis

To demonstrate statistical significance across the different parameters in our validation studies, the study sample size will need to be increased. For example, a brief power analysis based on the differences in circumferential and longitudinal strain observed in our pilot study suggested that for an effect size (ES) between .98 and 1.27, with $\alpha = 0.05$, power = 0.95, and assuming equal allocation between the two groups, the projected sample size is between 40 and 60 subjects. Given that the two populations in the pilot studies were not perfectly matched (e.g., in terms of age and BMI), the ES used here is quite optimistic. For a more moderate ES between 0.70 and 0.80, the projected sample size is 84-110 subjects.

Consequently, follow-on studies should amend the existing protocols to recruit adequate numbers of healthy controls and patients who are matched with respect to age, sex, and other

known correlates of LV strain. Moreover, patient selection should target specific CVD subtypes. For example, we would expect patients with only hypertension to demonstrate significantly smaller deviations in strain patterns compared to individuals who have suffered a myocardial infarct. Moreover, identification of patients with localized and acute pathology which has not yet promoted global LV remodeling (e.g. acute infarction or ischemia confined to a few segments) could facilitate quantification of the spatial sensitivity and specificity of the OF-based strain measures.

8.4.2   Evaluating Superiority of 3D Strain Parameters

There exist at least two axes along which 3D strain measures in the LV may become superior to existing parameters derived from 2D echocardiograms. In the practical sense, if 3D strain measures are demonstrated to strongly correlate with validated 2D markers, they may become a suitable replacement if the total acquisition and analysis time is reduced. Moreover, if the automation-related technical aims are completed as described, it is likely that 3D strain measures will exhibit lower inter- and intra-observer variability compared to operator-dependent 2D methodologies. Conclusive demonstration of this type of superiority would require not only applying the OF method to RT3D data from a large patient population, but also an implementation of the pipeline for physician end-users.

The second axis is perhaps even more valuable in a clinical sense, but also more challenging. In particular, future studies should examine the prognostic value of 3D strain markers with respect to significant clinical outcomes. For example, recent investigations into the predictive value of 2D global longitudinal strain have utilized the following events/outcomes in their

analyses: cardiovascular or all-cause mortality, admission/readmission for acute HF, intra-aortic balloon pump implantation, left ventricular assist device implantation, and stroke [166]-[168]. The exact design of such a study is beyond the scope of the present work, and would depend on the type of prognostic value being evaluated (e.g. statistical incremental value, predictive incremental value, therapeutic incremental value, etc.). For an excellent discussion of the methods and challenges involved in validating new noninvasive tests for clinical use, the reader is referred to a two-part review by Hachamovitch and Di Carli [169], [170].

Bibliography

[1]   K. D. Kochanek, J. Xu, S. L. Murphy, A. M. Miniño, and H. C. Kung, "National vital statistics reports," National Vital Statistics Reports, vol. 59, no. 4, p. 1, 2011.

[2]   "The Global Burden of Disease," 2008.

[3]   T. Münzel, C. Sinning, F. Post, A. Warnholtz, and E. Schulz, "Pathophysiology, diagnosis and prognostic implications of endothelial dysfunction," Ann Med, vol. 40, no. 3, pp. 180–196, Jan. 2008.

[4]   J. He, L. G. Ogden, L. A. Bazzano, S. Vupputuri, C. Loria, and P. K. Whelton, "Risk Factors for Congestive Heart Failure in US Men and WomenNHANES I Epidemiologic Follow-up Study," Arch Intern Med, vol. 161, no. 7, pp. 996–002, Apr. 2001.

[5]   M. Heron, "National Vital Statistics Reports," Hyattsville, MD, DHHS 2014-1120, Jul. 2015.

[6]   J. N. Kirkpatrick, M. A. Vannan, J. Narula, and R. M. Lang, "Echocardiography in Heart Failure: Applications, Utility, and New Horizons," Journal of the American College of Cardiology, vol. 50, no. 5, pp. 381–396, Jul. 2007.

[7]   S. A. Hunt, W. T. Abraham, M. H. Chin, A. M. Feldman, G. S. Francis, T. G. Ganiats, M. Jessup, M. A. Konstam, D. M. Mancini, K. Michl, J. A. Oates, P. S. Rahko, M. A. Silver, L. W. Stevenson, C. W. Yancy, E. M. Antman, S. C. Smith, C. D. Adams, J. L. Anderson, D. P. Faxon, V. Fuster, J. L. Halperin, L. F. Hiratzka, A. K. Jacobs, R. Nishimura, J. P. Ornato, R. L. Page, B. Riegel, American College of Cardiology, American Heart Association Task Force on Practice Guidelines, American College of Chest Physicians, International Society for Heart and Lung Transplantation, Heart Rhythm Society, "ACC/AHA 2005 Guideline Update for the Diagnosis and Management of Chronic Heart Failure in the Adult: a report of the American College of Cardiology/American Heart Association Task Force on Practice Guidelines (Writing Committee to Update the 2001 Guidelines for the Evaluation and Management of Heart Failure): developed in collaboration with the American College of Chest Physicians and the International Society for Heart and Lung Transplantation: endorsed by the Heart Rhythm Society.," Circulation, vol. 112, no. 12. Lippincott Williams & Wilkins, pp. e154–235, 20-Sep-2005.

[8]   P. S. Douglas, M. J. Garcia, D. E. Haines, W. W. Lai, W. J. Manning, A. R. Patel, M. H. Picard, D. M. Polk, M. Ragosta, R. P. Ward, and R. B. Weiner, "ACCF/ASE/AHA/ASNC/HFSA/HRS/SCAI/SCCM/SCCT/SCMR 2011 Appropriate Use Criteria for Echocardiography," Journal of the American College of Cardiology, vol. 57, no. 9, pp. 1126–1166, 2010.

[9]   R. B. Devereux, D. R. Alonso, E. M. Lutas, G. J. Gottlieb, E. Campo, I. Sachs, and N. Reichek, "Echocardiographic assessment of left ventricular hypertrophy: Comparison to necropsy findings," The American Journal of Cardiology, vol. 57, no. 6, pp. 450–458,

Feb. 1986.

[10]   J. R. Stratton, S. M. Speck, J. H. Caldwell, G. V. Martin, M. Cerqueira, C. Maynard, K. B. Davis, J. W. Kennedy, and J. L. Ritchie, "Relation of global and regional left ventricular function to tomographic thallium-201 myocardial perfusion in patients with prior myocardial infarction," Journal of the American College of Cardiology, vol. 12, no. 1, pp. 71–77, Jul. 1988.

[11]   J. Rowland Richards, Principles of Solid Mechanics. CRC Press, 2000.

[12]   C. Russo, Z. Jin, S. Homma, T. Rundek, M. S. V. Elkind, R. L. Sacco, and M. R. Di Tullio, "Prognostic Value of Left Ventricular Global Longitudinal Strain in the Elderly: A Population-Based Prospective Cohort Study," presented at the American Heart Association Scientific Sessions, 2013, vol. 128.

[13]   C. Russo, Z. Jin, M. S. V. Elkind, T. Rundek, S. Homma, R. L. Sacco, and M. R. Di Tullio, "Prevalence and prognostic value of subclinical left ventricular systolic dysfunction by global longitudinal strain in a community-based cohort.," Eur. J. Heart Fail., vol. 16, no. 12, pp. 1301–1309, Dec. 2014.

[14]   J. Chan, L. Hanekom, C. Wong, R. Leano, G.-Y. Cho, and T. H. Marwick, "Differentiation of Subendocardial and Transmural Infarction Using Two-Dimensional Strain Rate Imaging to Assess Short-Axis and Long-Axis Myocardial Function," Journal of the American College of Cardiology, vol. 48, no. 10, pp. 2026–2033, Nov. 2006.

[15]   D. Qi, "Real-time 4D cardiac image analysis for left ventricular function," 2008.

[16]   E. D. Angelini, A. F. Laine, and J. Donis, "Quantification of right and left ventricular function with real-time three-dimensional ultrasound," 2001 Conference Proceedings of the 23rd Annual International Conference of the IEEE Engineering in Medicine and Biology Society, vol. 3, pp. 2587–2590 vol.3, 2001.

[17]   Q. Duan, S. Herz, C. Ingrassia, K. Costa, J. Holmes, A. Laine, E. Angelini, O. Gerard, and S. Homma, "Dynamic cardiac information from optical flow using four dimensional ultrasound.," Conf Proc IEEE Eng Med Biol Soc, vol. 4, pp. 4465–4468, 2005.

[18]   Q. Duan, E. Angelini, and S. Homma, "Validation of optical-flow for quantification of myocardial deformations on simulated RT3D ultrasound," Conf Proc IEEE Int Symp Biomed Imag, pp. 944–947, Apr. 2007.

[19]   Q. Duan, K. M. Parker, A. Lorsakul, E. D. Angelini, E. Hyodo, S. Homma, J. W. Holmes, and A. F. Laine, "Quantitative Validation of Optical Flow Based Myocardial Strain Measyres Using Sonomicrometry," Proc IEEE Int Symp Biomed Imaging, vol. 2009, pp. 454–457, Jun. 2009.

[20]   J. B. Partridge and R. H. Anderson, "Left ventricular anatomy: Its nomenclature, segmentation, and planes of imaging," Clinical Anatomy, vol. 22, no. 1, pp. 77–84, Jan. 2009.

[21]   S. Y. Ho, "Anatomy and myoarchitecture of the left ventricular wall in normal and in disease," European Heart Journal - Cardiovascular Imaging, vol. 10, no. 8, pp. iii3–iii7,

Dec. 2009.

[22]   M. D. Cerqueira, N. J. Weissman, V. Dilsizian, A. K. Jacobs, S. Kaul, W. K. Laskey, D. J. Pennell, J. A. Rumberger, T. Ryan, M. S. Verani, American Heart Association Writing Group on Myocardial Segmentation and Registration for Cardiac Imaging, "Standardized myocardial segmentation and nomenclature for tomographic imaging of the heart: a statement for healthcare professionals from the Cardiac Imaging Committee of the Council on Clinical Cardiology of the American Heart Association.," presented at the Circulation, 2002, vol. 105, no. 4, pp. 539–542.

[23]   "WHO | Cardiovascular diseases (CVDs)," World Health Organization, 317, Jan. 2015.

[24]   L. S. Lilly, Pathophysiology of Heart Disease. Lippincott Williams & Wilkins, 2011.

[25]   W. C. Little and R. A. O'Rourke, "Effect of regional ischemia on the left ventricular end-systolic pressure-volume relation in chronically instrumented dogs," Journal of the American College of Cardiology, vol. 5, no. 2, pp. 297–302, Feb. 1985.

[26]   W. F. Boron and E. L. Boulpaep, Medical Physiology, 2e Updated Edition. Elsevier Health Sciences, 2012.

[27]   R. G. HISS and L. E. LAMB, "Electrocardiographic findings in 122,043 individuals.," Circulation, vol. 25, pp. 947–961, Jun. 1962.

[28]   P. A. Wolf, R. D. Abbott, and W. B. Kannel, "Atrial fibrillation as an independent risk factor for stroke: the Framingham Study.," Stroke, vol. 22, no. 8, pp. 983–988, Aug. 1991.

[29]   P. Carson, I. Anand, C. O'Connor, B. Jaski, J. Steinberg, A. Lwin, J. Lindenfeld, J. Ghali, J. H. Barnet, A. M. Feldman, and M. R. Bristow, "Mode of Death in Advanced Heart Failure," Journal of the American College of Cardiology, vol. 46, no. 12, pp. 2329–2334, Dec. 2005.

[30]   Z. J. Zheng, J. B. Croft, W. H. Giles, and G. A. Mensah, "Sudden cardiac death in the United States, 1989 to 1998.," Circulation, vol. 104, no. 18, pp. 2158–2163, Oct. 2001.

[31]   W. H. Sauer, "Etiology of atrioventricular block," uptodatecom. [Online]. Available: http://www.uptodate.com/contents/etiology-of-atrioventricular-block. [Accessed: 10-Jan-2013].

[32]   T. Kasai, E. G. Depuey, and A. A. Shah, "Decreased septal wall thickening in patients with left bundle branch block.," J Nucl Cardiol, vol. 11, no. 1, pp. 32–37, Jan. 2004.

[33]   U. D. O. H. A. H. Servic, Health, United States, 2014. Hyatsville, MD: National Center for Health Statistics, 2015.

[34]   R. M. Lang, M. Bierig, R. B. Devereux, F. A. Flachskampf, E. Foster, P. A. Pellikka, M. H. Picard, M. J. Roman, J. Seward, J. Shanewise, S. Solomon, K. T. Spencer, M. S. J. Sutton, and W. Stewart, "Recommendations for chamber quantification | European Heart Journal - Cardiovascular Imaging," European Journal of Echocardiography. [Online]. Available:

http://ehjcimaging.oxfordjournals.org/cgi/doi/10.1016/j.euje.2005.12.014. [Accessed: 23-Dec-2005].

[35]   "ACC/AHA 2005 Guideline Update for the Diagnosis and Management of Chronic Heart Failure in the Adult A Report of the American College of Cardiology/American Heart Association Task Force on Practice Guidelines (Writing Committee to Update the 2001 Guidelines for the Evaluation and Management of Heart Failure): Developed in Collaboration With the American College of Chest Physicians and the International Society for Heart and Lung Transplantation: Endorsed by the Heart Rhythm Society," vol. 112, no. 12, pp. e154–e235, Sep. 2005.

[36]   M. Takeuchi, T. Nishikage, H. Nakai, M. Kokumai, S. Otani, and R. M. Lang, "The Assessment of Left Ventricular Twist in Anterior Wall Myocardial Infarction Using Two-dimensional Speckle Tracking Imaging," Journal of the American Society of Echocardiography, vol. 20, no. 1, pp. 36–44, Jan. 2007.

[37]   E. E. Konofagou, J. D'hooge, and J. Ophir, "Myocardial elastography—a feasibility study in vivo," Ultrasound in Medicine & Biology, vol. 28, no. 4, pp. 475–482, Apr. 2002.

[38]   J. Provost, W.-N. Lee, K. Fujikura, and E. E. Konofagou, "Imaging the electromechanical activity of the heart in vivo," PNAS, vol. 108, no. 21, pp. 8565–8570, May 2011.

[39]   W. N. McDicken, G. R. Sutherland, C. M. Moran, and L. N. Gordon, "Colour doppler velocity imaging of the myocardium," Ultrasound in Medicine & Biology, vol. 18, no. 6, pp. 651–654, Jan. 1992.

[40]   A. D. Fleming, X. Xia, W. N. McDicken, G. R. Sutherland, and L. Fenn, "Myocardial velocity gradients detected by Doppler imaging," Br J Radiol, vol. 67, no. 799, pp. 679–688, Jul. 1994.

[41]   K. Dohi, M. S. Suffoletto, D. Schwartzman, L. Ganz, M. R. Pinsky, and J. Gorcsan III, "Utility of Echocardiographic Radial Strain Imaging to Quantify Left Ventricular Dyssynchrony and Predict Acute Response to Cardiac Resynchronization Therapy," The American Journal of Cardiology, vol. 96, no. 1, pp. 112–116, Jul. 2005.

[42]   T. P. Abraham, V. L. Dimaano, and H.-Y. Liang, "Role of tissue Doppler and strain echocardiography in current clinical practice.," Circulation, vol. 116, no. 22, pp. 2597–2609, Nov. 2007.

[43]   B. H. Amundsen, T. Helle-Valle, T. Edvardsen, H. Torp, J. Crosby, E. Lyseggen, A. Støylen, H. Ihlen, J. A. C. Lima, O. A. Smiseth, and S. A. Slørdahl, "Noninvasive Myocardial Strain Measurement by Speckle Tracking Echocardiography," Journal of the American College of Cardiology, vol. 47, no. 4, pp. 789–793, Feb. 2006.

[44]   Q. Duan, E. Angelini, O. Gerard, S. Homma, and A. Laine, "Comparing optical-flow based methods for quantification of myocardial deformations on RT3D ultrasound," 2006. 3rd IEEE International Symposium on Biomedical Imaging: Nano to Macro, pp. 173–176, 2006.

[45]   M. S. Suffoletto, K. Dohi, M. Cannesson, S. Saba, and J. Gorcsan, "Novel speckle-tracking radial strain from routine black-and-white echocardiographic images to quantify dyssynchrony and predict response to cardiac resynchronization therapy," Circulation, vol. 113, no. 7, pp. 960–968, 2006.

[46]   T. Edvardsen, H. Skulstad, S. Aakhus, S. Urheim, and H. Ihlen, "Regional myocardial systolic function during acute myocardial ischemia assessed by strain Doppler echocardiography," Journal of the American College of Cardiology, vol. 37, no. 3, pp. 726–730, Mar. 2001.

[47]   J. Koyama, P. A. Ray-Sequin, and R. H. Falk, "Longitudinal Myocardial Function Assessed by Tissue Velocity, Strain, and Strain Rate Tissue Doppler Echocardiography in Patients With AL (Primary) Cardiac Amyloidosis," circ.ahajournals.org.

[48]   T. Ishizu, Y. Seo, Y. Enomoto, H. Sugimori, M. Yamamoto, T. Machino, R. Kawamura, and K. Aonuma, "Experimental validation of left ventricular transmural strain gradient with echocardiographic two-dimensional speckle tracking imaging.," Eur J Echocardiogr, vol. 11, no. 4, pp. 377–385, May 2010.

[49]   F. G. Hage, S. Raslan, P. Dean, and N. C. Nanda, "Real Time Three-Dimensional Transthoracic Echocardiography in Congenital Heart Disease.," Echocardiography, Nov. 2011.

[50]   A. Kurklinsky and S. Mankad, "Three-dimensional Echocardiography in Valvular Heart Disease.," Cardiol Rev, vol. 20, no. 2, pp. 66–71, Mar. 2012.

[51]   M. J. Monaghan, "Role of real time 3D echocardiography in evaluating the left ventricle," Heart, vol. 92, no. 1, pp. 131–136, Jan. 2006.

[52]   R. Samir, M. Tawfik, A. M. El Missiri, G. El Shahid, M. A. Maaty, and M. El Sayed, "Assessment of Left Ventricular Mechanical Dyssynchrony Using Real Time Three-Dimensional Echocardiography: A Comparative Study to Doppler Tissue Imaging.," Echocardiography, Nov. 2011.

[53]   Y. Li, C. D. Garson, Y. Xu, R. J. Beyers, F. H. Epstein, B. A. French, and J. A. Hossack, "Quantification and MRI Validation of Regional Contractile Dysfunction in Mice Post Myocardial Infarction Using High Resolution Ultrasound," Ultrasound in Medicine & Biology, vol. 33, no. 6, pp. 894–904, Jun. 2007.

[54]   A. Thorstensen, H. Dalen, P. Hala, G. Kiss, J. D'hooge, H. Torp, A. Støylen, and B. Amundsen, "Three-dimensional echocardiography in the evaluation of global and regional function in patients with recent myocardial infarction: a comparison with magnetic resonance imaging.," Echocardiography, vol. 30, no. 6, pp. 682–692, Jul. 2013.

[55]   C. Russo, Z. Jin, S. Homma, T. Rundek, M. S. V. Elkind, R. L. Sacco, and M. R. Di Tullio, "Relationship of Multidirectional Myocardial Strain with Radial Thickening and Ejection Fraction and Impact of Left Ventricular Hypertrophy: A Study in a Community-Based Cohort," Echocardiography, vol. 30, no. 7, pp. 794–802, 2013.

[56]   J. L. Hare, J. K. Brown, and T. H. Marwick, "Association of Myocardial Strain With Left Ventricular Geometry and Progression of Hypertensive Heart Disease," The American Journal of Cardiology, vol. 102, no. 1, pp. 87–91, Jul. 2008.

[57]   S.-J. Kang, H.-S. Lim, B.-J. Choi, S.-Y. Choi, G.-S. Hwang, M.-H. Yoon, S.-J. Tahk, and J.-H. Shin, "Longitudinal Strain and Torsion Assessed by Two-Dimensional Speckle Tracking Correlate with the Serum Level of Tissue Inhibitor of Matrix Metalloproteinase-1, a Marker of Myocardial Fibrosis, in Patients with Hypertension," Journal of the American Society of Echocardiography, vol. 21, no. 8, pp. 907–911, Aug. 2008.

[58]   T. Stanton, R. Leano, and T. H. Marwick, "Prediction of All-Cause Mortality From Global Longitudinal Speckle Strain Comparison With Ejection Fraction and Wall Motion Scoring," Circ Cardiovasc Imaging, vol. 2, no. 5, pp. 356–364, Sep. 2009.

[59]   C. Russo, Z. Jin, S. Homma, M. S. V. Elkind, T. Rundek, M. Yoshita, C. DeCarli, C. B. Wright, R. L. Sacco, and M. R. Di Tullio, "Subclinical left ventricular dysfunction and silent cerebrovascular disease: the Cardiovascular Abnormalities and Brain Lesions (CABL) study.," Circulation, vol. 128, no. 10, pp. 1105–1111, Sep. 2013.

[60]   M. Becker, C. Ocklenburg, E. Altiok, A. Füting, J. Balzer, G. Krombach, M. Lysyansky, H. Kühl, R. Krings, M. Kelm, and R. Hoffmann, "Impact of infarct transmurality on layer-specific impairment of myocardial function: a myocardial deformation imaging study," Eur. Heart J., vol. 30, no. 12, pp. 1467–1476, Jun. 2009.

[61]   F. Jamal, T. Kukulski, G. R. Sutherland, F. Weidemann, J. D'hooge, B. Bijnens, and G. Derumeaux, "Can changes in systolic longitudinal deformation quantify regional myocardial function after an acute infarction? An ultrasonic strain rate and strain study.," J Am Soc Echocardiogr, vol. 15, no. 7, pp. 723–730, Jul. 2002.

[62]   C.-M. Yu, J. W.-H. Fung, Q. Zhang, C.-K. Chan, Y.-S. Chan, H. Lin, L. C. C. Kum, S.-L. Kong, Y. Zhang, and J. E. Sanderson, "Tissue Doppler imaging is superior to strain rate imaging and postsystolic shortening on the prediction of reverse remodeling in both ischemic and nonischemic heart failure after cardiac resynchronization therapy.," Circulation, vol. 110, no. 1, pp. 66–73, Jul. 2004.

[63]   M. S. Suffoletto, K. Dohi, M. Cannesson, S. Saba, and J. Gorcsan, "Novel Speckle-Tracking Radial Strain From Routine Black-and-White Echocardiographic Images to Quantify Dyssynchrony and Predict Response to Cardiac Resynchronization Therapy," circ.ahajournals.org.

[64]   V. Mor-Avi, R. M. Lang, L. P. Badano, M. Belohlavek, N. M. Cardim, G. Derumeaux, M. Galderisi, T. Marwick, S. F. Nagueh, P. P. Sengupta, R. Sicari, O. A. Smiseth, B. Smulevitz, M. Takeuchi, J. D. Thomas, M. Vannan, J. U. Voigt, J. L. Zamorano, From the University of Chicago, Chicago, Illinois (V.M.-A., R.M.L.); the University of Padua, Padua, Italy (L.P.B.); Mayo Clinic, Scottsdale, Arizona (M.B.); Hospital da Luz, Lisbon, Portugal (N.M.C.); Universite Claude Bernard Lyon 1, Lyon, France (G.D.), "Current and evolving echocardiographic techniques for the quantitative evaluation of cardiac

mechanics: ASE/EAE consensus statement on methodology and indications endorsed by the Japanese Society of Echocardiography.," Eur J Echocardiogr, vol. 12, no. 3, pp. 167–205, Mar. 2011.

[65]   J. Kjaergaard, J. Korinek, M. Belohlavek, J. K. Oh, P. Sogaard, and C. Hassager, "Accuracy, reproducibility, and comparability of Doppler tissue imaging by two high-end ultrasound systems.," J Am Soc Echocardiogr, vol. 19, no. 3, pp. 322–328, Mar. 2006.

[66]   L. P. Koopman, C. Slorach, W. Hui, C. Manlhiot, B. W. McCrindle, M. K. Friedberg, E. T. Jaeggi, and L. Mertens, "Comparison between Different Speckle Tracking and Color Tissue Doppler Techniques to Measure Global and Regional Myocardial Deformation in Children," J Am Soc Echocardiogr, vol. 23, no. 9, pp. 919–928, Sep. 2010.

[67]   M. Martensson, A. Bjallmark, and L.-A. Brodin, "Evaluation of tissue Doppler-based velocity and deformation imaging: a phantom study of ultrasound systems," European Journal of Echocardiography, vol. 12, no. 6, pp. 467–476, Jun. 2011.

[68]   J. Brown, C. Jenkins, and T. H. Marwick, "Use of myocardial strain to assess global left ventricular function: a comparison with cardiac magnetic resonance and 3-dimensional echocardiography.," Am. Heart J., vol. 157, no. 1, pp. 102.e1–5, Jan. 2009.

[69]   D. Hayat, M. Kloeckner, J. Nahum, E. Ecochard-Dugelay, J.-L. Dubois-Randé, D. Jean-François, P. Guéret, and P. Lim, "Comparison of real-time three-dimensional speckle tracking to magnetic resonance imaging in patients with coronary heart disease.," The American Journal of Cardiology, vol. 109, no. 2, pp. 180–186, Jan. 2012.

[70]   F. D. R. Hobbs, J. Doust, J. Mant, and M. R. Cowie, "Heart failure: Diagnosis of heart failure in primary care.," Heart, vol. 96, no. 21, pp. 1773–1777, Nov. 2010.

[71]   A. S. Pearlman, D. P. Scoblionko, and A. K. Saal, "Assessment of valvular heart disease by doppler echocardiography," Clin Cardiol, vol. 6, no. 12, pp. 573–587, Dec. 1983.

[72]   O. Salehian and K. L. Chan, "Impact of three-dimensional echocardiography in valvular heart disease.," Curr. Opin. Cardiol., vol. 20, no. 2, pp. 122–126, Mar. 2005.

[73]   S. Urheim, T. Edvardsen, H. Torp, B. Angelsen, and O. A. Smiseth, "Myocardial strain by Doppler echocardiography. Validation of a new method to quantify regional myocardial function.," Circulation, vol. 102, no. 10, pp. 1158–1164, Sep. 2000.

[74]   J. D'hooge, E. Konofagou, F. Jamal, A. Heimdal, L. Barrios, B. Bijnens, J. Thoen, F. Van de Werf, G. Sutherland, and P. Suetens, "Two-dimensional ultrasonic strain rate measurement of the human heart in vivo.," IEEE Trans Ultrason Ferroelectr Freq Control, vol. 49, no. 2, pp. 281–286, Feb. 2002.

[75]   H. Geyer, G. Caracciolo, H. Abe, S. Wilansky, S. Carerj, F. Gentile, H.-J. Nesser, B. Khandheria, J. Narula, and P. P. Sengupta, "Assessment of Myocardial Mechanics Using Speckle Tracking Echocardiography: Fundamentals and Clinical Applications," Journal of the American Society of Echocardiography, vol. 23, no. 4, pp. 351–369, Apr.

2010.

[76]   Q. Duan, E. D. Angelini, S. L. Herz, O. Gerard, P. Allain, C. M. Ingrassia, K. D. Costa, J. W. Holmes, S. Homma, and A. F. Laine, "Tracking of LV endocardial surface on real-time three-dimensional ultrasound with optical flow," Lect Notes Comput Sci, vol. 3504, pp. 434–445, 2005.

[77]   Q. Duan, E. D. Angelini, A. Lorsakul, S. Homma, J. W. Holmes, and A. F. Laine, "Coronary Occlusion Detection with 4D Optical Flow Based Strain Estimation on 4D Ultrasound.," Lect Notes Comput Sci, vol. 5528, pp. 211–219, Jan. 2009.

[78]   A. Lorsakul, Q. Duan, M. Po, E. Hyodo, Y. Wang, S. Homma, and A. F. Laine, "Pipeline for the quantification of cardiac strain based on optical flow using 4D ultrasound data," presented at the 2010 36th Annual Northeast Bioengineering Conference, 2010, pp. 1–2.

[79]   C. C. Moore, C. H. Lugo-Olivieri, E. R. McVeigh, and E. A. Zerhouni, "Three-dimensional Systolic Strain Patterns in the Normal Human Left Ventricle: Characterization with Tagged MR Imaging1," Radiology, vol. 214, no. 2, pp. 453–466, Feb. 2000.

[80]   L. K. Waldman, Y. C. Fung, and J. W. Covell, "Transmural myocardial deformation in the canine left ventricle. Normal in vivo three-dimensional finite strains.," Circulation Research, vol. 57, no. 1, pp. 152–163, Jul. 1985.

[81]   A. Lorsakul, V. Gamarnik, Q. Duan, C. Russo, E. Angelini, S. Homma, and A. F. Laine, "Impact of temporal resolution on LV myocardial regional strain assessment with real-time 3D ultrasound.," Conf Proc IEEE Eng Med Biol Soc, vol. 2012, pp. 4075–4078, 2012.

[82]   Q. Duan, E. D. Angelini, and A. Laine, "Assessment of visual quality and spatial accuracy of fast anisotropic diffusion and scan conversion algorithms for real-time three-dimensional spherical ultrasound," Society of Photo-Optical Instrumentation Engineers (SPIE) Conference Series, vol. 5373, pp. 331–342, Apr. 2004.

[83]   P. Perona and J. Malik, "Scale-space and edge detection using anisotropic diffusion," Pattern Analysis and Machine Intelligence, IEEE Transactions on, vol. 12, no. 7, pp. 629–639, Jul. 1990.

[84]   J. Weickert, B. H. Romeny, and M. A. Viergever, "Efficient and reliable schemes for nonlinear diffusion filtering.," IEEE Trans. on Image Process., vol. 7, no. 3, pp. 398–410, 1998.

[85]   J. Montagnat, M. Sermesant, H. Delingette, G. Malandain, and N. Ayache, "Anisotropic filtering for model-based segmentation of 4D cylindrical echocardiographic images," Pattern Recognition Letters, vol. 24, no. 4, pp. 815–828, Feb. 2003.

[86]   A. Lorsakul, Q. Duan, M. J. Po, E. Angelini, S. Homma, and A. F. Laine, "Parameterization of real-time 3D speckle tracking framework for cardiac strain assessment.," Conf Proc IEEE Eng Med Biol Soc, vol. 2011, pp. 2654–2657, 2011.

[87]   S. Herz, T. Pulerwitz, K. Hirata, A. Laine, and M. DiTullio, Novel Technique for Quantitative Wall Motion Analysis Using Real-Time Three-Dimensional Echocardiography. Proceedings of the 15th …, 2004.

[88]   P. Anandan, "A computational framework and an algorithm for the measurement of visual motion," Int J Comput Vision, vol. 2, no. 3, pp. 283–310, Jan. 1989.

[89]   A. Singh, "An estimation-theoretic framework for image-flow computation," presented at the Third International Conference on Computer Vision, 1990, pp. 168–177.

[90]   W. M. Lai, D. Rubin, and E. Krempl, Introduction to Continuum Mechanics. Gulf Professional Publishing, 1996.

[91]   E. Abate, G. E. Hoogslag, M. L. Antoni, G. Nucifora, V. Delgado, E. R. Holman, M. J. Schalij, J. J. Bax, and N. A. Marsan, "Value of Three-Dimensional Speckle-Tracking Longitudinal Strain for Predicting Improvement of Left Ventricular Function After Acute Myocardial Infarction," The American Journal of Cardiology, vol. 110, no. 7, pp. 961–967, Oct. 2012.

[92]   V. Gamarnik, C. Russo, E. Angelini, and A. Laine, "Toward Diagnostic Criteria for Left Ventricular Systolic Dysfunction from Myocardial Deformation," presented at the IEEE International Conference on Biomedical Health Informatics,, Barcelona, Spain, 2014, pp. 688–692.

[93]   K. Kaku, M. Takeuchi, W. Tsang, K. Takigiku, S. Yasukochi, A. R. Patel, V. Mor-Avi, R. M. Lang, and Y. Otsuji, "Age-Related Normal Range of Left Ventricular Strain and Torsion Using Three-Dimensional Speckle-Tracking Echocardiography," Journal of the American Society of Echocardiography, vol. 27, no. 1, pp. 55–64, Jan. 2014.

[94]   K. Ozawa, N. Funabashi, H. Takaoka, and Y. Kobayashi, "2D AND 3D GLOBAL LONGITUDINAL STRAIN OF RIGHT VENTRICLE AS WELL AS LEFT VENTRICLE USING TRANSTHORACIC ECHOCARDIOGRAPHY DIFFERENTIATE HYPERTROPHIC CARDIOMYOPATHY SUBJECTS FROM CONTROLS," Journal of the American College of Cardiology, vol. 63, no. 12, p. A849, Apr. 2014.

[95]   G. Pedrizzetti, S. Sengupta, G. Caracciolo, C. S. Park, M. Amaki, G. Goliasch, J. Narula, and P. P. Sengupta, "Three-Dimensional Principal Strain Analysis for Characterizing Subclinical Changes in Left Ventricular Function," Journal of the American Society of Echocardiography, vol. 27, no. 10, pp. 1041–1050.e1, Oct. 2014.

[96]   Z. Zhang, M. Zhu, M. Ashraf, C. S. Broberg, D. J. Sahn, and X. Song, "Right ventricular strain analysis from three-dimensional echocardiography by using temporally diffeomorphic motion estimation," Medical Physics, vol. 41, no. 12, p. 122902, Dec. 2014.

[97]   D. Muraru, U. Cucchini, S. Mihăilă, M. H. Miglioranza, P. Aruta, G. Cavalli, A. Cecchetto, S. Padayattil-Josè, D. Peluso, S. Iliceto, and L. P. Badano, "Left Ventricular Myocardial Strain by Three-Dimensional Speckle-Tracking Echocardiography in Healthy Subjects: Reference Values and Analysis of Their Physiologic and Technical

Determinants," Journal of the American Society of Echocardiography, vol. 27, no. 8, pp. 858–871.e1, Aug. 2014.

[98]   W. Dinh, W. Nickl, J. Smettan, F. Kramer, T. Krahn, T. Scheffold, M. C. Barroso, H. Brinkmann, T. Koehler, M. Lankisch, and R. Füth, "Reduced global longitudinal strain in association to increased left ventricular mass in patients with aortic valve stenosis and normal ejection fraction: a hybrid study combining echocardiography and magnetic resonance imaging," Cardiovascular Ultrasound, vol. 8, no. 1, p. 29, Jul. 2010.

[99]   Y. Mizuguchi, Y. Oishi, H. Miyoshi, A. Iuchi, N. Nagase, and T. Oki, "Concentric left ventricular hypertrophy brings deterioration of systolic longitudinal, circumferential, and radial myocardial deformation in hypertensive patients with preserved left ventricular pump function," Journal of Cardiology, vol. 55, no. 1, pp. 23–33, Jan. 2010.

[100]   K. Saito, H. Okura, N. Watanabe, A. Hayashida, K. Obase, K. Imai, T. Maehama, T. Kawamoto, Y. Neishi, and K. Yoshida, "Comprehensive Evaluation of Left Ventricular Strain Using Speckle Tracking Echocardiography in Normal Adults: Comparison of Three-Dimensional and Two-Dimensional Approaches," Journal of the American Society of Echocardiography, vol. 22, no. 9, pp. 1025–1030, Sep. 2009.

[101]   M. Altman, C. Bergerot, A. Aussoleil, E. S. Davidsen, F. Sibellas, M. Ovize, E. Bonnefoy-Cudraz, H. Thibault, and G. Derumeaux, "Assessment of left ventricular systolic function by deformation imaging derived from speckle tracking: a comparison between 2D and 3D echo modalities," European Heart Journal - Cardiovascular Imaging, vol. 15, no. 3, pp. 316–323, Mar. 2014.

[102]   C. B. Compas, E. Y. Wong, X. Huang, S. Sampath, B. A. Lin, P. Pal, X. Papademetris, K. Thiele, D. P. Dione, M. Stacy, L. H. Staib, A. J. Sinusas, M. O'Donnell, and J. S. Duncan, "Radial basis functions for combining shape and speckle tracking in 4D echocardiography. - PubMed - NCBI," Medical Imaging, IEEE Transactions on, vol. 33, no. 6, pp. 1275–1289, Jun. 2014.

[103]   M. De Craene, G. Piella, O. Camara, N. Duchateau, E. Silva, A. Doltra, J. D'hooge, J. Brugada, M. Sitges, and A. F. Frangi, "Temporal diffeomorphic free-form deformation: Application to motion and strain estimation from 3D echocardiography," Medical Image Analysis, vol. 16, no. 2, pp. 427–450, Feb. 2012.

[104]   S. A. Kleijn, N. G. Pandian, J. D. Thomas, L. Perez de Isla, O. Kamp, M. Zuber, P. Nihoyannopoulos, T. Forster, H. J. Nesser, A. Geibel, W. Gorissen, and J. L. Zamorano, "Normal reference values of left ventricular strain using three-dimensional speckle tracking echocardiography: results from a multicentre study," European Heart Journal - Cardiovascular Imaging, vol. 16, no. 4, pp. 410–416, Mar. 2015.

[105]   S. Yuda, Y. Sato, K. Abe, M. Kawamukai, H. Kouzu, A. Muranaka, N. Kokubu, A. Hashimoto, K. Tsuchihashi, N. Watanabe, and T. Miura, "Inter-Vendor Variability of Left Ventricular Volumes and Strains Determined by Three-Dimensional Speckle Tracking Echocardiography," Echocardiography, vol. 31, no. 5, pp. 597–604, May

174

2014.

[106]   E. Gayat, H. Ahmad, L. Weinert, R. M. Lang, and V. Mor-Avi, "Reproducibility and inter-vendor variability of left ventricular deformation measurements by three-dimensional speckle-tracking echocardiography.," J Am Soc Echocardiogr, vol. 24, no. 8, pp. 878–885, Aug. 2011.

[107]   S. E. Fischer, G. C. McKinnon, S. E. Maier, and P. Boesiger, "Improved myocardial tagging contrast.," Magn. Reson. Med., vol. 30, no. 2, pp. 191–200, Aug. 1993.

[108]   M. J. W. Götte, T. Germans, I. K. Rüssel, J. J. M. Zwanenburg, J. T. Marcus, A. C. van Rossum, and D. J. van Veldhuisen, "Myocardial Strain and Torsion Quantified by Cardiovascular Magnetic Resonance Tissue Tagging," Journal of the American College of Cardiology, vol. 48, no. 10, pp. 2002–2011, Nov. 2006.

[109]   "Three-dimensional regional strain computation method with displacement encoding with stimulated echoes (DENSE) in non-ischemic, non-valvular dilated cardiomyopathy patients and healthy subjects validated by tagged MRI.," vol. 41, no. 2, pp. 386–396, Feb. 2015.

[110]   H. Geyer, G. Caracciolo, H. Abe, S. Wilansky, S. Carerj, F. Gentile, H.-J. Nesser, B. Khandheria, J. Narula, and P. P. Sengupta, "Assessment of myocardial mechanics using speckle tracking echocardiography: fundamentals and clinical applications.," J Am Soc Echocardiogr, vol. 23, no. 4, pp. 351–69– quiz 453–5, Apr. 2010.

[111]   J. H. McGowan and J. G. F. Cleland, "Reliability of reporting left ventricular systolic function by echocardiography: A systematic review of 3 methods," Am. Heart J., vol. 146, no. 3, pp. 388–397, Sep. 2003.

[112]   M. Leitman, P. Lysyansky, S. Sidenko, and V. Shir, "Two-dimensional strain–a novel software for real-time quantitative echocardiographic assessment of myocardial function," Journal of the American Society of Echocardiography, vol. 17, no. 10, pp. 1021–1029, 2004.

[113]   S. A. Reisner, P. Lysyansky, Y. Agmon, D. Mutlak, J. Lessick, and Z. Friedman, "Global longitudinal strain: a novel index of left ventricular systolic function," Journal of the American Society of Echocardiography, vol. 17, no. 6, pp. 630–633, Jun. 2004.

[114]   J. D'Hooge, E. Konofagou, F. Jamal, A. Heimdal, L. Barrios, B. Bijnens, J. Thoen, F. Van de Werf, G. Sutherland, and P. Suetens, "Two-dimensional ultrasonic strain rate measurement of the human heart in vivo," IEEE Trans Ultrason Ferroelectr Freq Control, vol. 49, no. 2, pp. 281–286, Feb. 2002.

[115]   Q. Wang, Y. Gao, K. Tan, H. Xia, and P. Li, "Assessment of left ventricular function by three-dimensional speckle-tracking echocardiography in well-treated type 2 diabetes patients with or wit... - PubMed - NCBI," J. Clin. Ultrasound, vol. 43, no. 8, pp. 502–511, Mar. 2015.

[116]   R. F. Duncan, B. K. Dundon, A. J. Nelson, J. Pemberton, K. Williams, M. I. Worthley, A. Zaman, H. Thomas, and S. G. Worthley, "A Study of the 16-Segment Regional Wall

Motion Scoring Index and Biplane Simpson's Rule for the Calculation of Left Ventricular Ejection Fraction: A Comparison with Cardiac Magnetic Resonance Imaging," Echocardiography, vol. 28, no. 6, pp. 597–604, Jul. 2011.

[117]   V. Gamarnik, C. Russo, E. Angelini, and A. Laine, "Toward diagnostic criteria for left ventricular systolic dysfunction from myocardial deformation," presented at the Biomedical and Health Informatics (BHI), 2014 IEEE-EMBS International Conference on, 2014, pp. 688–692.

[118]   T. Yingchoncharoen, S. Agarwal, Z. B. Popović, and T. H. Marwick, "Normal ranges of left ventricular strain: a meta-analysis. - PubMed - NCBI," Journal of the American Society of Echocardiography, vol. 26, no. 2, pp. 185–191, Feb. 2013.

[119]   M. Becker, A. Lenzen, C. Ocklenburg, K. Stempel, H. Kühl, M. Neizel, M. Katoh, R. Kramann, J. Wildberger, M. Kelm, and R. Hoffmann, "Myocardial Deformation Imaging Based on Ultrasonic Pixel Tracking to Identify Reversible Myocardial Dysfunction," Journal of the American College of Cardiology, vol. 51, no. 15, pp. 1473–1481, Apr. 2008.

[120]   L. Afonso, A. Kondur, M. Simegn, A. Niraj, P. Hari, R. Kaur, P. Ramappa, J. Pradhan, D. Bhandare, K. A. Williams, S. Zalawadiya, A. Pinheiro, and T. P. Abraham, "Two-dimensional strain profiles in patients with physiological and pathological hypertrophy and preserved left ventricular systolic function: a comparative analyses," BMJ Open, vol. 2, no. 4, pp. e001390–e001390, Jan. 2012.

[121]   J. Korinek, J. Vitek, P. P. Sengupta, A. Romero-Corral, V. K. Krishnamoorthy, E. M. McMahon, B. K. Khandheria, and M. Belohlavek, "Does implantation of sonomicrometry crystals alter regional cardiac muscle function?," J Am Soc Echocardiogr, vol. 20, no. 12, pp. 1407–1412, Dec. 2007.

[122]   E. Lyseggen, H. Skulstad, T. Helle-Valle, T. Vartdal, S. Urheim, S. I. Rabben, A. Opdahl, H. Ihlen, and O. A. Smiseth, "Myocardial strain analysis in acute coronary occlusion: a tool to assess myocardial viability and reperfusion.," Circulation, vol. 112, no. 25, pp. 3901–3910, Dec. 2005.

[123]   D. Oxborough, K. George, and K. M. Birch, "Intraobserver Reliability of Two-Dimensional Ultrasound Derived Strain Imaging in the Assessment of the Left Ventricle, Right Ventricle, and Left Atrium of Healthy Human Hearts," Echocardiography, vol. 29, no. 7, pp. 793–802, Aug. 2012.

[124]   X. Zhou, P. Thavendiranathan, Y. Chen, L. Cheng, Z. Qian, S. Liu, H. Houle, G. Zhi, and M. A. Vannan, "Feasibility of Automated Three-Dimensional Rotational Mechanics by Real-Time Volume Transthoracic Echocardiography: Preliminary Accuracy and Reproducibility Data Compared with Cardiovascular Magnetic Resonance," Journal of the American Society of Echocardiography, Sep. 2015.

[125]   P. P. Swoboda, A. Larghat, A. Zaman, T. A. Fairbairn, M. Motwani, J. P. Greenwood, and S. Plein, "Reproducibility of myocardial strain and left ventricular twist measured using complementary spatial modulation of magnetization," J. Magn. Reson. Imaging,

vol. 39, no. 4, pp. 887–894, Apr. 2014.

[126] C. Russo, M.-P. Jaubert, Z. Jin, S. Homma, and M. R. Di Tullio, "Intra- and interobserver reproducibility of left ventricular mechanical dyssynchrony assessment by real time three-dimensional echocardiography.," Echocardiography, vol. 29, no. 5, pp. 598–607, May 2012.

[127] T. Kuznetsova, L. Herbots, T. Richart, J. D'hooge, L. Thijs, R. H. Fagard, M.-C. Herregods, and J. A. Staessen, "Left ventricular strain and strain rate in a general population," Eur. Heart J., vol. 29, no. 16, pp. 2014–2023, Aug. 2008.

[128] E.-S. H. Ibrahim, "Myocardial tagging by Cardiovascular Magnetic Resonance: evolution of techniques--pulse sequences, analysis algorithms, and applications," Journal of Cardiovascular Magnetic Resonance, vol. 13, no. 36, 2011.

[129] L. Axel and L. Dougherty, "Heart wall motion: improved method of spatial modulation of magnetization for MR imaging.," Radiology, 1989.

[130] L. Axel and L. Dougherty, "MR imaging of motion with spatial modulation of magnetization.," Radiology, 1989.

[131] S. Ryf, M. A. Spiegel, M. Gerber, and P. Boesiger, "Myocardial tagging with 3D-CSPAMM," J. Magn. Reson. Imaging, vol. 16, no. 3, pp. 320–325, Aug. 2002.

[132] A. K. Rutz, S. Ryf, S. Plein, P. Boesiger, and S. Kozerke, "Accelerated whole-heart 3D CSPAMM for myocardial motion quantification," Magn. Reson. Med., vol. 59, no. 4, pp. 755–763, 2008.

[133] S. Kumar and D. Goldgof, "Automatic tracking of SPAMM grid and the estimation of deformation parameters from cardiac MR images.," Medical Imaging, IEEE Transactions on, vol. 13, no. 1, pp. 122–132, 1994.

[134] M. A. Guttman, J. L. Prince, and E. R. McVeigh, "Tag and contour detection in tagged MR images of the left ventricle.," Medical Imaging, IEEE Transactions on, vol. 13, no. 1, pp. 74–88, 1994.

[135] M. A. Guttman, E. A. Zerhouni, and E. R. McVeigh, "Analysis of cardiac function from MR images," Computer Graphics and Applications, IEEE, vol. 17, no. 1, pp. 30–38, 1997.

[136] L. Dougherty, J. C. Asmuth, A. S. Blom, L. Axel, and R. Kumar, "Validation of an optical flow method for tag displacement estimation.," Medical Imaging, IEEE Transactions on, vol. 18, no. 4, pp. 359–363, Apr. 1999.

[137] A. A. Young, "Model tags: direct three-dimensional tracking of heart wall motion from tagged magnetic resonance images.," Medical Image Analysis, vol. 3, no. 4, pp. 361–372, Dec. 1999.

[138] H. Ashikaga, S. R. Mickelsen, D. B. Ennis, I. Rodriguez, P. Kellman, H. Wen, and E. R. McVeigh, "Electromechanical analysis of infarct border zone in chronic myocardial infarction.," Am. J. Physiol. Heart Circ. Physiol., vol. 289, no. 3, pp. H1099–105, Sep.

2005.

[139]   L. Feng, R. Donnino, J. Babb, L. Axel, and D. Kim, "Numerical and in vivo validation of fast cine displacement-encoded with stimulated echoes (DENSE) MRI for quantification of regional cardiac function," Magn. Reson. Med., vol. 62, no. 3, pp. 682–690, Sep. 2009.

[140]   R. C. Hendel, M. R. Patel, C. M. Kramer, M. Poon, R. C. Hendel, J. C. Carr, N. A. Gerstad, L. D. Gillam, J. M. Hodgson, R. J. Kim, C. M. Kramer, J. R. Lesser, E. T. Martin, J. V. Messer, R. F. Redberg, G. D. Rubin, J. S. Rumsfeld, A. J. Taylor, W. G. Weigold, P. K. Woodard, R. G. Brindis, R. C. Hendel, P. S. Douglas, E. D. Peterson, M. J. Wolk, J. M. Allen, and M. R. Patel, "ACCF/ACR/SCCT/SCMR/ASNC/NASCI/SCAI/SIR 2006 Appropriateness Criteria for Cardiac Computed Tomography and Cardiac Magnetic Resonance Imaging∗ ∗Developed in accordance with the principles and methodology outlined by ACCF: Patel MR, Spertus JA, Brindis RG, Hendel RC, Douglas PS, Peterson ED, Wolk MJ, Allen JM, Raskin IE. ACCF proposed method for evaluating the appropriateness of cardiovascular imaging. J Am Coll Cardiol 2005;46:1606–13.," Journal of the American College of Cardiology, vol. 48, no. 7, pp. 1475–1497, Oct. 2006.

[141]   J. Bogaert, S. Dymarkowski, A. M. Taylor, and V. Muthurangu, Clinical Cardiac MRI. Springer Science & Business Media, 2012.

[142]   A. T. Hess, X. Zhong, B. S. Spottiswoode, F. H. Epstein, and E. M. Meintjes, "Myocardial 3D strain calculation by combining cine displacement encoding with stimulated echoes (DENSE) and cine strain encoding (SENC) imaging.," Magn. Reson. Med., vol. 62, no. 1, pp. 77–84, Jul. 2009.

[143]   B. S. Spottiswoode, X. Zhong, A. T. Hess, C. M. Kramer, E. M. Meintjes, B. M. Mayosi, and F. H. Epstein, "Tracking Myocardial Motion From Cine DENSE Images Using Spatiotemporal Phase Unwrapping and Temporal Fitting," Medical Imaging, IEEE Transactions on, vol. 26, no. 1, pp. 15–30, Jan. 2007.

[144]   Chunming Li, Chenyang Xu, Changfeng Gui, and M. D. Fox, "Distance Regularized Level Set Evolution and Its Application to Image Segmentation," IEEE Trans. on Image Process., vol. 19, no. 12, pp. 3243–3254.

[145]   R. Cusack and N. Papadakis, "New robust 3-D phase unwrapping algorithms: application to magnetic field mapping and undistorting echoplanar images," Neuroimage, vol. 16, no. 3, pp. 754–764, 2002.

[146]   H. S. Abdul-Rahman, M. A. Gdeisat, D. R. Burton, M. J. Lalor, F. Lilley, and C. J. Moore, "Fast and robust three-dimensional best path phase unwrapping algorithm," Appl. Opt., AO, vol. 46, no. 26, pp. 6623–6635, Sep. 2007.

[147]   A. H. Aletras, S. Ding, R. S. Balaban, and H. Wen, "DENSE: displacement encoding with stimulated echoes in cardiac functional MRI.," J. Magn. Reson., vol. 137, no. 1, pp. 247–252, Mar. 1999.

[148]   H. Abdul-Rahman, M. Arevalillo-Herráez, M. Gdeisat, D. Burton, M. Lalor, F. Lilley, C.

Moore, D. Sheltraw, and M. Qudeisat, "Robust three-dimensional best-path phase-unwrapping algorithm that avoids singularity loops," Appl. Opt., AO, vol. 48, no. 23, pp. 4582–4596, 2009.

[149] X. Zhong, L. B. Gibberman, B. S. Spottiswoode, A. D. Gilliam, C. H. Meyer, B. A. French, and F. H. Epstein, "Comprehensive cardiovascular magnetic resonance of myocardial mechanics in mice using three-dimensional cine DENSE.," J Cardiovasc Magn Reson, vol. 13, no. 1, p. 83, 2011.

[150] X. Zhong, B. S. Spottiswoode, C. H. Meyer, C. M. Kramer, and F. H. Epstein, "Imaging Three-Dimensional Myocardial Mechanics Using Navigator-Gated Volumetric Spiral Cine DENSE MRI," Magn. Reson. Med., vol. 64, no. 4, pp. 1089–1097, Oct. 2010.

[151] Y. Zhang, S. Wang, G. Ji, and Z. Dong, "An Improved Quality Guided Phase Unwrapping Method and Its Applications to MRI," Progress in Electromagnetics Research-Pier, vol. 145, pp. 273–286, 2014.

[152] N. Paragios, "A level set approach for shape-driven segmentation and tracking of the left ventricle," Medical Imaging, IEEE Transactions on, vol. 22, no. 6, pp. 773–776, Jun. 2003.

[153] L. Yang, B. Georgescu, Y. Zheng, P. Meer, and D. Comaniciu, "3D ultrasound tracking of the left ventricle using one-step forward prediction and data fusion of collaborative trackers," Computer Vision and …, pp. 1–8, 2008.

[154] F. Orderud, J. Hansgård, and S. I. Rabben, "Real-time tracking of the left ventricle in 3D echocardiography using a state estimation approach.," Med Image Comput Comput Assist Interv, vol. 10, no. 1, pp. 858–865, 2007.

[155] Q. Duan, E. D. Angelini, S. L. Herz, C. M. Ingrassia, K. D. Costa, J. W. Holmes, S. Homma, and A. F. Laine, "Region-based endocardium tracking on real-time three-dimensional ultrasound.," Ultrasound in Medicine & Biology, vol. 35, no. 2, pp. 256–265, Feb. 2009.

[156] A. Myronenko, X. Song, and D. J. Sahn, "LV motion tracking from 3D echocardiography using textural and structural information.," Med Image Comput Comput Assist Interv, vol. 10, no. 2, pp. 428–435, 2007.

[157] E. D. Angelini, S. Homma, G. Pearson, J. W. Holmes, and A. F. Laine, "Segmentation of real-time three-dimensional ultrasound for quantification of ventricular function: a clinical study on right and left ventricles.," Ultrasound in Medicine & Biology, vol. 31, no. 9, pp. 1143–1158, Sep. 2005.

[158] S. L. Herz, T. Hasegawa, A. N. Makaryus, K. M. Parker, S. Homma, J. Wang, and J. W. Holmes, "Quantitative three-dimensional wall motion analysis predicts ischemic region size and location.," Ann Biomed Eng, vol. 38, no. 4, pp. 1367–1376, Apr. 2010.

[159] S. J. Osher and R. P. Fedkiw, Level Set Methods and Dynamic Implicit Surfaces, 1st ed. Springer, 2002.

[160] J. A. Sethian, Level set methods and fast marching methods : evolving interfaces in

computational geometry, fluid mechanics, computer vision, and materials science. Cambridge, U.K. ; New York : Cambridge University Press, 1999.

[161]   X. Deng and G. Du, "Editorial: 3D segmentation in the clinic: a grand challenge II-liver tumor segmentation," MICCAI Workshop, 2008.

[162]   J. E. McManigle, R. V. Stebbing, and J. A. Noble, "Modified Hough transform for left ventricle myocardium segmentation in 3-D echocardiogram images," 2012 IEEE 9th International Symposium on Biomedical Imaging (ISBI 2012), pp. 290–293.

[163]   Q. Duan, E. D. Angelini, and A. F. Laine, "Real-time segmentation by Active Geometric Functions," Computer Methods and Programs in Biomedicine, vol. 98, no. 3, pp. 223–230, Jun. 2010.

[164]   S. Brekke, S. I. Rabben, A. Støylen, A. Haugen, G. U. Haugen, E. N. Steen, and H. Torp, "Volume stitching in three-dimensional echocardiography: distortion analysis and extension to real time.," Ultrasound in Medicine & Biology, vol. 33, no. 5, pp. 782–796, May 2007.

[165]   R. Mukherjee, C. Sprouse, A. Pinheiro, T. Abraham, and P. Burlina, "Computing Myocardial Motion in 4-Dimensional Echocardiography," Ultrasound in Medicine & Biology, vol. 38, no. 7, pp. 1284–1297, Jul. 2012.

[166]   A. Mignot, E. Donal, A. Zaroui, P. Reant, A. Salem, C. Hamon, S. Monzy, R. Roudaut, G. Habib, and S. Lafitte, "Global Longitudinal Strain as a Major Predictor of Cardiac Events in Patients with Depressed Left Ventricular Function: A Multicenter Study," Journal of the American Society of Echocardiography, vol. 23, no. 10, pp. 1019–1024, Oct. 2010.

[167]   M. Cameli, F. M. Righini, M. Lisi, E. Bennati, R. Navarri, S. Lunghetti, M. Padeletti, P. Cameli, C. Tsioulpas, S. Bernazzali, M. Maccherini, G. Sani, M. Henein, and S. Mondillo, "Comparison of Right Versus Left Ventricular Strain Analysis as a Predictor of Outcome in Patients With Systolic Heart Failure Referred for Heart Transplantation," The American Journal of Cardiology, vol. 112, no. 11, pp. 1778–1784, Dec. 2013.

[168]   S. W. Choi, J.-H. Park, B. J. Sun, Y. Park, Y. J. Kim, I. S. Lee, M. S. Kim, J.-H. Kim, J.-H. Lee, J.-O. Jeong, I. S. Kwon, and I.-W. Seong, "Impaired two-dimensional global longitudinal strain of left ventricle predicts adverse long-term clinical outcomes in patients with acute myocardial infarction," International Journal of Cardiology, vol. 196, pp. 165–167, Oct. 2015.

[169]   R. Hachamovitch and M. F. Di Carli, "Methods and Limitations of Assessing New Noninvasive Tests Part I: Anatomy-Based Validation of Noninvasive Testing," Circulation, vol. 117, no. 20, pp. 2684–2690, May 2008.

[170]   R. Hachamovitch and M. F. Di Carli, "Methods and limitations of assessing new noninvasive tests: Part II: Outcomes-based validation and reliability assessment of noninvasive testing.," Circulation, vol. 117, no. 21, pp. 2793–2801, May 2008.

[171]   D. J. Schneck and J. D. Bronzino, Biomechanics: Principles and Applications.

Productivity Press, 2003.

[172]   M. Kowalski, T. Kukulski, F. Jamal, J. D'Hooge, F. Weidemann, F. Rademakers, B. Bijnens, L. Hatle, and G. R. Sutherland, "Can natural strain and strain rate quantify regional myocardial deformation? A study in healthy subjects.," Ultrasound in Medicine & Biology, vol. 27, no. 8, pp. 1087–1097, Aug. 2001.

[173]   T. H. Marwick, "Measurement of Strain and Strain Rate by Echocardiography," Journal of the American College of Cardiology, vol. 47, no. 7, pp. 1313–1327, Apr. 2006.

[174]   T. Kukulski, F. Jamal, L. Herbots, J. D'hooge, B. Bijnens, L. Hatle, I. De Scheerder, and G. R. Sutherland, "Identification of acutely ischemic myocardium using ultrasonic strain measurements," Journal of the American College of Cardiology, vol. 41, no. 5, pp. 810–819, Mar. 2003.

[175]   H. M. Hurlburt, G. P. Aurigemma, J. C. Hill, A. Narayanan, W. H. Gaasch, C. S. Vinch, T. E. Meyer, and D. A. Tighe, "Direct ultrasound measurement of longitudinal, circumferential, and radial strain using 2-dimensional strain imaging in normal adults.," Echocardiography, vol. 24, no. 7, pp. 723–731, Aug. 2007.

[176]   I. K. Zervantonakis, S. D. Fung-Kee-Fung, W.-N. Lee, and E. E. Konofagou, "A novel, view-independent method for strain mapping in myocardial elastography: eliminating angle and centroid dependence.," Phys Med Biol, vol. 52, no. 14, pp. 4063–4080, Jul. 2007.

[177]   W.-N. Lee, C. M. Ingrassia, S. D. Fung-Kee-Fung, K. D. Costa, J. W. Holmes, and E. E. Konofagou, "Theoretical quality assessment of myocardial elastography with in vivo validation," IEEE Trans Ultrason Ferroelectr Freq Control, vol. 54, no. 11, pp. 2233–2245, 2007.

[178]   J. Luo, W.-N. Lee, and E. E. Konofagou, "Fundamental performance assessment of 2-D myocardial elastography in a phased-array configuration.," IEEE Trans Ultrason Ferroelectr Freq Control, vol. 56, no. 10, pp. 2320–2327, Oct. 2009.

[179]   S. Nottin, G. Doucende, I. Schuster-Beck, M. Dauzat, and P. Obert, "Alteration in left ventricular normal and shear strains evaluated by 2D-strain echocardiography in the athlete's heart," J Physiol, vol. 586, no. 19, pp. 4721–4733, Oct. 2008.

Appendix A.   **Supplemental Tables and Figures**

Table A-1. Variation in the peak value of each strain component and TTPS, for each of the analyzed segments in the volunteer population from Chapter 3.

	bIS	bI	bIL	bAS	mIS	mI	mIL	mAS	aS
Ecc ±	-2.25 ±	-11.80 ±	-3.73 ±	-6.60 ±	-2.76 ±	-5.22 ±	-2.55 ±	-8.80 ±	-3.52 ±
SD	5.15	11.41	6.18	8.17	4.22	7.00	4.76	6.42	5.61
Err ±	33.68 ±	17.09 ±	34.71 ±	31.81 ±	24.71 ±	5.72 ±	22.12 ±	35.21 ±	24.44 ±
SD	21.36	17.03	20.70	25.05	17.88	14.45	17.06	20.88	18.34
Ezz ±	-9.43 ±	-10.10 ±	-10.86 ±	-8.22 ±	-11.11 ±	-5.14 ±	-7.41 ±	-11.71 ±	-9.30 ±
SD	7.94	9.21	8.21	8.81	7.18	5.08	5.31	5.99	8.06
Ecc CV	229	97	166	124	153	134	187	73	159
Err CV	63	100	60	79	72	253	77	59	75
Ezz CV	84	91	76	107	65	99	72	51	87
TTPScc	97.70 ±	383.62 ±	178.32 ±	405.43 ±	195.96 ±	329.72 ±	172.31 ±	368.85 ±	192.40 ±
± SD	249.64	417.71	280.02	416.66	317.19	398.27	307.49	402.98	317.54
TTPSrr	312.78 ±	139.99 ±	194.75 ±	262.87 ±	239.82 ±	40.17 ±	145.64 ±	262.39 ±	235.84 ±
± SD	153.98	136.61	117.27	166.22	161.61	97.74	115.70	132.01	158.32
TTPSzz	316.29 ±	380.47 ±	442.30 ±	417.84 ±	592.18 ±	398.04 ±	487.63 ±	644.91 ±	523.28 ±
± SD	377.69	397.55	402.49	379.68	354.57	423.71	402.48	367.57	366.93
TTPScc CV	256	109	157	103	162	121	178	109	165
TTPSrr CV	49	98	60	63	67	243	79	50	67
TTPSzz CV	119	104	91	91	60	106	83	57	70

Table A-2. Differences in peak strains between segments from the control (RWMSI = 2) and patient (RWMSI = 2, < 1.25) populations in Chapter 4.

	Mean Diff.	Max. Diff.	Min. Diff.
Control vs. RWMSI < 1.25			
E_{rr} (%)	17.74	29.75	5.15
E_{zz} (%)	5.87	10.14	0.17
E_{cc} (%)	2.95	6.28	0.62
Control vs. RWMSI = 2			
E_{rr} (%)	13.64	20.77	5.43
E_{zz} (%)	5.61	7.67	2.46
E_{cc} (%)	3.31	7.80	0.54
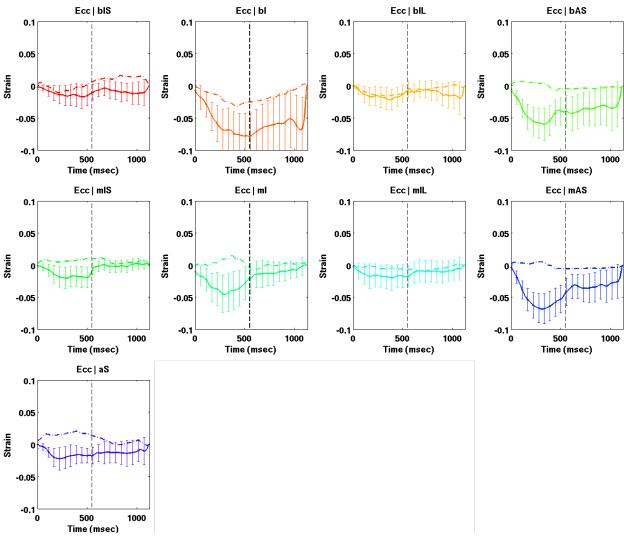
Figure A-1. Comparison of segmental circumferential strain profiles in healthy subjects (with 95% CI) and patient subgroup with RWMSI below 1.25 (dotted line). 95% CIs for patient subgroup are omitted for clarity).

185
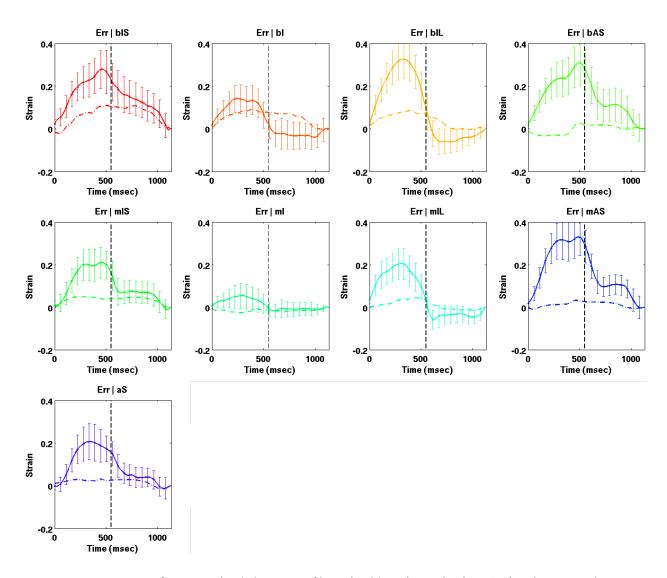
Figure A-2. Comparison of segmental radial strain profiles in healthy subjects (with 95% CI) and patient subgroup with RWMSI below 1.25 (dotted line). 95% CIs for patient subgroup are omitted for clarity).
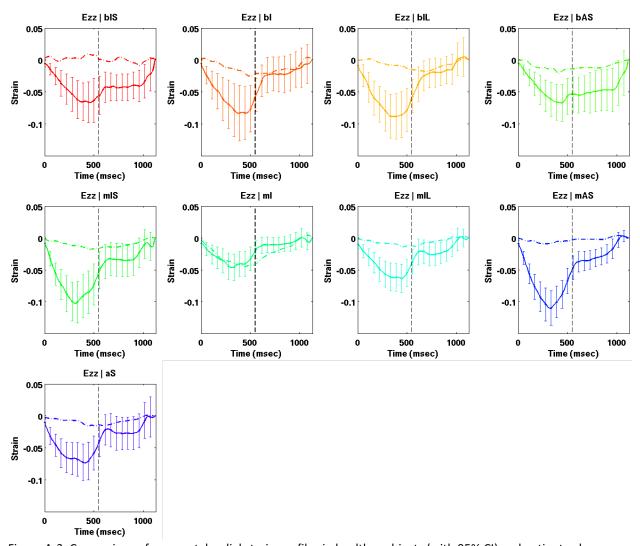
Figure A-3. Comparison of segmental radial strain profiles in healthy subjects (with 95% CI) and patient subgroup with RWMSI below 1.25 (dotted line). 95% CIs for patient subgroup are omitted for clarity).
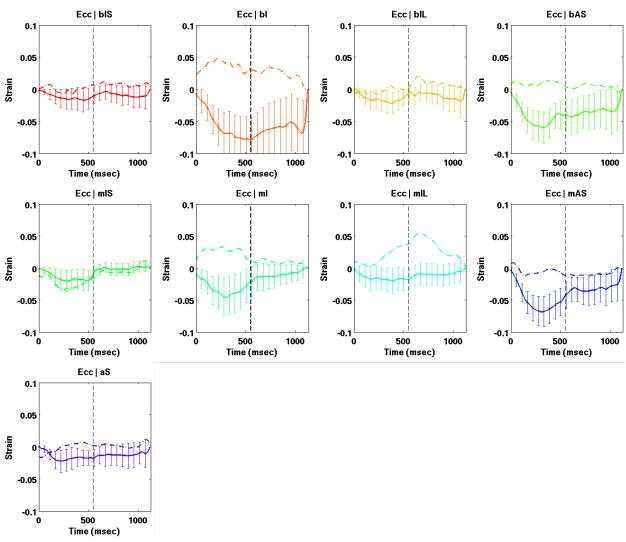
Figure A-4. Comparison of segmental circumferential strain profiles in healthy subjects (with 95% CI) and patient subgroup with RWMSI below 1.25 (dotted line). 95% CIs for patient subgroup are omitted for clarity).
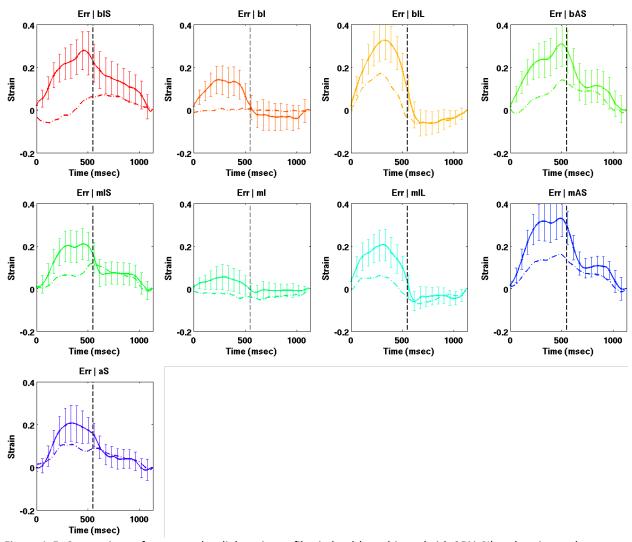
Figure A-5. Comparison of segmental radial strain profiles in healthy subjects (with 95% CI) and patient subgroup with RWMSI below 1.25 (dotted line). 95% CIs for patient subgroup are omitted for clarity).
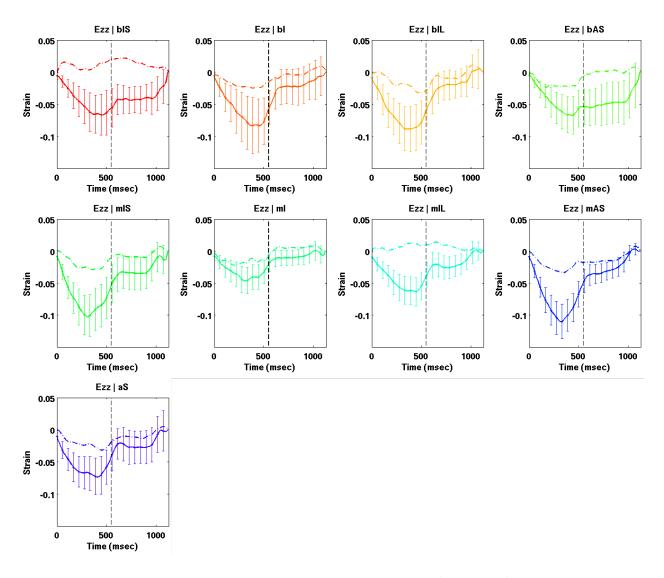
Figure A-6. Comparison of segmental radial strain profiles in healthy subjects (with 95% CI) and patient subgroup with RWMSI below 1.25 (dotted line). 95% CIs for patient subgroup are omitted for clarity).

RWMSI	E_{cc}	E_{rr}	E_{zz}	E_{cc} TTPS	E_{rr} TTPS	E_{zz} TTPS
2* vs. 2	0.0003	0.2027	0.0025	0.1971	0.0457	0.0820
2* vs. 1.25	0.0446	0.4172	0.0033	0.5998	0.1669	0.8594
2* vs. 0.75	0.0000	0.0022	0.0041	0.7601	0.1486	0.9221
2* vs. 0	0.0405	0.0325	0.5240	0.5240	0.3189	0.9179
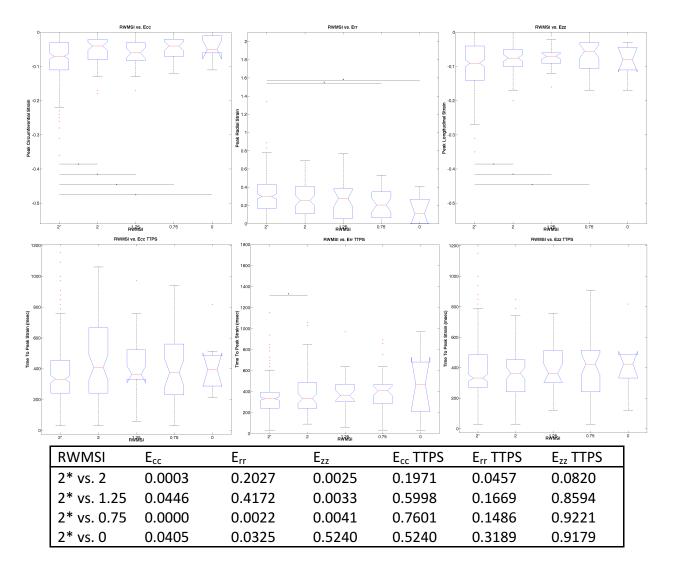
Figure A-7. Box plot comparison of peak strain and TTPS values, categorized by RWMSI in patients (0 – 2) and healthy individuals (2*). The red line represents the median value. The blue lines extend to the 25th and 75th percentiles. The dotted lines extend to the farthest samples not considered outliers. Outliers are plotted individually as red asterisks. Horizontal black lines represent significant differences at the *p < 0.05* level. No segments in the study sample demonstrated hyperkinetic (RWMSI = 3) segments. The table below shows the significance level of each comparison.

In addition to ROC analysis, we investigated whether each of the global peak strain components demonstrated any significant differences for each of the four risk factors, using the two-tailed independent samples t-test. These results are summarized below, in Table A-3.

Table A-3. Differences in mean value of peak global strains based on selected clinical risk factors

Clinical Risk Factor	N	Peak E_{rr} (%)	Peak E_{cc} (%)	Peak E_{zz} (%)
HTN-	21	60.1 ± 22.4	-19.2 ± 6.4	-19.5 ± 6.4
HTN+	9	52.2 ± 12.2	-10.6 ± 1.4	-14.6 ± 2.1
P value		0.355	0.007	0.077
HLD-	24	60.2 ± 21.0	-18.2 ± 6.6	-18.8 ± 6.3
HLD+	6	48.0 ± 12.3	-10.5 ± 1.5	-14.8 ± 1.7
P value		0.507	0.026	0.097
DM2-	25	59.3 ± 20.9	-17.9 ± 6.6	-18.8 ± 6.1
DM2+	5	50.2 ± 13.9	-10.2 ± 1.3	-14.0 ± 1.2
P value		0.733	0.034	0.076
CAD-	24	57.9 ± 21.3	-17.8 ± 6.9	-18.9 ± 6.2
CAD+	6	57.2 ± 15.3	-12.0 ± 2.8	-14.3 ± 1.4
P value		0.734	0.054	0.075

Appendix B. Evaluation of Radial Strain Estimates by Optical Flow

This section was written collaboratively with Dr. Elsa Angelini.

B.1 Introduction

Following a discussion with the dissertation committee, we sought to corroborate the veracity of the radial strain (E_{rr}) estimates calculated using the 3D OF technique and reported in Chapter 3. To this end, we examined three critical aspects of the E_{rr} estimates:

[1] First, we performed a detailed analysis of the OF pipeline source code, to ascertain that no errors were introduced into the algorithm over the course of minor revisions and updates.

[2] Next, we conducted an extensive literature review to determine the typical amplitude of E_{rr} reported both by similar (B-mode echocardiography) and alternative (MRI) techniques on human subjects with standard clinical devices and scanning protocols.

[3] Lastly, we evaluated previously published data from our group, to compare our latest results to those previously generated using the same OF-based computational pipeline.

B.2 Details of the OF-Based Strain Calculation Pipeline

Our approach to Lagrangian displacement and strain calculation incrementally tracks all points from the initial ED tissue mask. Each point is tracked in 3D, frame by frame, over the course of the cardiac cycle. Incremental displacements are accumulated into a total displacement with respect to the baseline positions at ED. The rationale for this approach was to facilitate direct comparisons with tagged MRI, which can only provide estimates by tracking an initial population of points over time, since tagging cannot introduce new points in the middle of the cardiac cycle.

194

After tracking, Lagrangian strain is computed using the same principles as aforementioned papers, but a key point is that due to the nature of the tracking method, we compute gradients always with respect to the baseline, so displacement gradients are estimated between points that were neighbors at ED, but may have moved far away over time. This implies that we do not consider the immediate neighborhood at each time frame (as would be the case if we updated the population of points being tracked in each cardiac phase). Consequently, the strain values we observe may be considerably larger when compared to techniques that compare only local neighborhoods at each time point. An approach which considers new neighbors at each time point is technically possible, but there would be a significant computational cost to identifying these newly adjacent points at each frame, while also updating the tracking routine.

A detailed outline of the source code for strain computation is provided below.

Additionally, we noted that the AHA segments are *fixed* and defined on the ED geometry, which adds the constraint that a point, which at ED is in segment 6, for example, always stays in segment 6 throughout the cardiac cycle. Since all the anatomical references and baseline coordinates are estimated at ED, this closely corresponds to the notion of "tagging" all tissue points at the initial time, but they are free to move anywhere over the cardiac cycle. However, the reality that a tissue point may cross into a different predefined segment and contribute to its deformation cannot be dismissed, and may be a source of error. Nevertheless, segments correspond to coronary perfusion, which should remain constant along time.
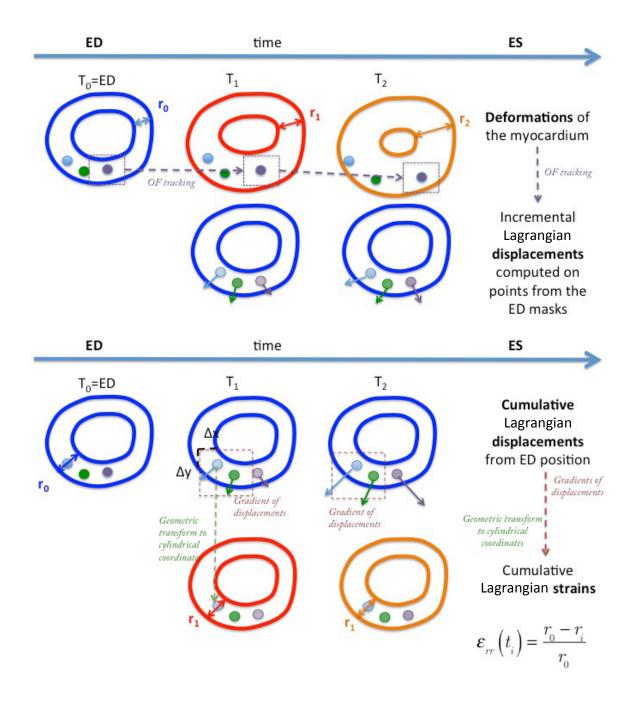
Figure B-1. Diagram of the two main steps for strain (radial) computation in the OF pipeline. Top: movement of the myocardium is quantified using speckle tracking. Bottom: Cumulative (radial) strain is calculated from the derivative of the cumulative displacement estimates, and transformed to the LV coordinate system

The equation shown in the figure:

$$\varepsilon_{rr}\left(t_i\right) = \frac{r_0 - r_i}{r_0}$$

Explanation of the computation of the cumulative strain value for each time frame and each AHA segment based on tracking of the initial population of points inside the ED myocardium mask.

INPUTS

- **Pixel size**

$$Pixdim = \begin{bmatrix} S_x & S_y & S_z \end{bmatrix}$$

Code:
```
Pixdim = [x_scale, y_scale, z_scale]
```

- **Coordinates of base, apex, mid-septal points**
  Get rotation matrix & angles, to align long axis of LV with vertical z axis

$$\left(P_{apex}, P_{base} \right) \Rightarrow \Re$$

Code:
```
[xs,ys,zs,R]  =  pixelindex2cart(mid_septal(1),  mid_septal(2),  mid_septal(3),  apex,
                         base, scales);
```

- **ED mask**
  Define: (1) list of points in ED mask to track in image coordinates, Cartesian coordinates aligned with long axis, cylindrical coordinates, (2) cylindrical transform with local angles of points inside ED mask:

$$\left(x, y, z \right) \in \Omega_{ED}$$
$$\left(x, y, z \right)_{\Omega_{ED}} \rightleftharpoons \left(x^r, y^r, z^r \right)_{\Omega_{ED}} \rightleftharpoons \left(r, \theta, z^c \right)_{\Omega_{ED}}$$

$$\left\{ \left(r, \theta, z^c \right)_{\Omega_{ED}}, \Re \right\} \Rightarrow \mathbf{T}_{cyl}$$

197

```
Code:
[x1,y1,z1,R] = pixelindex2cart(x,y,z, apex, base, scales);
   [th,r]    = cart2pol(x1,y1);
```

- **AHA partition on ED Mask**

```
Seg_label
```

FOR EACH TIME FRAME *timeframe*:

Inputs are <u>ED to *timeframe*</u> displacement vectors at each point inside ED mask

$$F_{pix}\left(x,y,z\right)=\left[f_x^{pix},f_y^{pix},f_y^{pix}\right]$$

Code:
```
Fpix(x, y, z) = [fx, fy, fz];
```

Compute positions of initial ED mask at current time frame *timeframe* in rotated Cartesian coordinates and in cylindrical coordinates

$$\left[x_2,y_2,z_2\right]=\left[x+f_x^{pix},y+f_y^{pix},z+f_z^{pix}\right]$$
$$\left[x_2,y_2,z_2\right]\rightleftharpoons\left[x_2^r,y_2^r,z_2^r\right]\rightleftharpoons\left[r_2,\theta_2,z_2^c\right]$$

Code:
```
x2           = x + (fx_pix(ind));
y2           = y + (fy_pix(ind));
z2           = z + (fz_pix(ind));
[x3,y3,z3,R] = pixelindex2cart(x2, y2, z2, apex, base, scales);
```

Displacements in rotated Cartesian coordinates in pixels, then converted to mm

$$\left[f_x^{r,pix},f_y^{r,pix},f_z^{r,pix}\right]=\left[x_2^r-x^r,y_2^r-y^r,z_2^r-z^r\right]$$
$$\left[f_x^{r,pix},f_y^{r,pix},f_z^{r,pix}\right]\Rightarrow\left[f_x^{r,mm},f_y^{r,mm},f_z^{r,mm}\right]$$

Code:
```
fx_pix(ind)    = x3-x1;
fy_pix(ind)    = y3-y1;
fz_pix(ind)    = z3-z1;

fx_mm          = fx_pix * x_scale;
fy_mm          = fy_pix * y_scale;
fz_mm          = fz_pix * z_scale;
fx             = fx_mm;
fy             = fy_mm;
fz             = fz_mm;
```

Displacements in cylindrical coordinates

$$\left[f_x^{r,mm}, f_y^{r,mm}, f_z^{r,mm} \right] \xrightarrow{\ \mathbf{T}_{cyl}\ } \left[f_r^{mm}, f_\theta^{mm}, f_{z^c}^{mm} \right]$$

```
Code:
f_r(ind(:))    = (cos(th(:)) .* fx(ind(:))) + (sin(th(:)) .* fy(ind(:)));
f_th(ind(:))   = (cos(th(:)) .* fy(ind(:))) - (sin(th(:)) .* fx(ind(:)));
```

Compute gradient on <u>radial</u> displacements & Transform to cylindrical coordinates

$$\nabla f_r^{pix} = \left[\frac{\partial f_r^{mm}}{\partial x}, \frac{\partial f_r^{mm}}{\partial y}, \frac{\partial f_r^{mm}}{\partial z} \right] ./ \left[S_x, S_y, S_z \right]$$

$$\left[\frac{\partial f_r^{pix}}{\partial x}, \frac{\partial f_r^{pix}}{\partial y}, \frac{\partial f_r^{pix}}{\partial z} \right] \xrightarrow{\ \mathbf{T}_{cyl}\ } \left[\frac{\partial f_r^{pix}}{\partial r}, \frac{\partial f_r^{pix}}{\partial \theta}, \frac{\partial f_r^{pix}}{\partial z^c} \right]$$

```
Code:
[f_rx, f_ry, f_rz, Sign_strain] = gradient_with_mask(f_r, bw_myo,[1 1 1]);
f_rx = f_rx / x_scale;
f_ry = f_ry / y_scale;
f_rz = f_rz / z_scale;
[f_rr,  f_rth_r,  f_rz]  =  rotate_vect_coordinates(f_rx,  f_ry,  f_rz,  R,
                                                    theta, radius);
```

Compute gradient on <u>circumferential</u> displacements & Transform to cylindrical coordinates

$$\nabla f_\theta^{pix} = \left[\frac{\partial f_\theta^{mm}}{\partial x}, \frac{\partial f_\theta^{mm}}{\partial y}, \frac{\partial f_\theta^{mm}}{\partial z} \right] ./ \left[S_x, S_y, S_z \right]$$

$$\left[\frac{\partial f_\theta^{pix}}{\partial x}, \frac{\partial f_\theta^{pix}}{\partial y}, \frac{\partial f_\theta^{pix}}{\partial z} \right] \xrightarrow{\ \mathbf{T}_{cyl}\ } \left[\frac{\partial f_\theta^{pix}}{\partial r}, \frac{\partial f_\theta^{pix}}{\partial \theta}, \frac{\partial f_\theta^{pix}}{\partial z^c} \right]$$

```
Code:
[f_thx, f_thy, f_thz, Sign_strain] = gradient_with_mask(f_th, bw_myo, [1 1
                                                        1]);
f_thx = f_thx / x_scale;
f_thy = f_thy / y_scale;
f_thz = f_thz / z_scale;
[f_thr, f_thth_r, f_thz] = rotate_vect_coordinates(f_thx, f_thy, f_thz, R,
                                                   theta, radius);
```

Compute gradient on <u>longitudinal</u> displacements & Transform to cylindrical coordinates

$$\nabla f_{z^c}^{pix} = \left[\frac{\partial f_{z^c}^{mm}}{\partial x}, \frac{\partial f_{z^c}^{mm}}{\partial y}, \frac{\partial f_{z^c}^{mm}}{\partial z} \right] ./ \left[S_x, S_y, S_z \right]$$

$$\left[\frac{\partial f_{z^c}^{pix}}{\partial x}, \frac{\partial f_{z^c}^{pix}}{\partial y}, \frac{\partial f_{z^c}^{pix}}{\partial z} \right] \xrightarrow{\mathbf{T}_{cyl}} \left[\frac{\partial f_{z^c}^{pix}}{\partial r}, \frac{\partial f_{z^c}^{pix}}{\partial \theta}, \frac{\partial f_{z^c}^{pix}}{\partial z^c} \right]$$

```
Code:
[f_zx, f_zy, f_zzz, Sign_strain] = gradient_with_mask(fz, bw_myo,[1 1 1]);
f_zx  = f_zx / x_scale ;
f_zy  = f_zy / y_scale;
f_zzz = f_zzz/ z_scale;
[f_zr,  f_zth_r,  f_zz]  = rotate_vect_coordinates(f_zx,  f_zy,  f_zzz,  R,
                                                   theta, radius);
```

Compute average strain values within each AHA segment

```
Code:
[f_rs(frame,:),      f_r_rs(frame,:),   f_ths(frame,:),
 f_th_rs(frame,:),   f_zs(frame,:),     f_rrs(frame,:),
 f_rth_rs(frame,:),  f_rzs(frame,:),    f_thrs(frame,:),
 f_thth_rs(frame,:), f_thzs(frame,:),   f_zrs(frame,:),
 f_zth_rs(frame,:),  f_zzs(frame,:),    f_thetazs(frame,:)]
   =      create_segmental_maps(f_r,f_r_r,f_th,f_th_r,f_z,
```

201

```
                         f_rr,f_rth_r,f_rz,f_thr,f_thth_r
                         f_thz,f_zr,f_zth_r,f_zz,Seg_label);
```

END FOR EACH TIME FRAME

Compute the gradient tensor in <u>cylindrical coordinates</u> at each time frame *timeframe* and within each segment *segment:*

$$U\left(timeframe, segment\right) = \begin{bmatrix} \dfrac{\partial f_r^{pix}}{\partial r} & \dfrac{1}{r}\dfrac{\partial f_r^{pix}}{\partial \theta} - \dfrac{f_\theta}{r} & \dfrac{\partial f_r^{pix}}{\partial z^c} \\[3mm] \dfrac{\partial f_\theta^{pix}}{\partial r} & \dfrac{1}{r}\dfrac{\partial f_\theta^{pix}}{\partial \theta} + \dfrac{f_r}{r} & \dfrac{\partial f_\theta^{pix}}{\partial z^c} \\[3mm] \dfrac{\partial f_{z^c}^{pix}}{\partial r} & \dfrac{1}{r}\dfrac{\partial f_{z^c}^{pix}}{\partial \theta} & \dfrac{\partial f_{z^c}^{pix}}{\partial z^c} \end{bmatrix}$$

Code:
```
U = [   f_rrs(frame,k),    f_rth_rs(frame,k) - f_th_rs(frame,k),      f_rzs(frame,k);
        f_thrs(frame,k),   f_thth_rs(frame,k) + f_r_rs(frame,k),      f_thzs(frame,k);
        f_zrs(frame,k),    f_zth_rs(frame,k),                         f_zzs(frame,k)];
```

Computation of the Green symmetric strain tensor

$$E = \frac{U + U^T + U^T U}{2}$$

Code:
```
E = (U+U'+U'*U)/2;
```

B.3 Radial Strain Measurement in Previous Literature

Since no ground-truth measurements of radial strain in the human LV exists, we reviewed literature on LV strain from 2000 to 2014 published in reputable journals to determine what range of E_{rr} values is considered realistic in healthy human subjects.

First, according to [171] in *Biomechanics: Principles and Applications*, "intact cardiac muscle experiences finite deformations during the normal cardiac cycle, with maximum Lagrangian strains (which are generally radial and endocardial) that may easily exceed 0.5 in magnitude". Furthermore, in his 2006 *JACC* review of strain measurement by echocardiographic techniques, Marwick cites the work of Kowalski et al. [172] in stating that "the complexities of fiber direction [in the LV] cause a longitudinal shortening of 20% to 30% to generate a radial thickening of 50% to 70%" [173].

In 2003, Kukulski et al. used a GE Vingmed System 5 and accompanying TDI software to measure 2D radial segmental deformation in 90 patients with stable angina undergoing angioplasty, and 20 controls [174]. Their results are reproduced below in Figure B-2. Note that in the healthy control population, TDI produced peak strain estimates of 59.9 ± 12.1%. Upon reperfusion, segments that were found to be "visually normal," were found to reach peak radial deformation of 60.4 ± 10.8%. In parallel, the control population demonstrated longitudinal strains of -20.6 ± 4.4%.

Table 1. Parameters of Radial Segmental Deformation During Circumflex/Right Coronary Artery Coronary Angioplasty in Visually Normal (Group I) and Abnormal Segments (Group II)—Long-Axis Parasternal View

	Control (n = 20)	Group I (n = 26)			Group II (n = 19)		
		Baseline	Occlusion	Reperfusion	Baseline	Occlusion	Reperfusion
ϵ_{SYS} (%)	56.3 ± 11.7	49.0 ± 6.9*	23.0 ± 14.6†	56.0 ± 11.9	21.9 ± 11.0*	11.3 ± 8.4†	30.0 ± 13.4
ϵ_{PEAK} (%)	59.9 ± 12.1	52.9 ± 8.5*	37.6 ± 16.1†	60.4 ± 10.8	26.6 ± 12.1*	23.5 ± 10.6	33.2 ± 13.8
ϵ_{PS} (%)	4.1 ± 4.0	3.8 ± 3.1	14.6 ± 9.5†	4.4 ± 4.0	4.4 ± 3.7	11.3 ± 7.8†	3.2 ± 3.1
PSI	0.06 ± 0.05	0.06 ± 0.04	0.41 ± 0.23†	0.07 ± 0.07	0.18 ± 0.14*	0.48 ± 0.26†	0.13 ± 0.18
Tϵ (ms)	54 ± 33	67 ± 31	107 ± 24†	61 ± 45	65 ± 40	104 ± 24†	68 ± 39

*p < 0.05 vs. control; †p < 0.001 vs. baseline.

ϵ_{SYS}, ϵ_{PEAK}, and ϵ_{PS} = systolic, peak, and postsystolic strains, respectively; PSI = postsystolic strain index; Tϵ = time from end-systole to peak strain.

Figure B-2. Results on radial strain reported by Kukulski et al. in [174].

Although TDI is a significantly different method of strain estimation as compared to OF, we note that the values observed in the control population are quite close to our findings.

In 2007, Hurlburt et al. measured 2D radial strain in SAX views on 60 healthy adults, using a GE Vivid 7 machine and Echopac software [175]. Their key findings with respect to peak strain values averaged over the population on a segment basis, are summarized Figure B-3, below.

TABLE III

Mean Strain (ε) Values by Region in the Study Population

Longitudinal (ϵ_l)						
Basal septal	Mid septal	Apical septal	Apical lateral	Mid lateral	Basal lateral	ANOVA
17 ± 4	19 ± 4	23 ± 6	21 ± 7	19 ± 6	19 ± 6	0.78
Circumferential (ϵc)						
Anterior	Lateral	Posterior	Inferior	Septal	Antero septal	ANOVA
24 ± 6	22 ± 7	21 ± 7	22 ± 6	24 ± 6	26 ± 11	0.001
Radial (ϵ_r)						
Anterior	Lateral	Posterior	Inferior	Septal	Antero septal	ANOVA
39 ± 16	37 ± 18	37 ±17	37 ± 17	37 ± 19	39 ± 15	0.98

Figure B-3. Results on mean radial strain reported by Hurlburt et al. in [175].

Additionally, they compared peak strains between men and women, with the following results:

Strain	Males	Females
E_{cc}	20.9 ± 4.3	25.4 ± 6.3
E_{zz}	18.4 ± 4.0	20.8 ± 4.3
E_{rr}	35.0 ± 10.2	40.0 ± 15.6

Examining these values in the context of previous findings, Hurlburt stated: "our values for radial strain are consistent with average thickening values of 35-42% observed by Bogaert and Rademakers using magnetic resonance tagging, Hugenholtz et al. using angiography, and 31-50% by M-mode and 2D echocardiography."

We note that while the peak longitudinal and circumferential values were close to our observations, the peak radial deformation observed in this study was lower than what we measured, but still above 35%.

Also in 2007, Zervantonakis et al. described a novel method for eliminating dependence of 2D echocardiographic Lagrangian strain computation on the view and centroid [176]. They evaluated a dedicated myocardial elastography (ME) algorithm (using normalized cross-correlation on RF data), on a 3D finite-element (FE) model of baseline and ischemic canine tissue. In Figures 3 and 4 of this article, the authors reported peak radial strains of up to 30% in both normal and ischemic cases. Meanwhile, the circumferential strains exhibited peaks of -20%. For both components, the endocardial strains were consistently greater than the epicardial values. These values may not be directly comparable to our study because they were derived from a computational model of canine tissue.

As part of an *in-vivo* validation study in the same year, Lee et al. compared 2D ME-based strains to those derived from tagged MRI (tMRI) in a healthy human volunteer [177]. Although average and peak values were not reported explicitly, Figure 10 of the article demonstrated that peak cumulative radial strains by 2D ME reach 50% at ES (particularly in the mid-inferior segments), while cumulative circumferential strains tend to be in the 25-40% range. While the strain distributions measured by tMRI were similar, the values were generally lower.

In a follow-up study in 2009, Luo et al. evaluated the performance of 2D ME in a phase-array configuration, using the same canine LV model and ultrasonic images simulated with Field II [178]. As reported in Figure 5 of this article, the peak cumulative strains in the healthy canine LV from ED to ES were approximately 25% for E_{rr} and -25% for E_{cc}. These ME-derived values were found to be in close agreement with the FE model, as corroborated by low mean absolute errors (around 3%). Peak cumulative strains in the ischemic case tended to be lower, and were also in agreement with the FE model.

In 2008, Nottin et al. reported the results of their efforts to measure 2D strain in a cohort of 16 athletes and 23 controls using a GE Vivid I machine and EchoPac STE software [179]. In addition to observing significant differences between athletes and healthy but sedentary individuals, their analysis revealed that peak radial strain varies along the longitudinal axis of the LV, with values typically larger at the apex compared to the base. Specifically, the peak radial strains at the apex were: 42.7 ± 10.5% (controls) vs. 52.2 ± 14.3% (athletes); the peak radial strains at the base were 41.7 ± 11.9% (controls) vs. 41.5 ± 14.4% (athletes).

In 2009, Saito et al. applied a 2D and 3D imaging protocol similar to the one in our study to

206

46 healthy volunteers, using a Toshiba Artida machine and accompanying software [100]. In their study they achieved frame rates similar to ours (50-70Hz for 2D and 20-30Hz for 3D). The global mean strain values are summarized below in Figure B-4.
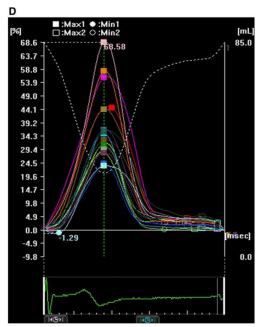
Table 3 Mean strain values of 16 segments for longitudinal, circumferential, and radial strains

	3DT	2DT	P
Longitudinal, %	−17.0 ± 5.5	− 19.9 ± 5.3	<.0001
Circumferential, %	−31.6 ± 8.0	− 27.8 ± 6.9	<.0001
Radial, %	34.4 ± 11.4	35.1 ± 11.8	.20

3DT, 3D speckle tracking; 2DT, 2D speckle tracking.

Figure B-4. Mean strain measures reported by Saito et al. in [100].

While the mean radial strain is below what we have observed, in Figure 1D (replicated in Figure B-5 below) they demonstrate an example of radial strains for which peak values exceed 50% (up to 69%) in 3 segments.

3D strain analysis. **A,** The LV was divided into 16 segments (6 basal,
I radial **(D)** strain.

Figure B-5. Radial strain profiles from Saito et al. in [100] showing peak values above 50%.

In 2014, Kaku et al. sought to establish the range of normal LV strain in different age groups [93]. In the first protocol, 19 patients (mean LVEF: 48 ± 15%) who were referred for CMR were also scanned using RT3DE, with a Philips Sonos 7500 or iE-33 machine. In the second protocol, 335 normal subjects underwent RT3DE imaging. A single apical view and 1-heartbeat acquisition were used, resulting in a mean frame rate of 21 Hz. All strain analysis was performed using the TomTec 4D LV Analysis software.

The results of the first protocol, with respect to mean strain values, are summarized below:

Strain	RT3DE	CMR
E_{cc}	-19.2 ± 6.7%	19.1 ± 6.8%
E_{zz}	-11.3 ± 4.4%	-16.8 ± 6.0%
E_{rr}	47.1 ± 20.3%	36.1 ± 14.2%

The results of the second protocol, with respect to mean strain values, separated by age group, are summarized in Figure B-6 below.

Table 3 Global and level 3D strains according to the age group

	Age group (y)								P
	1–3	4–9	10–19	20–29	30–39	40–49	50–59	>60	
Longitudinal strain									
Basal	−28.3 ± 4.4	−26.1 ± 3.2	−22.9 ± 4.9*†	−18.6 ± 3.5*†‡	−18.3 ± 3.8*†‡	−18.9 ± 3.5*†‡	−18.8 ± 3.0*†‡	−18.3 ± 4.1*†‡	<.0001
Middle	−21.2 ± 2.7	−21.0 ± 2.5	−20.9 ± 3.4	−19.6 ± 3.5	−19.2 ± 3.3	−19.5 ± 2.9	−19.8 ± 3.3	−19.6 ± 3.4	.0371
Apical	−18.3 ± 3.8	−17.8 ± 4.7	−20.3 ± 4.7	−21.5 ± 4.1†	−19.6 ± 3.9	−20.6 ± 3.8	−21.0 ± 5.3†	−22.1 ± 4.5†	<.0001
P	<.0001	<.0001	.0638	.0017	.2366	.1056	.0960	<.0001	
Global	−22.7 ± 2.6	−21.9 ± 2.1	−21.4 ± 3.4	−19.8 ± 3.2*†	−19.1 ± 2.9*†‡	−19.6 ± 2.8*†	−19.9 ± 3.1	−19.9 ± 3.3*†	<.0001
Circumferential strain									
Basal	−30.8 ± 5.7	−29.3 ± 5.9	−25.6 ± 3.9*†	−23.6 ± 4.5*†	−23.3 ± 5.5*†	−22.4 ± 5.0*†	−23.1 ± 3.7*†	−23.0 ± 4.0*†	<.0001
Middle	−29.6 ± 4.5	−31.6 ± 5.4	−30.5 ± 5.4	−30.7 ± 4.7	−31.1 ± 5.7	−30.6 ± 6.1	−30.7 ± 4.3	−33.2 ± 5.0	.0922
Apical	−28.2 ± 7.1	−27.5 ± 5.9	−29.3 ± 7.1	−31.6 ± 5.3	−31.2 ± 6.4	−30.8 ± 7.0	−31.5 ± 6.4	−34.0 ± 6.9†‡	<.0001
P	.4795	.0041	.0021	<.0001	<.0001	<.0001	<.0001	<.0001	
Global	−29.3 ± 4.0	−29.4 ± 4.3	−28.4 ± 4.5	−28.4 ± 4.0	−28.5 ± 5.2	−27.8 ± 5.2	−28.6 ± 4.1	−29.9 ± 4.5	.3542
Radial strain									
Basal	97.3 ± 22.6	97.6 ± 20.9	79.1 ± 17.9†	65.5 ± 18.7*†	66.7 ± 25.4*†	63.8 ± 20.3*†‡	61.5 ± 14.5*†‡	63.6 ± 17.4†‡*	<.0001
Middle	87.8 ± 17.7	97.5 ± 25.5	95.7 ± 21.7	93.6 ± 24.1	91.4 ± 24.4	90.9 ± 23.7	94.3 ± 25.4	105.1 ± 26.4	.0438
Apical	77.9 ± 23.4	78.3 ± 26.4	99.9 ± 40.9	105.5 ± 34.4†	96.9 ± 31.8	99.8 ± 31.8	103.7 ± 36.1†	119.8 ± 36.6*†§	<.0001
P	.0575	.0002	.0134	<.0001	<.0001	<.0001	<.0001	<.0001	
Global	88.6 ± 16.1	92.7 ± 20.8	90.4 ± 20.8	86.3 ± 22.7	83.4 ± 23.2	82.9 ± 21.8	84.5 ± 20.1	92.5 ± 22.4	.1599
3D strain									
Basal	−42.4 ± 4.3	−40.4 ± 4.1	−36.1 ± 4.0*†	−32.3 ± 4.3*†‡	−32.7 ± 6.4*†	−32.5 ± 5.0*†‡	−31.7 ± 4.1*†‡	−32.5 ± 4.2*†‡	<.0001
Middle	−38.4 ± 5.2	−39.3 ± 4.8	−39.1 ± 4.3	−38.1 ± 4.9	−37.9 ± 5.9	−37.8 ± 5.6	−38.2 ± 4.9	−40.9 ± 5.0	.0317
Apical	−37.1 ± 7.3	−36.0 ± 6.5	−39.4 ± 7.0	−40.6 ± 6.8	−38.3 ± 6.6	−39.8 ± 7.2	−40.5 ± 7.3	−44.2 ± 7.2*†‡§	<.0001
P	.0434	.0003	.0314	<.0001	<.0001	<.0001	<.0001	<.0001	
Global	−38.5 ± 4.7	−38.8 ± 4.0	−37.9 ± 4.1	−36.3 ± 4.7	−36.3 ± 5.5	−36.2 ± 5.2	−37.1 ± 5.1	−39.0 ± 4.6	.0118

Data are expressed as mean ± SD (range).
*P < .001 versus 1 to 3 years.
†P < .001 versus 4 to 9 years.
‡P < .001 versus 10 to 19 years.
§P < .001 versus 30 to 39 or 40 to 49 years.

Figure B-6. Mean strain measures reported by Kaku et al. in [93].

We note that while E_{cc} and E_{zz} show mean values similar to what is routinely measured in other studies, here mean E_{rr} values are sometimes over 100%, with averages well above the 60% we measured. The authors remarked, "radial strain values seemed to be very high.

Although the exact strain algorithms and formulas are proprietary and hidden from end users, we think the value could be based on calculations from the endocardium. This will lead to different values of strain than if the calculations were based on the midwall position." This statement is indeed corroborated by our investigation of TomTec's strain calculation approach, which does consider only the endocardium, and by the study from Zervantonakis et al. which noted that strains tend to be larger at the endocardium compared to the epicardial wall. Consequently, it is feasible that if the entire myocardium were considered, the observed peak radial strains could be reduced into the 40-60% range, as we have seen.

In a similar study in 2014, Muraru et al. sought to establish 3D strain reference values using vendor-specific STE software [97]. They recruited 338 healthy volunteers and scanned them using a GE Vivid 9 machine. Strain analysis was performed using GE Echopac (4D AutoLVQ) and also using TomTec 4D LV Analysis. Strains were measured in 2D and 3D using both software packages. Global peak strain parameters (Table 2 in the paper) measured by Echopac (4D AutoLVQ) were as follows: E_{rr}: 49 to 53% across all age groups, up to 57% in women; E_{cc}: -18 to -20%; E_{zz}: -17 to -20%. Per Table 3, there was also significant regional variation in the three strain components, with peak E_{rr} varying from 45% at the base to 55% at the apex (similarly to what had been previously reported by Nottin et al. [179]). In Figure 5, box and whisker plots depicting segmental strain by 3D STE show that E_{rr} routinely exceeds 50% and even 60%. The comparison between GE Echopac and TomTec (Table 5) revealed that the GE-based peak radial strain of 52% [47, 59] corresponded to 41% [36, 44] by TomTec's algorithm (values in [ ] denote 1st and 3rd quartiles). Lastly, they also found that peak 3D E_{rr} was generally higher than 2D E_{rr} (52% vs 46%).

The authors remarked: "our reference values are similar to those obtained in a very recent study (Kaku et al. [93]), except for 3DRε [3D Radial Strain] and principal tangential strain. The difference in 3DRε values is explained by the use of an earlier version of this prototype software, in which 3DRε was calculated from 3D (tangential) strain at the endocardium, assuming preservation of regional myocardial volumes. This assumption can be erroneous in the presence of a highly trabecular endocardium, and consequently the 3DRε values were not physiologically sound for normal hearts, as acknowledged by the authors." This statement is not totally supported by Kaku's paper (see above); Kaku et al. only state that the values taken from mid-wall measurements might be different.

Lastly, in their 2014 article, Yuda et al. quantified the inter-vendor variability of LV strains determined by STE [105]. They acquired data from 41 healthy subjects using GE Vivid E9 ("V1") and Toshiba Artida ("V2") machines. Acquisition was performed via a 3D apical view, in 4-beats, resulting in a frame rate > 25Hz in all studies. Strain analysis was performed using vendor-specific software, GE Echopac and Toshiba 3D WMT, respectively. Global peak 3D strains by both vendors are summarized in Figure B-7 below:

	VI (n = 26)	V2 (n = 26)	P-Value
3D-LS	-20.5 ± 4.8	-17.0 ± 1.7	<0.01
3D-CS	-20.9 ± 3.1	-39.5 ± 3.8	<0.01
3D-RS	56.2 ± 8.0	39.6 ± 12.7	<0.01

Figure B-7. Peak radial strain values reported by Yuda et al. in [105].

Additionally, Figure B-8 shows peak strains for each component at the 3 LV levels.
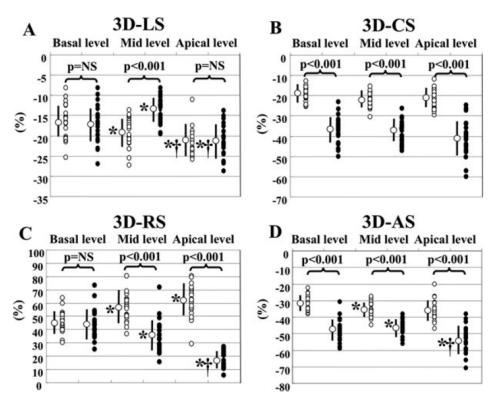

Figure 3. Comparison of three-dimensional longitudinal (3D-LS) **A.** circumferential (3D-CS) **B.** radial (3D-RS) **C.** and area strains (3D-AS) **D.** at three left ventricular levels between V1 (white dots) and V2 (black dots). *P < 0.05 versus basal level, †P < 0.05 versus mid level.

Figure B-8. Replication of Figure 3 from Yuda, et al. in [105].

We note that overall, the peak values measured by OF are well within the range of deformation measured by GE software, which itself is in agreement with most of the preceding studies.

With respect to strain measurement by MRI, one of the most highly cited papers was published by Moore et al. in 2000 [79]. In this study, 3D strain was measured in 31 healthy adults using tagged MRI. All strain components were measured in each of the four LV walls.

Although the imaging modality and tissue tracking approach is quite distinct from STE, the final strain calculation was performed using the same general formula (e.g. $E = \frac{1}{2}F^T F\text{-}I$). In the table replicated in Figure B-9, the authors summarized the average peak strains across the subject population and in each of the four walls.

TABLE 2
Average Peak Strain Components and Indexes

Strain	Septal	Anterior	Lateral	Inferior
SI				
Basal	−0.17 ± 0.03	−0.20 ± 0.03	−0.20 ± 0.03	−0.18 ± 0.03
Equatorial	−0.17 ± 0.03	−0.22 ± 0.04	−0.21 ± 0.03	−0.18 ± 0.04
Apical	−0.20 ± 0.03	−0.25 ± 0.05	−0.25 ± 0.04	−0.24 ± 0.05
T				
Basal	0.46 ± 0.10	0.58 ± 0.12	0.60 ± 0.12	0.50 ± 0.11
Equatorial	0.49 ± 0.10	0.68 ± 0.17	0.61 ± 0.12	0.51 ± 0.14
Apical	0.63 ± 0.14	0.82 ± 0.21	0.80 ± 0.17	0.77 ± 0.20
E_{RR}				
Basal	0.45 ± 0.12	0.42 ± 0.21	0.52 ± 0.19	0.41 ± 0.17
Equatorial	0.42 ± 0.19	0.52 ± 0.25	0.38 ± 0.18	0.35 ± 0.22
Apical	0.36 ± 0.22	0.67 ± 0.31	0.49 ± 0.29	0.39 ± 0.38
E_{CC}				
Basal	−0.17 ± 0.03	−0.20 ± 0.03	−0.21 ± 0.03	−0.16 ± 0.03
Equatorial	−0.16 ± 0.03	−0.23 ± 0.04	−0.22 ± 0.03	−0.16 ± 0.05
Apical	−0.18 ± 0.03	−0.24 ± 0.06	−0.24 ± 0.04	−0.23 ± 0.04
E_{LL}				
Basal	−0.14 ± 0.03	−0.15 ± 0.03	−0.15 ± 0.03	−0.15 ± 0.03
Equatorial	−0.15 ± 0.03	−0.15 ± 0.03	−0.14 ± 0.04	−0.15 ± 0.03
Apical	−0.18 ± 0.04	−0.19 ± 0.03	−0.19 ± 0.03	−0.18 ± 0.04

Figure B-9. Average peak strain measures on MRI, reported by Moore et al. in [79].

The authors state: "our midwall E_{rr} values were greater (0.36–0.67 vs 0.02–0.25). These differences may be partially explained by the difficulty of the two MR tagging–based methods to generate more than two lines across the heart wall, the relatively small amount of data in this direction, and the differences in 3D reconstruction technique. Our E_{RR} values corresponded approximately to midwall thickening of 46%–80%. These data are in closer agreement with the

other wall thickening estimates based on cine computed tomography (average, 66% ± 12 [40]; approximately 125% at the middle level [41]), short-axis cine MR imaging (56% ± 24 basally to 91% ± 29 apically [36]), and radially tagged MR imaging (55% ± 4 [39]). Lessick, et al. (40) observed increasing base-to-apex gradients of thickening of approximately 50% ± 15 basally to 72% ± 18 apically; these values are in good agreement with those in our study."

However, they also mention that the sparsity of tags in their images means that the E_{rr} estimates they compute are not necessarily representative of the true strain.

B.4 Radial Strains Reported by Our Group

Aside from the results described in Chapter 3, our group reported radial strain values in the human LV in one earlier article [81]. In this study, Lorsakul et al. scanned 5 volunteers using a Philips iE-33, with frame rates ranging from 15 to 35Hz. At 35Hz, the peak E_{rr} averaged across all 5 subjects was 51%. At 25Hz, the peak E_{rr} was 37.7%.

B.5 Summary

Our review of previous literature on radial strain in the human LV, using both B-mode echocardiography and MRI-based methods suggests that the peak E_{rr} values observed in our study are within the range of deformation seen by other investigators. Although we could not locate any experimental evidence of ground-truth strain measurements in the human LV, it was notable that at least two independent sources described the physiological basis for peak radial values to be within the range 50-70% combined with longitudinal/circumferential shortening peak values within the range 20-30%. These values closely match our observations.

214

Additionally, a close examination of the tracking and strain computation algorithms suggested that our method of tracking, which computes displacement gradients between points which are neighbors at ED, may contribute to larger deformation estimates when compared to techniques which update direct neighborhood points at each time point.